Investigation of Precise Relative Positioning through Varying Equipment Grades

by

Christian J. Campos-Vega

A thesis submitted to the Graduate Faculty of
Auburn University
in partial fulfillment of the
requirements for the Degree of
Master of Science

Auburn, Alabama
May 07, 2022

Keywords: Ambiguity Resolution, Relative Navigation, RTK, DRTK

Approved by

Scott M. Martin, Chair, Assistant Professor of Mechanical Engineering
David M. Bevly, Bill and Lana McNair Distinguished Professor
Mark A. Hoffman, Assistant Professor of Mechanical Engineering

Abstract

In this thesis, three methodologies are investigated in order to provide precise relative positioning knowledge between two dynamic platforms as equipment grade is varied. Two methods are integrated into the real-time kinematic (RTK) algorithm using differential GPS techniques to aid the ambiguity resolution of static and dynamic baselines. Lastly, with the introduction of modern GNSS signals, the benefits of integrating single-frequency (SF) observables from GPS, Galileo (GAL), and the BeiDou (BDS) constellations into a single RTK algorithm is explored. The first method uses an adaptive extended Kalman Filter (EKF) to estimate stochastic properties of single-differenced (SD) GPS combinations. This technique improves the resolution of the carrier-phase ambiguities allowing for precise relative navigation and improved time-to-first fix (TTFF). Secondly, a tightly-coupled RTK algorithm is demonstrated which combines ultra-wideband radio (UWB) observables with SD GPS combinations. This is shown to improve TTFF and increase the robustness of the fixed integer solution. An overview of the estimation techniques is provided, and errors observed in diagnostic assessment tools are explained.

To better evaluate the robustness of the presented algorithms, they are applied to experimental data collected with equipment of varying grade. Survey-grade equipment is heavily used in RTK research or in applications with a need for precise relative positioning between a base and rover platform. This equipment can be costly and not applicable to many emerging modular technologies. Low-cost sensor suites have been shown to create noisier observables due to the instabilities of their internal oscillators. In addition, low-cost antennas exhibit irregular gain patterns and poor multi-path suppression which obscure the ambiguity search space leading to longer TTFF and higher chances of incorrectly fixing integers. Thus, it is of interest to evaluate the effects of equipment grade on the ambiguity search space for on-the-fly ambiguity estimation.

The investigation of the search space is first assessed using a zero-baseline test. This test provides insight into the observability of the carrier phase ambiguity since no geometric

range is embedded in the observables. The study then continues by evaluating the search space during a static baseline test. Measurement innovations are monitored and a unique integer validation scheme is shown to improve the percentage of correct integer fixes for all utilized equipment. Lastly, the RTK algorithm is extended to consider dynamic baselines under the pretense that both the base and rover platforms are mobile. This breaks several assumptions of the nominal RTK algorithm and allows it to be considered a Dynamic-Real Time Kinematic (DRTK) algorithm.

Acknowledgments

I am thankful for my family who gave me reprieve from GRA stress with food, World of Warcraft, League of Legends, Smash, Mario Kart and laughter. I am thankful for the first floor office and the daily shenanigans we had, downtown nights, pizza at Shittly's, arguments/conversations and communal stress relieve sessions. Shout out to everyone else in the GAVlab who had an impact on me. I won't list names (because I will forget some) but for late nights testing, working, stressing, studying or whatever we were doing... you made it easier and a more enjoyable experience. Big thanks to Eminem, Tech N9ne and anime for being amazing! I could not have done without those three :). And lastly, I am thankful for Dr. Bevly and Dr. Martin for allowing me to grow as an individual, engineer, and academic and for providing me with work on work.... which paid for my Master's education so I have to respect it :).

P.S. War Eagle

P.S.^{2} ”I believe that this is a practical world and that I can count only on what I earn. Therefore, I believe in work, hard work” - George Petrie

Table of Contents

List of Figures

List of Tables

Chapter 1

Introduction

The demand for precise relative positioning has increased as vehicle-to-vehicle (V2V) and vehicle-to-infrastructure (V2I) autonomous technologies become integrated into the commercial, industrial, and military sectors. This transition to cooperative or complete autonomous task completion has led researchers and engineers to explore system configurations with varying sensor suites and equipment grades. With this considered, mission parameters such as power consumption, weight, cost, mission objectives and operational limits can influence the selection of sensors.

When relative position information between platforms or between a platform and an environment of interest is desired, a few sensors exist capable of providing this information. Cameras and laser sensors are capable of providing the needed accuracy, but can increase the cost, computing cost and complexity of the holistic system. Furthermore, they are operationally limited to perform only when needed information can be extracted from the perceived environment. Ultra Wide-Band (UWB) radios have been proven to be cheap yet robust sensors through many environments. Their ability to provide ranging measurements within line-of-sight (LoS) at varying baselines has been acknowledged and can be furthered observed in [12][15]. In [7][9][15], their incorporation into V2V and V2I relative positioning has been shown to provide robust localization in indoor and outdoor environments. However, these localization schemes are susceptible to radio dropouts and are limited to the perceptional range of the utilized radios.

Global Navigation Satellite Systems (GNSS) utilizing differential techniques or DGPS techniques are also capable of providing the desired relative sensing information. This mature technology is attractive due to the availability of the solution and the precision of carrier phase-based approaches [We need a reference!]. In addition, GNSS equipment can vary in size

and cost making it adaptable to variety of applications. This makes GNSS-based positioning methods ideal in many scenarios.

1.1 Prior Art

GPS-based relative positioning has been studied for many years. Researchers and engineers have developed many methodologies for maintaining an accurate solution through a variety of environments and scenarios. Sensor fusion approaches couple information from different sensors to improve the availability of the desired solution. Stochastic approaches aim at modeling uncertainties to improve the accuracy of the solution under certain conditions. Lastly, with the introduction of new constellations, GNSS based relative positioning has been the focus of recent years. Prominent results of each of these methods will be summarized in the subsequent sections.

1.1.1 Multi-GNSS

With the completion of the new BeiDou-3 era of Chinese GNSS satellites and the European Galileo constellation, precise relative navigation with low-cost equipment is not only achievable but available in many environments where GPS alone would fail. With these new capabilities, researchers have been busy integrating these new sources of information into a single navigation algorithm. The coupling of regional BDS-2 and GPS observables for a combination of low-cost receivers with high-grade antennas is explored in [2]. It demonstrated improved ambiguity resolution (AR) for not only dual frequency cases, but also when the filter is limited to single frequency observables. [3] couples BDS-3 with GPS observables, but also takes this a step further by evaluating the effects of varying equipment grade. It demonstrates an increase in measurement uncertainty corresponding to decreasing antenna grade. This is explained to be caused by the inherent gain patterns and poor multipath suppression. Through modeling sensor covariances via Least Squares variance component estimation (LC-VCE), the proposed algorithm is capable of coupling GPS-BDS observables to achieve a fixed integer precision RTK solution.

1.1.2 Adaptive Estimation

Survey grade receivers provide robust tracking algorithms giving precise observables to any user. In addition, survey grade antennas not only provide multi-frequency perception but suppress the effects of multipath on the receivers' tracking loops, further improving the quality of the provided observables. There exist scenarios and circumstances where this equipment may not be feasible or applicable to the platform(s) of interest. In these situations, the use of low-grade equipment is unavoidable. These have been shown to be less precise and more susceptible to multipath making it difficult to seamlessly place observables from these sensors into algorithms expecting survey level information. Stochastic methods for better modeling of sensor uncertainty is not a new technique. In the application of satellite relative positioning, [4] introduces an adaptive EKF formulation which allows for centimeter-level positioning accuracy. These satellites have poor LoS to GPS SVs, causing poor observability of the ambiguities. Stochastic methods are also used to improve the AR of low-grade equipment in [3].

1.1.3 Sensor Fusion

GNSS-based approaches to navigation work well in open-sky conditions, but degrade in cities due to LoS obstructions and in hostile environments where the satellite signals may become compromised. In these situations, information from additional sensors can constrain the navigation solution during GNSS outages to limit positional errors. DGPS/INS is a common technique to constrain positioning errors during GNSS outages. This has been demonstrated in a variety of architectures and further studied in [5][6]. In situations where the quality of observables is poor, however, INS can not improve the AR of problem. In these circumstances, additional observations of positional information can be beneficial. Camera and laser systems can provide this information, but as previously stated, increase the complexity and cost of the system. As alluded, combining UWB and GPS sensing information has been of much interest recently. The combination of UWB and DGPS is discussed in [4][5][6] to varying degree. [4] introduced the aid provided by UWB measurements to ambiguity fixing through the C-Lambda method. In that work, the UWB range measurement is used as an *a priori* baseline measurement during

the LAMBDA method. It demonstrated an improvement to the time-to-fix of the navigation problem when the baseline error between the distinct sensor phase centers is less than a 5 cm threshold. In [5], a tightly-coupled UWB/RTK algorithm was introduced with real data. The data was gathered in the context of an RTK surveyor who has augmented the work site with 3 other static UWB radios. UWB biases were added to the state vector and estimated while GPS was available, then relied on when the GPS solution was degraded or unavailable. [6] validated a tightly-coupled formulation between IR-UWBs and single-differenced (SD) GPS observables in simulation. The aim was to evaluate the performance of the aided navigation solution through increasing magnitudes of error sources such as multi-path, a prominent problem in aerial vehicle navigation.

1.2 Objectives and Contributions

The focus of the research presented in this thesis is the evaluation of the ambiguity resolution for platforms with varying grade equipment. In addition, we assume that both platforms are mobile, breaking a key aspect of standard RTK methods. To that end, the following contributions are made:

- A combination of three commercially available GNSS receivers and antennas are tested. They are evaluated based on their ability to achieve fixed integer precision in zero, static, and dynamic baselines.
- Two carrier-phase DGPS methods are discussed which utilize GPS L1 only; and GPS L1, Galileo E1b, and BeiDou B1. The algorithms are compared based on time-to-fix, integer validation metrics, and consistency of their computed high-precision results in various operational scenarios.
- The second method tightly-couples DGPS observables and UWB observables for precise relative navigation between UAVs and UGVs. This formulation aims to experimentally validate the tightly-couple algorithm when low-cost equipment on platforms experiencing high dynamics.

- The probability of correct integer fixing is examined by comparing the true ambiguity values to the estimate set at every epoch. The time-to-first-fix (TTFF) is calculated and the time-to-fix (TTF) is computed for the remaining data set to assess the AR for each scenario.

1.3 Thesis Outline

Chapter 2 discusses the GNSS systems under consideration while describing the unique characteristics of each. Chapter 3 introduces the differential GPS technique known as RTK and distinguishes it from its dynamic counter part DRTK. Chapter 3 also demonstrates the capabilities and weaknesses of DRTK for three cases. Chapter 4 presents the tests used to assess the performance of the equipment and presented algorithms in various operational scenarios. Finally, Chapter 5 provides conclusions from the work presented here and provides direction for future work in the field of carrier-based relative positioning.

Chapter 2

Global Navigation Satellite Systems

GNSS is the collective term for all satellite navigation systems providing position, velocity, and timing (PVT) capabilities. At this point, GPS, Glonass, Galileo and Beidou are all capable of providing this functionality to commercial, civilian, and military users. A GNSS consists three main segments: the space segment, which consists of the satellites; the control segment, which is responsible for proper operation of the system; and the user segment, which includes the GNSS receivers providing the PVT solution to users. For this work, only GPS, Galileo, and BeiDou are discussed. GLONASS is excluded due to its unique frequency division multiple access (FDMA) multiplexing technique. This technique creates biases across channels since each is transmitted at a distinct carrier frequency. These biases must be estimated and removed to provide the precise relative navigation solution of interest in this work []. While these processes are well researched [], they can add obscurity to other variables of interest and thus are not included in this work.

2.1 Space Segment

The main functions of the space segments are to generate and transmit code and carrier phase signals, and to store and broadcast the navigation message uploaded by the control segment. These transmissions are controlled by a highly stable atomic clocks allowing accurate timing knowledge to the nanosecond. Each constellation, has unique characteristics and will be discussed in the following sections to explain parameters and necessary knowledge needed to utilize their transmitted information.

2.1.1 GPS

The GPS satellites are arranged in six equally spaced orbital planes surrounding Earth, each with four "slots" occupied by baseline satellites. This 24-slot arrangement ensures there are at least four satellites in view at any point in time around the planet. The satellites are placed in Medium Earth Orbit (MEO) at an altitude of 20,200km and a nominal period of 11 hours, 58 minutes and 2 seconds.

GPS satellites are grouped by sets, or Blocks, launched within a specific time interval. The evolution of the technology is illustrated in figure 2.1 and is discussed in detail in the following passage

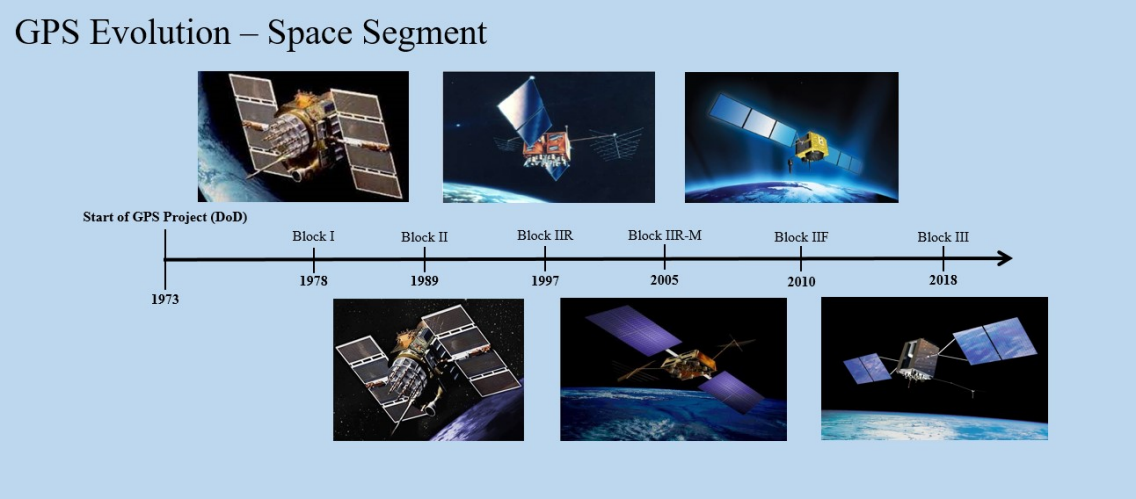

Figure 2.1: GPS Space Segment Evolution

Block I consisted of eleven satellites launched between 1978 and 1985. They had an average lifespan of 4.5 years and were capable of providing positioning services for three or four days without any contact with the control center. Block II consisted of 28 satellites launched from 1989 to 1990. They had an average lifespan of 6.5 years and could supply positioning services for 180 days without contact from the control segment. Block IIR were produced to replace Block II/IIA as they reached their life expectancy. These satellites were capable of determining their orbits and generating navigation messages internally. They could operate for half a year without support from the control segment with no degradation of ephemeris accuracy. Block IIR-M are the upgraded versions of the IIR block. They included a new military signal and the more robust L2C signal. The first Block IIR-M satellite was launched on

September 26, 2005. The first member of the Block IIF was launch on May 28, 2010. These satellites expanded on the existing capabilities by adding the L5 civil signal in a frequency band protected for safety-of-life applications. Lastly, Block III will introduce significant improvements in navigation capabilities by improving interoperability and jam resistance. They will also provide the fourth civil signal L1C on the L1 band.

2.1.2 Galileo

The Galileo constellation in Full Operational Capability (FOC) consists of 27 operational and 3 spare MEO satellites at an altitude of 2322km with an eccentricity of 0.002. Ten satellites will occupy each of the three orbital planes inclined at an angle of 56 degrees with respect to the equator. The satellites will be spread around each plane and will take about 14 hours, 4 minutes and 45 seconds to orbit the Earth. This constellation guarantees a minimum of six satellites in view from any point in time around the planet. The evolution of the Galileo space segment is illustrated in figure 2.2.

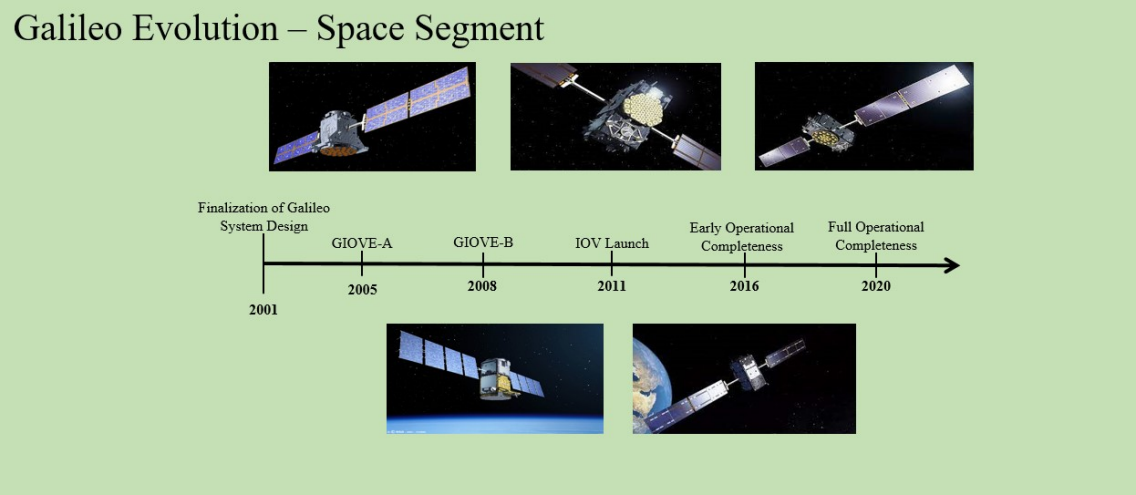

Figure 2.2: Galileo Space Segment Evolution

Two experimental satellites were launched between 2005 and 2008: the Galileo In-Orbit Validation (GIOVE) satellites GIOVE-A and GIOVE-B. GIOVE-A was launched on December 28, 2005. It has two redundant small-size rubidium atomic clocks with a stability of about 10ns a day. GIOVE-B was launched on April 27, 2008 with a more advanced payload. It uses 4 redundant clocks: two small rubidium atomic clocks with a stability of 10ns a day, and

two passive hydrogen master clocks with a higher stability of about 1ns a day. Two phases followed the experimental satellites: Galileo IOV and FOC phase. The IOV phase aimed at qualifying the Galileo space, ground and user segments through extensive in-orbit/on-ground tests. During this phase, four operational satellites complement the two experimental satellites already in orbit. The first two operational IOV satellites were launched on October 21, 2011 and placed in the first orbital plane. The next two were launched on October 12, 2012 in the second orbital plane. They combine two rubidium and two passive hydrogen master clocks with a powerful transmitter to broadcast precise navigation data. The FOC phase was reached in 2020 with a constellation of 27 operational satellites plus 3 spares.

2.1.3 BeiDou

The BeiDou constellation consists of 35 satellites including 5 Geostationary Orbit (GEO) satellites and 30 non-GEO satellites in a nearly circular orbit. The non-GEO satellites include three Inclined Geosynchronous Satellite Orbit (IGSO) pieces with an inclination of about 55 degrees and with an orbital period of about 12 hours and 53 minutes. The GEO satellites, orbiting at an altitude of about 35786km recently entered service in 2020. The general timeline of the BeiDou constellation is shown in 2.3.

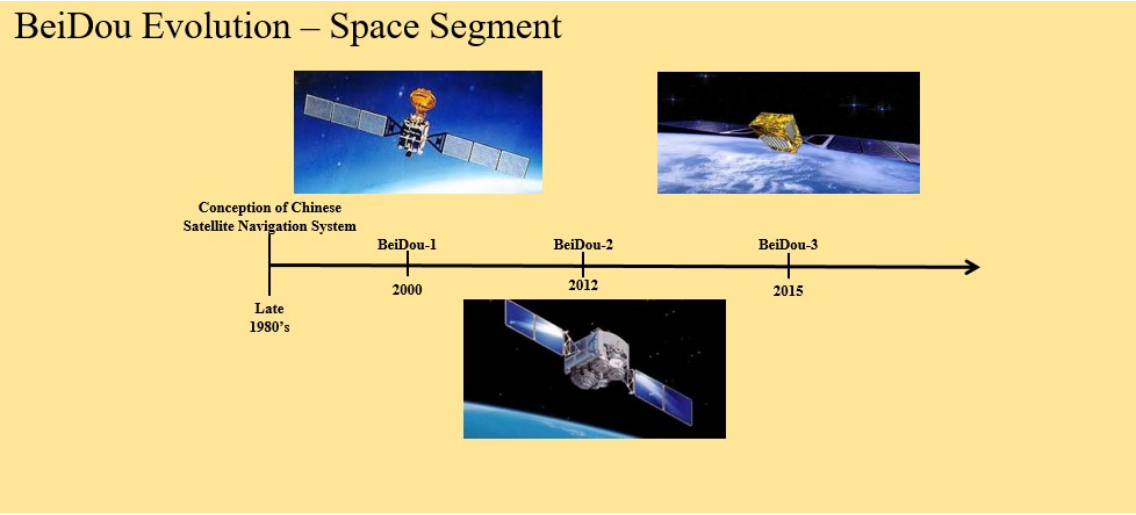

Figure 2.3: BeiDou Space Segment Evolution

There are three variants of BeiDou satellites: the geostationary BeiDou-G, the geosynchronous BeiDou-IGSO and the MEO BeiDou-M. They have a lifetime of eight years and are

based on the three-axis-stabilised DFH-3 platform []. The first BeiDou Phase II satellite in orbit was the experimental BeiDou-M satellite launched on April 14, 2007. By late December 2011, China had put four BeiDou-G and five BeiDou-IGSO satellites into orbit. By the end of 2012, there were five GEO, four MEO and five IGSO navigation satellites in orbit. The constellation of 35 satellites was completed in 2020.

2.2 Control Segment

The control segment is responsible for the proper operation of the GNSS. Its basic functions are:

- To control and maintain the status and configuration of the satellite constellation
- To predict ephemeris and satellite clock evolution
- To keep the corresponding GNSS time scale
- To update the navigation messages for all satellites

Again, each constellation is uniquely controlled and will be discussed individually.

2.2.1 GPS

The GPS control segment is composed of a network of Monitoring Stations (MS), a Master Control Station (MCS) and the Ground Antennas (GA). The MCS, located in Colorado Springs, USA is the core of the control segment. It is responsible for operating the system and providing command, control and maintenance services to the space segment. Recently, a new full functional backup station, known as the Alternate Master Control Station (AMCS), was set up as part of a modernization plan at Vandenberg Air Force Base.

The MS are distributed around the world. They are equipped with atomic clock standards and continuously log data for all the satellites in view. The collected data are sent to the MCS where they are processed to estimate satellite orbits, clock errors and to generate the navigation message. Originally, the MS network consisted of five stations located in Hawaii, Colorado Springs, Ascension Island, Diego Garcia, Kwajalein with Cape Canaveral being incorporated

in 2001. These stations were controlled and operated by the United States Air Force (USAF). In 2005, the modernization program expanded this network to include six new MS operated by the National Geospatial-Intelligence Agency (NGA) of the US Department of Defense (DoD). These were located in Adelaide, Australia; Buenos Aires, Argentina; Hermitage, United Kingdom; Manama, Bahrain; Quito, Ecuador; and Washington, DC. Five more stations were added in 2006 found in Fairbanks, Alaska; Osan, South Korea; Papeete, French Polynesia; Pretoria, South Africa; and Wellington, New Zealand. With this final addition, each satellite is seen from at least three MS improving system accuracy. Lastly, the GA uplink data to the satellites via S-band radio signals. This includes parameters estimated by the MCS in addition to command telemetry for each satellite to maintain its correct orbit.

2.2.2 Galileo

The Galileo ground segment controls the entire satellite constellation, the navigation system facilities and the dissemination services. The Full Operational Capabilities (FOC) involves two Ground Control Centre (GCC), five Telemetry, Tracking and Control (TTC) stations, nine Mission Uplink Stations (ULS) and a world-wide network Galileo Sensor Stations (GSS). The Ground Control Segment (GCS) is responsible for the constellation control and management of Galileo satellites. It provides the TTC function for the whole satellite constellation. Its functional elements are deployed within the GCC and the globally distributed TTC stations. The TTC stations use S-band frequency to provide a secure exchange of data between the control centers and satellites. The Ground Mission Segment (GMS) is responsible for the determination and uplink of the navigation and integrity data messages needed to provide the navigation and Universal Time Coordinate (UTC) time transfer service. The GMS includes a worldwide network of GSS continuously collecting data to be processed by the GCC for determining Galileo navigation and integrity data messages. The GCCs constitute the core of the control segment. They are located in Fucino, Italy and Oberpafaffenhofen, Germany and the main functions are as follows:

- Orbit determination and synchronization

- Control of all Galileo satellites and uploading navigation data messages
- Monitoring, maintenance and control of satellites and ground segment elements
- Computation of Galileo System Time (GST) and provision of a reliable and stable coordinated time reference for the Galileo System

2.2.3 BeiDou

The BeiDou Control consists of a single Master Control Station (MCS) responsible for satellite constellation control and processing measurements sent by the Monitoring Stations (MS) for parameter estimation. Upload stations (US) are in charge of uploading the orbital corrections and the navigation message to the satellites. Lastly, the MS collect observables from the BeiDou satellites in view from their locations.

2.3 User Segment

GNSS receivers compose the user segment. Their primary purpose is to receive GNSS signals, determine observables, and solve navigation equations to obtain position and velocity information of the user at a precise time. GNSS satellites continuously transmit signals at two or more frequencies in the L band. Each constellation accomplishes this feat in unique ways, and thus the following sections will further discuss the signal characteristics for each of the aforementioned constellations.

2.3.1 GPS Signals

The legacy GPS signals are transmitted on two radio frequencies in the L band referred to as Link 1 (L1) and Link 2 (L2). They are right-hand circularly polarized and their frequency is derived from a fundamental frequency of 10.23MHz generated by on-board atomic clocks. The GPS uses the CDMA technique to send different signals on the same radio frequency, and the modulation method used is Binary Phase Shift Keying (BPSK). Modernization of the GPS system began in 2005 with the launch of the first IIR-M satellite. This satellite supported the new military M signal and the second civil signal L2C. The L2C signal is modulated onto the

L2 Carrier frequency and broadcasted at higher effective power level than the original L1 C/A signal. This, coupled with its powerful cross-corrrelation properties, facilitates tracking with large signal-level variations from satellite to satellite, making reception easier in high multipath environments. The GPS modernization plan continued with the launch of the Block IIF satellites which introduced the third civil signal on the L5 band. This signal has two components, both modulated via BPSK onto the carrier. This signal has improved code/carrier tracking loop and high transmit power which provides further robustness to interference. Lastly, its higher chipping rate than the L1 C/A code provides superior multipath performance. The next step in modernization involves the Block III satellites which will provide the fourth civil signal on the L1 band (L1C). This signal uses Multiplexed Binary Offset Carrier (MBOC) modulation to improve reception in cities and other challenging environments. Characteristics of signals of interest are shown in table 2.1.

Link	Carrier Freq. (MHz)	PRN Code	Modulation Type	Data Rate (bps)	Service
L1	1575.420	C/A	BPSK(1)	50	Civil
L2	1227.6	P	BPSK(10)	50	Military
L5	1176.450	L5-I	BPSL(10)	50	Civil

Table 2.1: Studied GPS Signal Characteristics

For the navigation piece of information transmitted by GPS satellites, the Keplerian parameters are with respect to the space vehicle's (SV) antenna phase center in the WGS 84 ECEF coordinate system defined at the SV's local estimate of GPS time. The WGS 84 model is comprised of estimated planetary parameters describing the eccentricity, diameter, and rotational rates of the Earth. GPS time runs parallel to Coordinated Universal Time (UTC) which is based on Greenwich Median Time (GMT) with the exception that GPS time is a continuous time scale. It is expressed in GPS weeks and GPS seconds with the start date acknowledged at January 6, 1980. Ellipsoidal parameters for WGS 84 are provided in Table 2.2.

2.3.2 Galileo Signals

In the FOC phase, each satellite in the constellation will transmit 10 navigation signals in the frequency bands E1, E6, E4a, and E5b, each right-hand circularly polarized and transmitted

Semi-major axis of the ellipse	a	6378137.0m
Flattening Factor	f	1/298,257233563
Earth's Angular Velocity	w_E	7292115.0*$10^{-11} rad/s$
Gravitational Constant	μ	3986004.418*$10^8 m^3/s^2$
Speed of Light in Vacuum	c	2.99792458*$10^8 m/s$

Table 2.2: WGS 84 Ellipsoidal Parameters

using the CDMA technique. For this work, only the Open Service (OS) signals are discussed. The other signals, Public Regulated Service (PRS) and Commercial Service (CS), are intended for authorized users only. They provide improved robustness to jamming and spoofing or additional observables for more consistent position and velocity information. E1-B and E1-C are OS signals with unencrypted ranging codes. The MBOC modulation is used for the E1-B and E1-C signals which is implemented by the Composite Binary Offset Carrier (CBOC). E51 is an OS signal and includes two signal components: a data channel, E5a-I and a pilot channel E5a-Q. The E5a signal has unencrypted ranging codes and navigation data which is accessible to all users. This signal shares the frequency space with GPS L5, BeiDou B2a and future GLONASS L5 signals. E5b is a OS signal and similarly, consists of a E5b-I data channel and E5b-Q pilot channel. Its shares a frequency space with BeiDou B2b and GLONASS G3. Interestingly, the E5a and E5b signals are modulated onto a single E5 carrier frequency at 1191.795 MHz using a technique known as Alternate Binary Offset Carrier (AltBOC). When assessed correctly, the E5 single can be processed as a single large-bandwidth signal which results in a low-multipath and tracking noise signal.

Band	Carrier Freq. (MHz)	PRN Code	Modulation Type	Data Rate (bps)	Service
E1	1575.420	E1-B	BOC_{cos}(15,2.5)	125	OS,CS,SoL
E5a	1176.45	E5a-I	BPSK(10)	50	OS
E5b	1207.14	E5b-I	BPSK(10)	50	OS,CS,SoL

Table 2.3: Studied Galileo Signal Characteristics

In the IOV phase, the initial coordinates for the reference stations were in the WGS 84 reference frame. But as the Galileo constellation matured and entered it FOC phase, the Galileo Terrestrial Reference Frame (GTRF) was already being validated and made compatible to the

International Terrestrial Reference Frame (ITRF). The ITRF was introduced by the International Earth Rotation and Reference Systems Service (IERS) and is updated every year. The GTRF, along with all other terrestrial reference frames, must agree with the ITRF to within 3cm (2σ). Conveniently, the newest realization of WGS 84 based on GPS data set G1762 adopted the ITRF2008 coordinates for more than half of the reference stations and velocities of nearby stations. This made the conversion between ITRF and WGS 84 agree at the centimeter level; which by default make GTRF and WGS 84 coincident as well. Thus, they share the same geodetic parameters. Similar to GPST, Galileo System Time (GST) is a continuous time scale and is synchronised to the International Atomic Time (TAI) with a nominal offset below 50 ns. The GST start epoch was on August 22, 1999.

2.3.3 BeiDou Signals

BeiDou Phase II/III satellites will transmit right-hand circularly polarized signals centered on three radio frequencies in the L band referred to as B1, B2, and B3 bands. Similar to Galileo, the BeiDou constellation has encrypted signal for authorized users which provide more robust position and velocity information. Again, only the OS signals will be discussed here. Like GPS, Galileo or the new GLONASS signals, BeiDou ranging signals are based on the CDMA technique. The B1-I signal is modulated onto a 1561.098MHz carrier frequency. Its modulated using the QPSK technique. A B1-Q signal exists but only authorized users can use its information. The B2-I, or B2b signal is sent on a 1207.14MHz signal and modulated using the BPSK technique. Similarly, a B2-Q signal exists but its availability is limited to authorized users.

Band	Carrier Freq. (MHz)	PRN Code	Modulation Type	Service
B1	1561.098	B1-I	QPSK(2)	Open
B2	1207.14	B2-I	BPSK(10)	Open

Table 2.4: Studied BeiDou Signal Characteristics

The BDS adopts the BeiDou Coordinate System (BDCS) whose definition complies with the standards of the International Earth Rotation and Reference (IERS). The definition is also consistent with that of the China Geodetic Coordinate System 2000 (CGCS2000). BDS and CGCS2000 have the same reference ellipsoid parameters. The origin is located at the Earth's

center of mass. The Z-axis is the direction of the IERS Reference Pole (IRP). The X-axis is the intersection of the IERS Reference Meridian (IRM) and the plane passing through the origin and normal to the Z-axis. The Y-axis, together with Z-axis and X-axis, constitutes a right-handed orthogonal coordinate system. BeiDou Time (BDT) is also a continuous time scale. It is synced to UTC within 100ns and started on Jaunuary 1, 2006.

Semi-major axis of the ellipse	a	6378137.0m
Flattening Factor	f	1/298.257222101
Earth's Angular Velocity	w_E	7292115.0*$10^{-11} rad/s$
Gravitational Constant	μ	3986004.418*$10^8 m^3/s^2$
Speed of Light in Vacuum	c	2.99792458*$10^8 m/s$

Table 2.5: CGCS2000 Ellipsoidal Parameters

Chapter 3

Real-Time Kinematic

Studying the user segment furthermore, we can begin processing the observables from each satellite in view in order to compute position and velocity information. For this work, the pseudoranges and carrierphase measurements from satellites in view of two GNSS receivers are used to construct the ambiguity search space. The ambiguities present in the carrierphase measurements must be resolved to provide the most precise relative navigation solution. The use of differential techniques with the carrierphase observable is coined real-time kinematic (RTK) positioning. RTK considers the observables between two GNSS receivers: a static base station with accurate knowledge of its own position and a kinematic rover unit. Since the base station can acknowledge errors in perceived observables from accurate knowledge of its own position. These errors can be sent to rover units as corrections to account for atmospheric and satellite clock errors. This method of RTK positioning can achieve sub-meter absolute positioning accuracy, but there are some limitations. First, the rover units must be able to receive the corrections at all times of interest meaning that an internet connection or radio communication is required. Secondly, if a problem occurs at the base station (i.e. maintenance, equipment damage, etc..) corrections can not be sent to the rover units. Lastly, base stations are not always in range (within the 25km radius of effectiveness). While RTK positioning is an effective method for precise positioning, its limitations can be troublesome. In 2003 however, a new method was developed that improved the reliability of RTK while maintaining the high level of precision expected when using the carrierphase observables [1]. This technique was called Dynamic Real-Time Kinematic positioning. It still relied on two GNSS systems but removed the static constraint on the base station. Furthermore, since the base station's absolute

position was no longer well known, this technique relied on specific observable combinations that removed common modes of error from the system observables. In doing so, the problem no longer considers the absolute position of the rover but its relative position with respect to the mobile base station. This technique is discussed in detail in this chapter while also demonstrating its capabilities in a variety of settings.

3.1 DRTK

The Dynamic Real-Time Kinematic (DRTK) algorithm was originally developed in [1]. Its utility comes from its ability to provide centimeter level accurate relative positioning between two platforms with shared communications. It is a multi-stage process but for simplicity, its more critical stages are illustrated in figure 3.1.

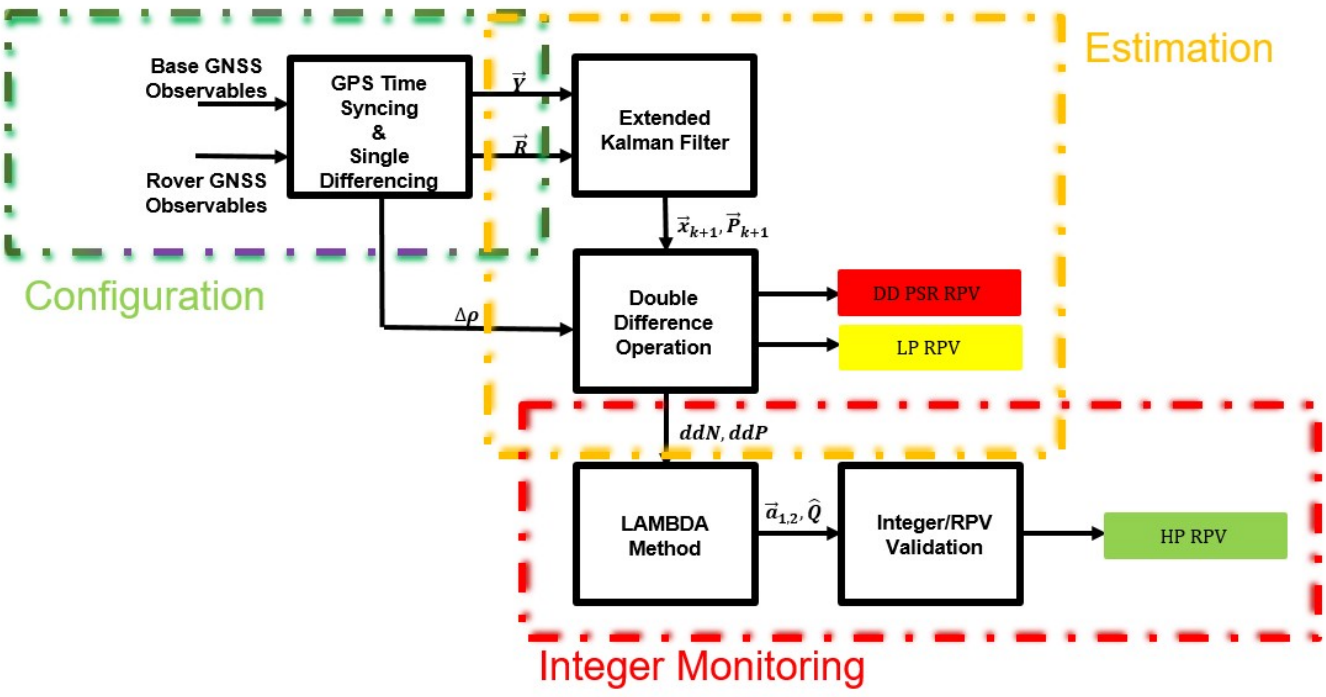

Figure 3.1: DRTK Block Diagram

The configuration section syncs measurements across platforms and forms necessary measurement combinations from the shared observables. This necessary combination is discussed in section 3.1.2 and is used by a discrete extended Kalman filter in the estimation section of the algorithm. The formulation and initialization of this filter is discussed in section 3.1.3 and

3.1.4. The double difference operation is the final stage before a relative navigation solution can be provided. At this stage, two solution are available to the user and are discussed in section 3.1.5. The LAMBDA method is critical in providing the most accurate solution and is the final step in resolving the AR of the problem. The integer validation metrics are discussed in detail in section 3.1.6. The calculation of the high precision (HP) RPV is discussed in 3.1.7.

3.1.1 Un-Differenced Measurement Models

The mathematical model for the code and carrier based range measurements are shown below in Equation 3.1.

$$\begin{cases} \tilde{\rho}_a^j = \mid \rho_a^j \mid + c(\delta t_a - \delta t^j) + T^j + I^j + M_\rho + \eta_a^{j,DLL} \\ \tilde{\psi}_a^j = \mid \rho_a^j \mid + c(\delta t_a - \delta t^j) + T^j - I^j + \lambda N_a^j + M_\psi + \eta_{ab}^{j,PLL} \end{cases} \tag{3.1}$$

Where $\tilde{\rho}_a^j$ is the measured range from receiver a to satellite j, $\tilde{\psi}_a^j$ is the carrierphase from receiver a to satellite j, c is the speed of light, $|\rho_a^j|$ is the true range from receiver a to satellite j, T is the troposhperic delay, I is the Ionospheric advancement or delay, δt_a is the receiver clock errors, δt^j is the satellite clock errors, λN_a^j is the integer ambiguity or phase bias, M are the multipath effects, and η is the measurement noise. For this work, the carrierphase measurement is of interest due to its precision and multipath resistance. However, several steps must be taken before the carrierphase observables can be used to estimate relative position. This includes forming specific observable combinations to improve the observability of the integer ambiguities, estimating float-level ambiguity estimates, and fixing the float estimates to their correct integer value.

3.1.2 Single Difference Measurement Models

The integer ambiguity is better observed in specific combinations of the GNSS observables. A specific combination, called the Single Difference (SD) measurement, is able to remove common modes of error between observables from satellites in view to both receivers. The geometric interpretation of the single difference measurement is shown in Equation 3.2.

$$\begin{cases} \Delta\rho_{ab}^{j} = |\rho_{ab}^{j}| + cb_{a,b} + \eta_{ab}^{j,DLL} \\ \Delta\psi_{ab}^{j} = |\rho_{ab}^{j}| + cb_{a,b} + \Delta N_{ab}^{j} + \eta_{ab}^{j,PLL} \end{cases} \tag{3.2}$$

Where ρ_{ab}^{j} is the baseline between the GPS antennas, cb_{ab} is the relative clock bias, and ΔN_{ab}^{j} are the SD ambiguities present in the carrierphase observable. The non-deterministic term (η) is a function of CNO and receiver characteristics. These terms can be statistically quantified by determining the accuracy of the delay-lock loop (DLL) and phase-lock loops (PLL). Standard formulations for DLL and PLL can be seen in [1]. Assessing Equation 3.2, the atmospheric errors and satellite clock bias are removed. This is due to strong spatial and temporal correlation between measurements. Another artifact of this combination is the summation of the receiver clock bias and the conversion of the geometric range to the relative range between the phase centers of the two antenna. The remaining deterministic term is the SD ambiguity term in the carrierphase model. Note that it is more isolated especially when considering that the remaining deterministic terms are already observed in the SD pseudorange model. It should be noted, that while we take a step towards removing the ambiguity term from the carrierphase measurement; the statistical uncertainty associated with each measurement is increased. This is due to differencing or summing independent Gaussian random variables which sums the uncertainty of both terms in the operation.

3.1.3 Kalman Filter Floating Point Ambiguity Resolution

In this methodology, a recursive estimation process can be used to take advantage of the constant nature of the ambiguity present in the carrierphase. Here, we use a discrete Extended Kalman Filter (EKF). Recursive estimation of these constant integers coupled with the symmetric nature of the covariance matrix allows this to be an effective method for estimating integer ambiguities.The state vector is demonstrated in 3.3.

$$\vec{x} = \begin{bmatrix} \Delta X \\ \Delta Y \\ \Delta Z \\ cb_{ab}^{j} \\ \Delta N_{ab}^{1} \\ \vdots \\ \Delta N_{ab}^{j} \end{bmatrix} \tag{3.3}$$

Where ΔX, ΔY, ΔZ are the relative positions states in the Earth centered Earth Fixed reference frame, cb_{ab}^{j} is the relative clock bias and ΔN_{ab}^{j} are the SD ambiguities for each tracked channel used in the filter. The measurements used by the filter are the SD observables. These are organized as shown in Equation 3.7.

$$\vec{z} = \begin{bmatrix} \vec{y}_{\rho} \\ \vec{y}_{\psi} \end{bmatrix} \tag{3.4}$$

$$\vec{y}_{\rho} = \begin{bmatrix} \Delta\rho_{k}^{1}, GPS \\ \vdots \\ \Delta\rho_{k}^{i}, GPS \end{bmatrix} \tag{3.5a}$$

$$\vec{y}_{\phi} = \begin{bmatrix} \Delta\psi_{k}^{1}, GPS \\ \vdots \\ \Delta\psi_{k}^{i}, GPS \end{bmatrix} \tag{3.5b}$$

The measurement model used in the filter must fit the form:

$$\vec{z}(t) = h(x(t)) + w_{m}(t) \tag{3.6}$$

Where h(x(t)) is a nonlinear function of the state vector and $w_m(t)$ is the statistical uncertainty of the measurements. In GNSS applications, this nonlinear function is procedurally computed at every observation period and is known as the geometry matrix []. The geometry matrix

consists of unit vectors whose origin is about the phase center of the ground antenna and points to the phase center of the satellite antenna with respect to the X,Y,Z axis of the ECEF coordinate frame []. The last common term is the relative receiver clock bias. It should be noted that for multi-constellation applications, the clock bias term will be unique for each constellation. The ambiguity term is unique to the carrierphase observables and thus will populate the lower right diagonal of the holistic geometry matrix. The complete geometry matrix is shown below:

$$H = \begin{bmatrix} H_{x,y,z}^{GPS} & 1 & 0_{nxm} \\ H_{x,y,z}^{GPS} & 1 & \lambda_{L1} I_{nxm} \end{bmatrix} \tag{3.7}$$

$w_m(t)$ is the statistical uncertainty associated with the system inputs. The matrix is populated along its diagonal with the calculated accuracy from $\eta_{ab}^{j,DLL}$ and $\eta_{ab}^{j,PLL}$ and is shown in equation 3.6. It should be noted that for this algorithm, thermal noise is the considered noise source which is characterized with $w_m(t) \sim (\sigma_{ab}^{DLL,PLL}, 0)$.

$$R = \begin{bmatrix} \sigma_{ab}^{1,DLL} & 0 & 0 & 0 & 0 & 0 \\ 0 & \ddots & 0 & 0 & 0 & 0 \\ 0 & 0 & \sigma_{ab}^{j,DLL} & 0 & 0 & 0 \\ 0 & 0 & 0 & \sigma_{ab}^{1,PLL} & 0 & 0 \\ 0 & 0 & 0 & 0 & \ddots & 0 \\ 0 & 0 & 0 & 0 & 0 & \sigma_{ab}^{j,PLL} \end{bmatrix} \tag{3.8}$$

Note the repetition of positional unit vectors and clock biases in the left most section of Equation 3.5. This symmetry allows us to rewrite Equation 3.4 in a vector/matrix format.

$$Z(t) = H_{2mx4} \begin{bmatrix} \vec{r}_{AB} \\ c\delta t_{AB} \end{bmatrix} + \begin{bmatrix} 0_{mxm} \\ \lambda I_{mxm} \end{bmatrix} \Delta N_{mx1} \tag{3.9}$$

As stated before, the goal of the observer is to estimate SD ambiguities. Thus, the position, receiver clock biases and geometry are unnecessary and only add computational load to the algorithm. The left null space of H_{2mx4} can be used to uncouple the unneeded information

from the measurements, geometry matrix and measurement weighting matrix which is later defined. This has been used rigorously in [4,5,6,7]. The left null space is defined as:

$$L\bar{H}_{2mx4} = 0 \tag{3.10}$$

Applying the left null space to Equation 3.9 gives the simplified expression:

$$LZ(t) = L \begin{bmatrix} 0_{mxm} \\ \lambda I_{mxm} \end{bmatrix} \Delta N_{mx1} \tag{3.11}$$

$$H_{integer} = L \begin{bmatrix} 0_{mxm} \\ \lambda I_{mxm} \end{bmatrix} \tag{3.12}$$

The state vector, now consisting only of the SD ambiguity estimates are mapped to the measurement domain using $H_{integer}$ shown in 3.12. R is also altered becoming:

$$R = LRL^T \tag{3.13}$$

With these matrices and vectors updated, the measurement update within the Kalman filter can be completed. For completeness, the calculation of the Kalman gain, state a posteriori update and state covariance update are defined below:

$$K = P_k^- H^T (H P_k^- H^T + R)^{-1} \tag{3.14}$$

$$\hat{x}_k^+ = \hat{x}_k^- + K(z - H\hat{x}_k^-) \tag{3.15}$$

$$P_k^+ = (I - KH)P_k^- \tag{3.16}$$

The ambiguities found in the carrierphase are constant assuming no cycle slips occur between observation periods. This makes defining the time update relatively simple since no

dynamic exist to be modeled and the process noise is uncorrelated among the distinct channels. The state transition matrix can thus be defined with an identity matrix:

$$\Phi = I_{mxm} \tag{3.17}$$

The process noise dictates the size of the search space assessed in the measurement update. If we assume that little uncertainty is added to the system after the time update, then we can apply small values along the diagonal to prevent the filter from "going to sleep". But as will later be seen in the paper, there are platforms which benefit from increasing the process noise values from their standard values used in prior work [4,5,6,7]. It is defined as:

$$Q = G_P \Delta t I_{mxm} \tag{3.18}$$

Where G_P is a constant value typically set to a very small number $1\text{e}{-6} <= G_p <= 100\text{e}{-6}$, and Δt is the sampling time. With these defined, the time update can propagate the state vector and estimated state uncertainty forward in time while respecting system dynamics and uncertainty associated with the considered states.

$$\hat{x}_k^- = \Phi \hat{x}_{k-1}^+ \tag{3.19}$$

$$P_k^- = \Phi P_{k-1}^+ \Phi^T + Q \tag{3.20}$$

There exist moments in time where the covariance matrix can become non-symmetric due to constellation changes or excessive tuning to filter parameters [4,5,6]. A simple operation can be computed should this error occur and is defined as follows:

$$P = \frac{1}{2}(P + P^T) \tag{3.21}$$

3.1.4 Initialization

For this work, the SD ambiguity estimates are initialized by differencing SD pseudoranges by SD carrierphase observables and converting these values to units of cycles. This is expressed below:

$$\vec{x}_{k-1}^{+} = \begin{bmatrix} (\Delta\rho_k^1 - \Delta\psi_k^1)/\lambda, GPS \\ \vdots \\ (\Delta\rho_k^i - \Delta\psi_k^i)/\lambda, GPS \end{bmatrix} \tag{3.22}$$

As stated previously, the covariance matrix is initialized based on the user knowledge of uncertainty in estimated state initialization. Cross correlation is ignored at this stage and it was found that for high grade equipment, that a standard deviation of half a cycle was sufficient. For low grade equipment, higher values up to 5 cycles were needed to acknowledge the increase in state uncertainty caused by lower grade internal oscillators.

3.1.5 Double Difference

The previous section discusses the utilization of SD observables to help isolate and subsequently estimate SD ambiguities. But, a common mode of error across channels still obscures the ambiguity search space preventing complete isolation of the ambiguity. The culprit, the relative receiver clock bias, can be removed by the double difference operation. A single channel, preferably the highest in elevation, can be chosen as the base satellite. The satellite highest in elevation is chosen since it travels through the least amount of atmosphere and thus contains minimal amounts of atmospheric distortion to obscure the ambiguity information. The remaining channel observables and geometric information is differenced from the base satellite's equivalent information to form the double difference observables and geometry matrix. These are defined below:

$$\begin{cases} \nabla\Delta\rho_{ab}^j = |\rho_{ab}^j| + \eta_{\nabla,ab}^{j,DLL} \\ \nabla\Delta\psi_{ab}^j = |\rho_{ab}^j| + \nabla\Delta N_{ab}^j + \eta_{\nabla,ab}^{j,PLL} \end{cases} \tag{3.23}$$

The double difference operation is a linear operation and assuming the first satellite is highest on the horizon, the resulting matrix operator is shown below:

$$D = \begin{bmatrix} 1 & -1 & 0 & 0 & 0 \\ 1 & 0 & -1 & 0 & 0 \\ 1 & 0 & 0 & -1 & 0 \\ 1 & 0 & 0 & 0 & -1 \end{bmatrix} \tag{3.24}$$

The DD operation is performed on the SD ambiguity estimates and the error covariance matrix.

$$\hat{N}_Z = D\Delta N \tag{3.25}$$

$$\hat{P}_Z = DP_k^+ D^T \tag{3.26}$$

3.1.6 Integer Validation

The double differenced float ambiguity estimates need to be rounded to their correct integer value to achieve the highest possible precision. Because of the high correlation between states and error covariances, simple rounding schemes or boot-strapping approaches are not sufficient to consistently integerize the float estimates to their correct values. The LAMBDA method was introduced in [2] and has been experimentally validated for many years. LAMBDA stands for Least-squares AMBiguity Decorrelation Adjustment. It is a two stage process that considers the DD estimates and the error covariance matrix after the measurement update. The first stage is the decorrelation of the ambiguities by means of the Z-transform to create new ambiguities and error covariances.

$$z = Za_{\nabla\Delta} \tag{3.27}$$

$$\hat{z} = Z\hat{a}_{\nabla\Delta} \tag{3.28}$$

$$Q_{\hat{z}} = ZP_{\hat{a}_{\nabla\Delta}}Z \tag{3.29}$$

Where z are the true transformed ambiguities, Z is the transformation matrix, $a_{\nabla\Delta}$ are the true DD differenced ambiguities, $\hat{z}$ are the transformed estimated ambiguities, $\hat{a}_{\nabla\Delta}$ are the DD float ambiguities, $Q_{\hat{z}}$ is the transformed covariance matrix, and $P_{\hat{a}_{\nabla\Delta}}$ is the DD covariance matrix. This step improves the efficiency of the search step in the LAMBDA method. It also allows the new ambiguities to retain their integer characteristics shown in Equation 3.28 and maintain the volume search space of the original problem [2]. The next step is searching the transformed search space for the real valued solution. This is considered through the integer least-squares (ILS) problem:

$$min. \quad (\hat{z} - \tilde{z})Q_{\hat{z}}^{-1}(\hat{z} - \tilde{z}) \quad with z \in Z^n \tag{3.30}$$

The search must yield the grid point that is nearest to the real valued estimate, with nearness measured in the metric of the variance-covariance matrix [2]. For this work, MATLABs LAMBDA function was used to conduct this stage in the DRTK algorithm [35]. The Integer Least Squares with integrated ratio validation was used for the work. The ratio test is a discrimination test: it tests the closeness of the float solution to the optimal integer solution compared to the other integer candidates [35]. It is defined in Equation 3.31.

$$\frac{F(\hat{a})}{F(\hat{a}')} \quad \leq \quad \mu \tag{3.31}$$

Where μ is the threshold value which holds for $0 \leq \mu \leq 1$. $\hat{a}'$ is the integer vector that returns the second smallest cost expressed in Equation 3.30 and $\hat{a}$ is the integer set that returns the smallest cost expressed in Equation 3.30. Even with these internal validation metrics, it is still possible for the ILS to converge to the incorrect integer set. With this in mind, a common method for consistency is to apply an additional ratio which takes the form :

$$\frac{(\hat{z}_2 - \tilde{z})Q_{\hat{z}}^{-1}(\hat{z}_2 - \tilde{z})}{(\hat{z}_1 - \tilde{z})Q_{\hat{z}}^{-1}(\hat{z}_1 - \tilde{z})} \quad \leq \quad \kappa \tag{3.32}$$

It is the inverse of Equation 3.31 and so the threshold is valid for $1 \leq \kappa \leq \infty$. A threshold of 3 is typically considered as a validation metric when using the ratio test [1]. Again, this test evaluates the closeness of the candidate set to the float solution. An additional metric known as the Ambiguity Dilution of Precision (ADOP) was introduced in [4]. It is an easy-to-compute diagnostic value that measures the intrinsic model strength for successful ambiguity resolution [8]. The ADOP is defined as:

$$ADOP = \sqrt{|Q_{\hat{a}\hat{a}}|}^{\frac{1}{n}} \tag{3.33}$$

With n being the number of DD ambiguities, $Q_{\hat{a}\hat{a}}$ is the ambiguity variance matrix and $|\cdot|$ denotes the determinant. The ADOP has several properties that make it an important diagnostic tool. First, it is invariant against the choice of ambiguity parametrization. All admissible ambiguity transformations can be shown to have a determinant of one, thus the ADOP does not change when one changes the definition of the ambiguities. Secondly, it measures the volume of the ambiguity confidence ellipsoid. And third, the ADOP equals the geometric mean of the standard deviations of the ambiguities when the ambiguities are completely decorrelated. Since the LAMBDA method produces ambiguities that are largely decorrelated, the ADOP approximates the average precision of the transformed ambiguities [8]. Since the ADOP gives a good approximation to the ILS ambiguity success rate, we can define p_{ADOP} to evaluate the candidate set covariance. It has been shown that ADOP values smaller than 0.12 cycles corresponds to an ambiguity success rate greater than 0.999 [8].

$$P_{ADOP} \approx [2\Phi\frac{1}{2ADOP} - 1]^n \tag{3.34}$$

Where n is the number of DD ambiguities and Φ is the standard normal cumulative distribution. Figures showing P_{ADOP} as a function of ADOP can be found in [8]. Lastly, should a candidate set of integers pass LAMBDA's thresholds and the secondary ratio test; a valid candidate set is only chosen if the the same candidate set is found for a series of consecutive observation periods. This is a form of integrity monitoring to ensure only the correct integer set is chosen and used in the RPV calculation. This consecutive counter threshold is termed the consecutive

ambiguity counter (CAC). For the results discussed in this thesis, a CAC threshold of 10 was used. This value was chosen due to its consistency across equipment grade and data sets and is further discussed in appendix section A.1.

3.1.7 High Precision RPV Estimation

A weighted least squares (WLS) operation is used to determine the a precise RPV once a set of candidate integer estimates have been selected. The geometric expression is shown below:

$$r_{AB} = [G_{\nabla\Delta}^T R_{\nabla\Delta\Phi}^{-1} G_{\nabla\Delta}]^{-1} G_{\nabla\Delta}^T R_{\nabla\Delta\psi}^{-1} (\nabla\Delta\psi_{AB} - \lambda I \nabla\Delta\tilde{N}) \tag{3.35}$$

Where r_{AB} is the estimated RPV, $G_{\nabla\Delta}$ is the DD geometry matrix, $R_{\nabla\Delta}$ is the DD measurement uncertainty This expression can be used to provide the float level solution and the much nosier DD pseudorange RPV solution. Where $\nabla\Delta\tilde{N}$ is replaced with the float estimates and where $(\nabla\Delta\Psi_{AB} - \lambda I \nabla\Delta\tilde{N})$ is replaced with the DD pseudorange observables.

3.2 DRTK: Good Performance

The DRTK algorithm was developed for GPS only dual frequency scenarios. With this in mind, this section demonstrates the capabilities of algorithm during a zero-baseline test while using survey-to-mid grade equipment. Three points will be made by demonstrating key aspects of the filter and its performance. The experiment set-up can be seen in figure 3.2. The zero-baseline experiment used a Novatel PWRPAK 7 GNSS receiver and a Piksi Multi evaluation receiver receiving RF signal from a dual frequency, multi-GNSS antenna.

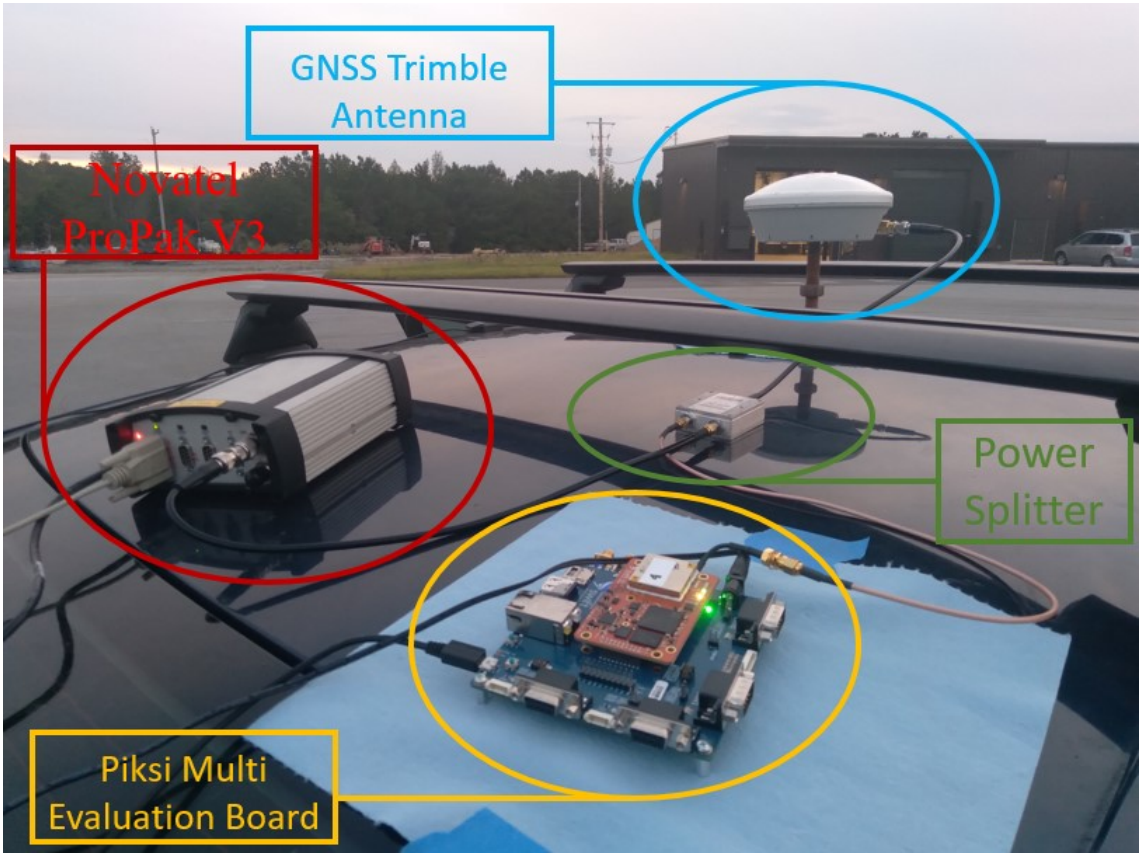

Figure 3.2: Zero-Baseline Test with Survey-Grade Antenna: Experiment Set-Up

First, lets consider the accuracy of the fixed integer solution. This is shown by plotting the time series of the estimated RPV of a zero-baseline test in figure 3.3. This type of experiment helps demonstrate the quality of the carrierphase measurements since no relative range information is contained within the inputs.

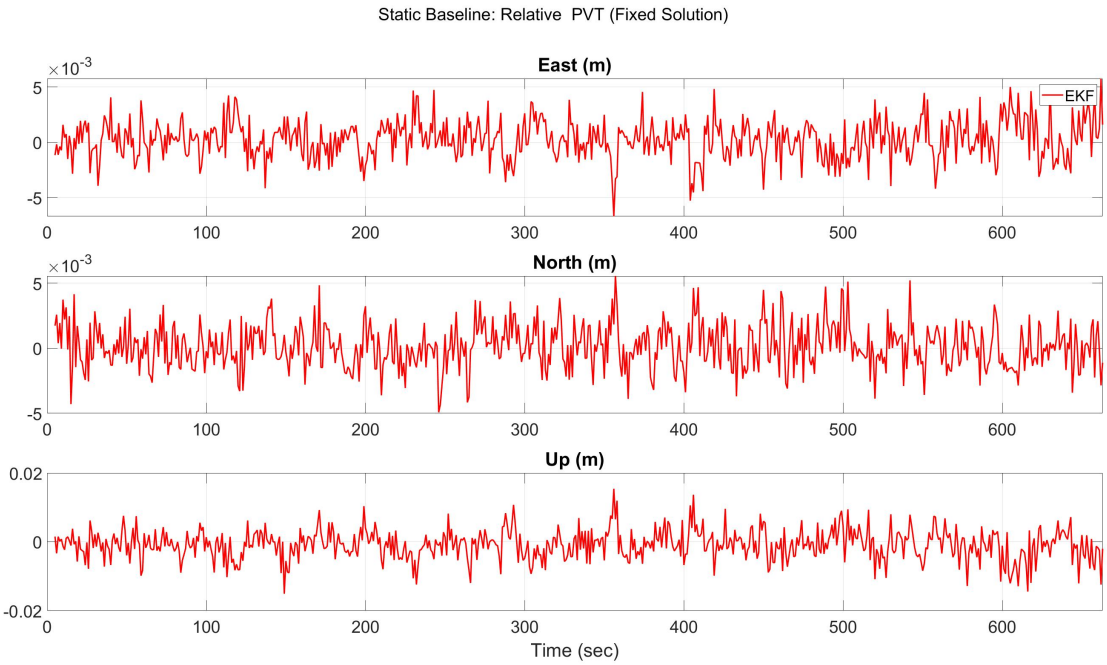

(a)

Figure 3.3: Zero-Baseline with Survey-Grade Antenna: Estimated HP-RPV

Millimeter level accuracy is maintained for the entirety of the 10 minute experiment. The time to first fix (TTFF) was approximately 10 seconds into the data set. The importance of correctly fixing the ambiguity estimates can be easily instilled by observing the float level solution and the noisier pseudorange solution shown in figure 3.4.

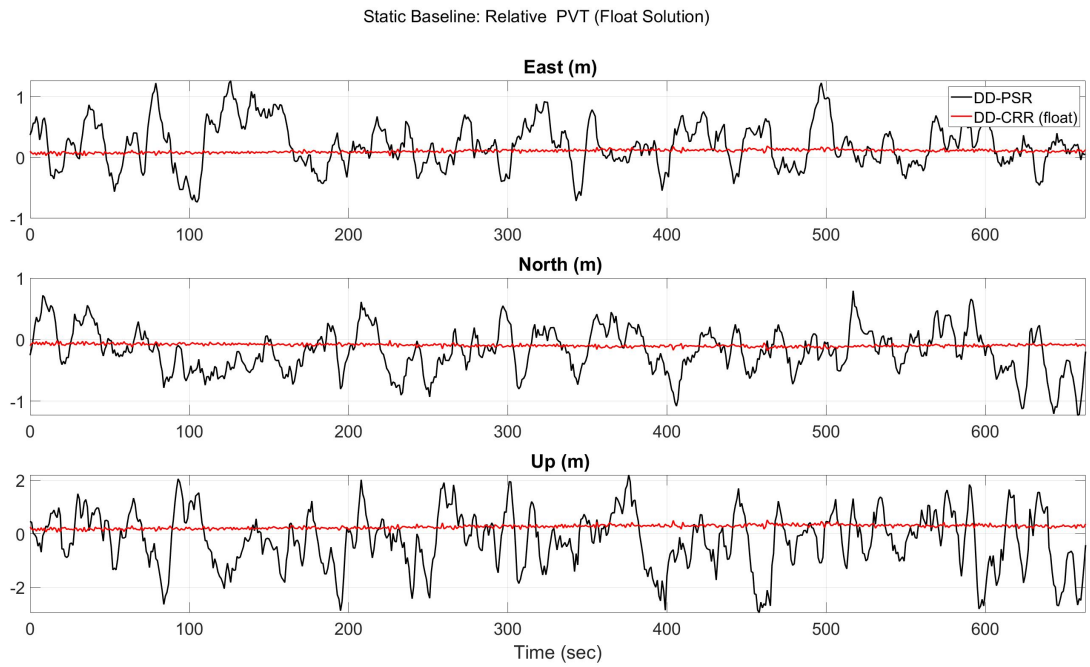

(a)

Figure 3.4: Zero-Baseline with Survey-Grade Antenna: DD-PSR and Float RPV

Note the variance of the DD-PSR solution. This is not only attributed to the accumulation of uncertainty collected through the SD and DD operations but also by the high levels of noise inherent to the pseudorange measurements. Also note that the float estimates, while more accurate and precise than the PSR solution, is still incorrect and even biased in every axis.

The last aspect of interest is the algorithms integer validation stage. To study this piece, we can first look at the inputs to the RPV estimation stage of the algorithm. The insight this provides is unique to the zero-baseline tests since the signal, at this point in the algorithm, contains only the DD integer ambiguities with Gaussian noise.

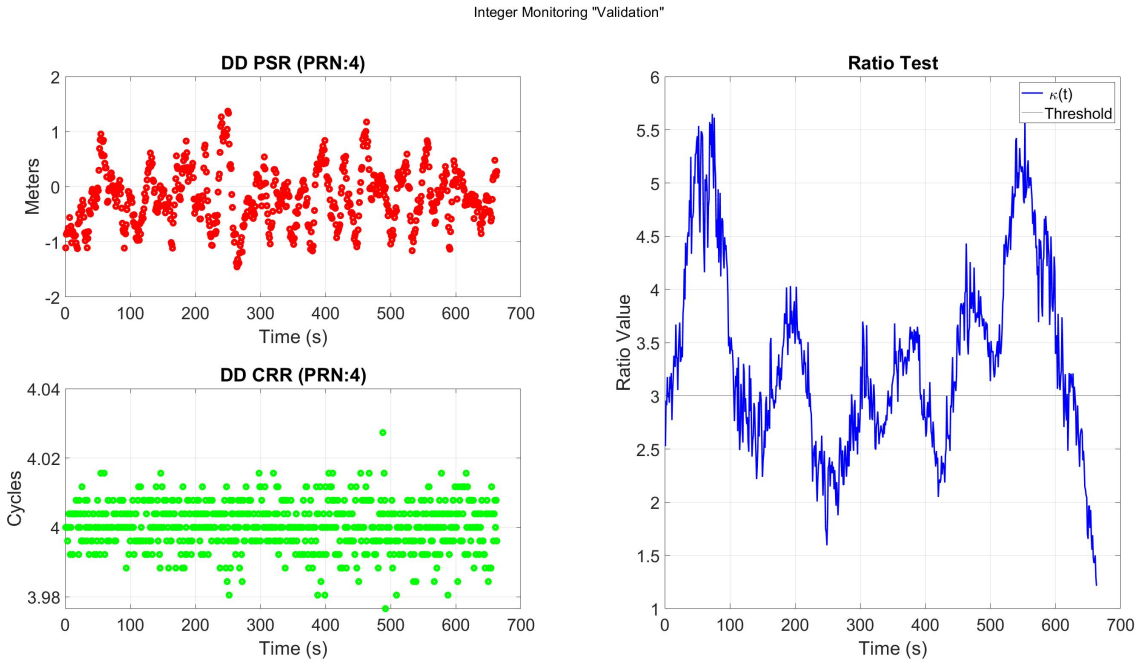

(a)

Figure 3.5: Zero-Baseline Test with Survey-Grade Antenna: Integer Monitoring Metrics

The integer ambiguity corrupting the DD carrierphase observable can be clearly identified as 4 cycles from the time series alone. The filter has extended periods of confidence in its candidate sets but fails to pass the threshold for the entire data set.

A notable change in filter performance can be observed however by only considering L1 measurements. The resulting HP-RPV estimates are shown in 3.4. It should be noted that while TTFF did increase by nearly 400 seconds, the precision of the estimated RPV was maintained.

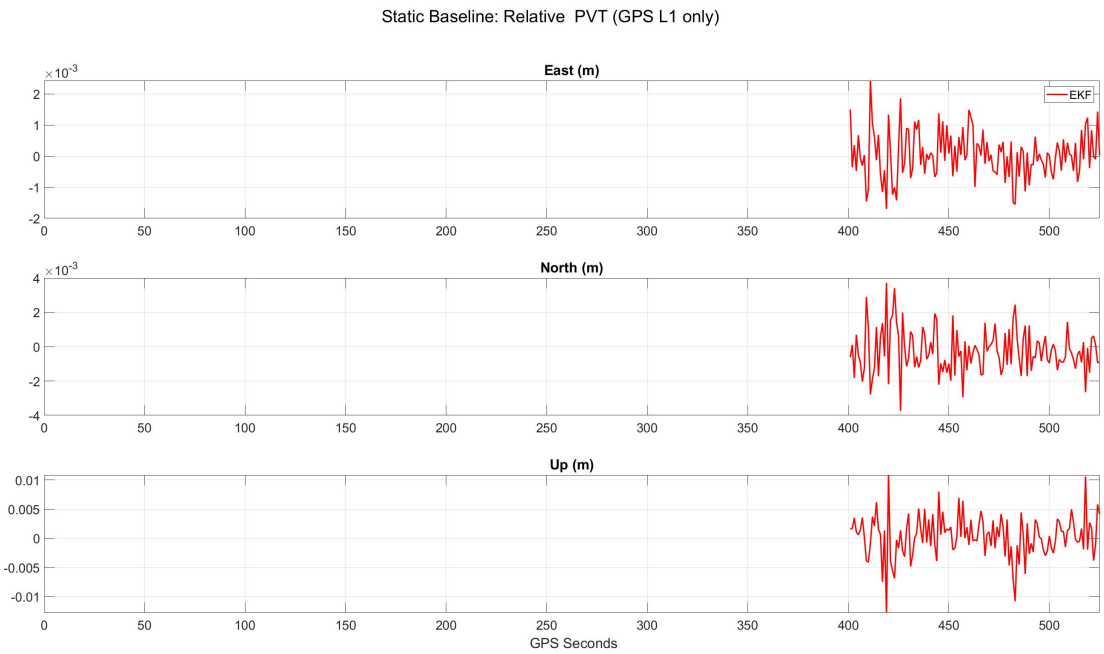

Figure 3.6: Zero-Baseline with Low-Cost Antenna: Fixed RPV

A significant change can be observed in the float and pseudorange solutions in figure 4.2. The float solution is seen to be bias but slowly converge to the truth. More notable however is the increase in the pseudorange solution variance. This is due to less measurements being available to be weighted and thus reduce error in the resulting LS RPV estimation.

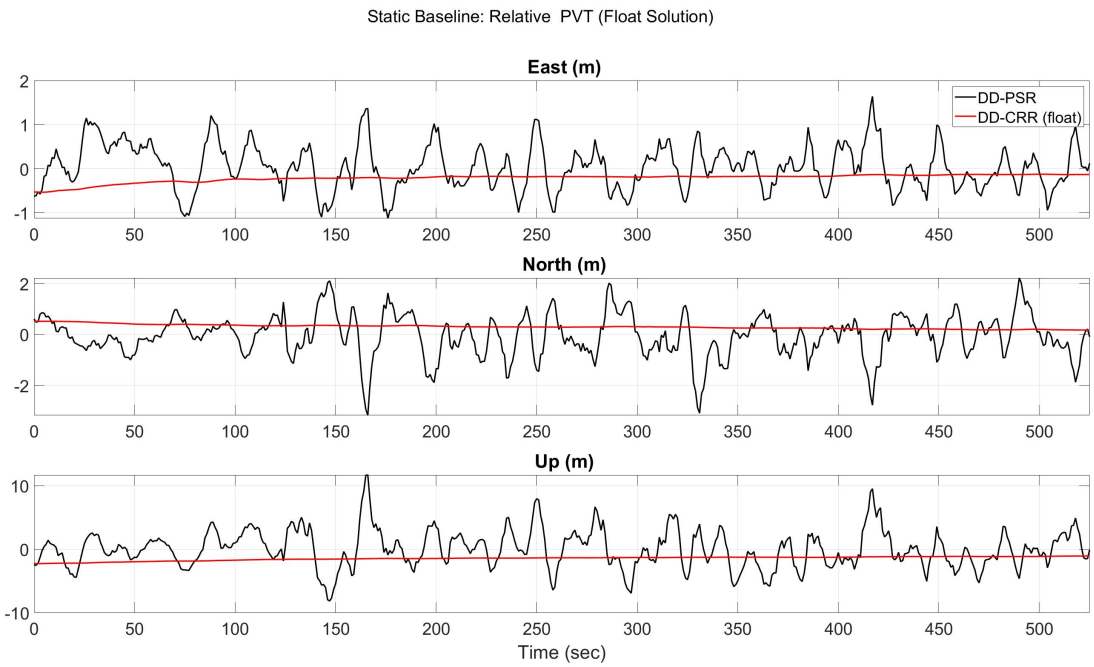

Figure 3.7: Zero-Baseline with Low-Cost Antenna: DD-PSR and Float RPV

Lastly, our integer monitoring can be inspected by observing the time series of the the DD observables and ratio test. Again, the DD ambiguities can be observed within the carrierphase measurements. In addition, the confidence of the DD ambiguity estimates is significantly lower for the single frequency case.

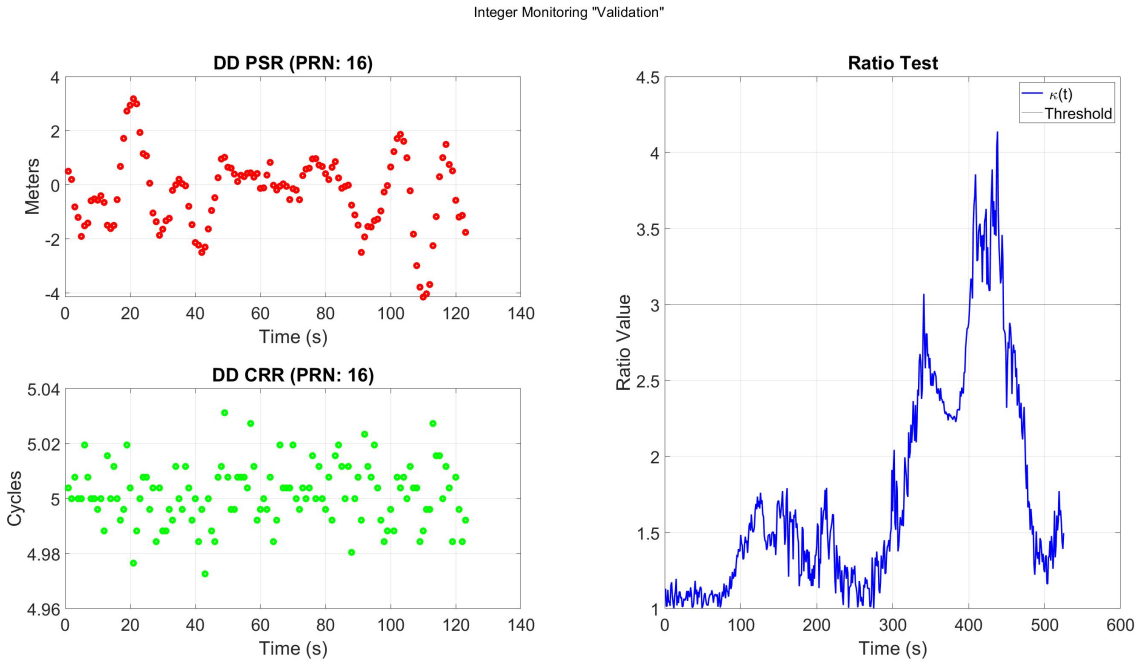

Figure 3.8: Zero-Baseline with Low-Cost Antenna: Integer Monitoring Metrics

3.3 DRTK: Mid Performance

This section uses the same GNSS receivers discussed in the previous section but changes the survey grade antenna to a low-cost Ublox patch antenna. Again, the DRTK algorithm attempts to resolve the integer ambiguities in order to provide the HP-RPV. The experiment set-up is shown in figure 3.9.

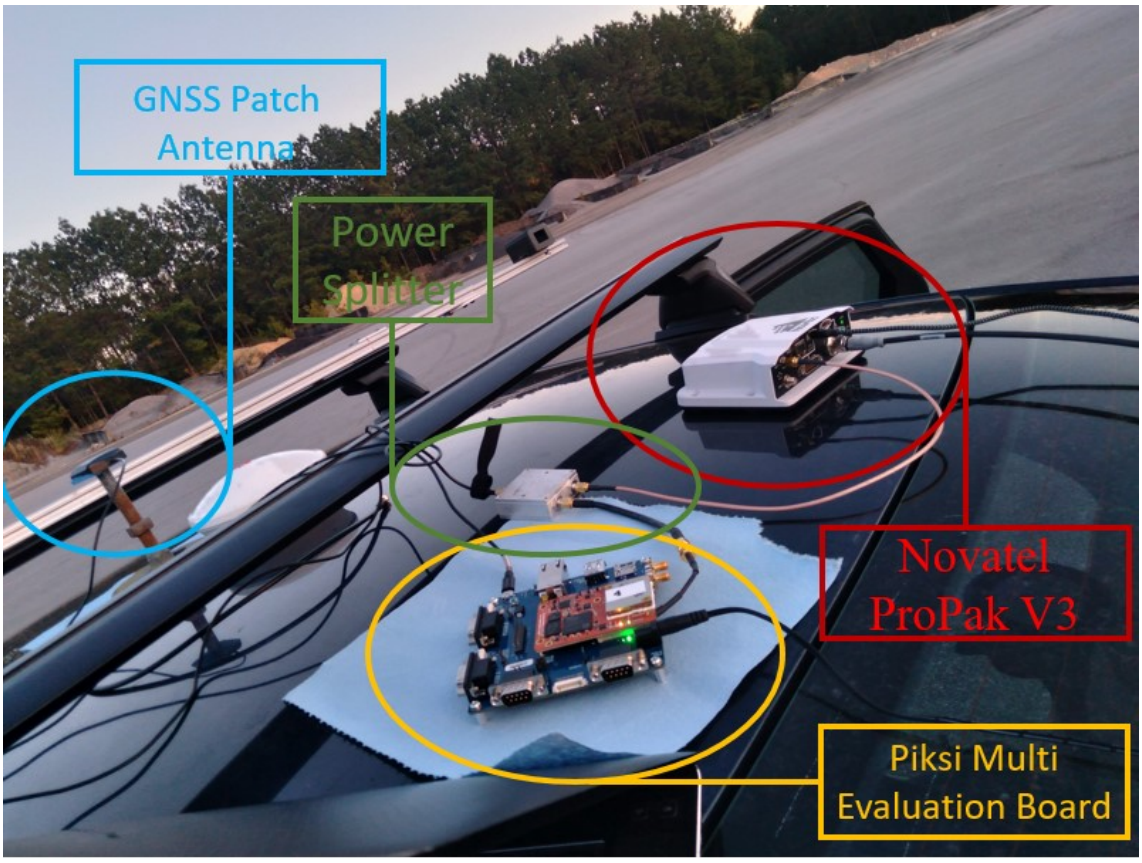

Figure 3.9: Zero-Baseline Test with Low Cost Antenna: Experiment Set-up

The Ublox patch antenna is a single frequency multi-GNSS antenna however, similar performance metrics are not observed when compared to the single frequency case from the previous section. This phenomenon is discussed in greater detail in the adaptive estimation section of the thesis but the results of the ratio test are shown in 3.10 to demonstrate the significant difference made by the antenna change. The filter only momentarily passes the ratio test showing a significant lack of confidence in the ambiguity estimates.

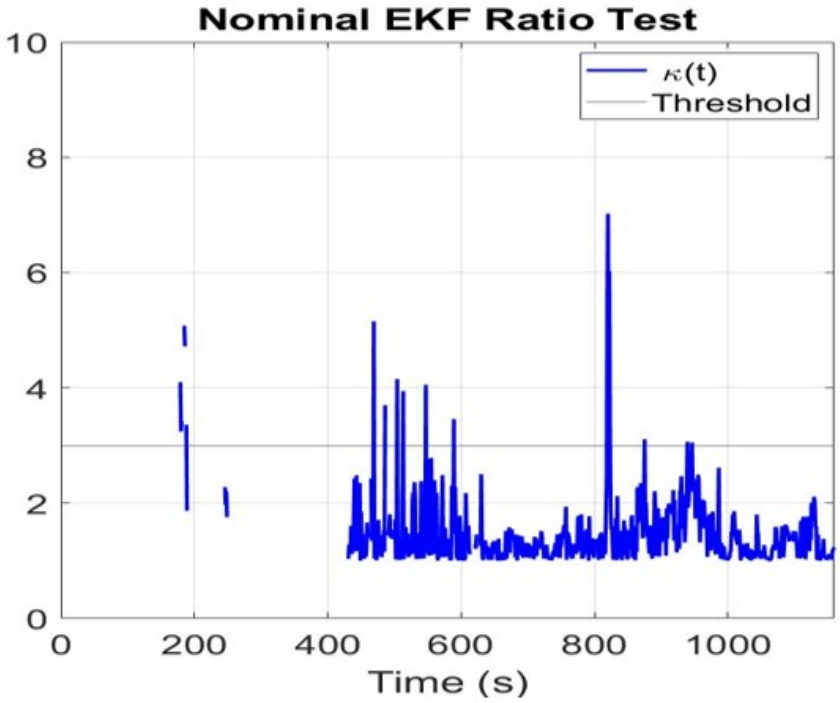

Figure 3.10: Zero-Baseline Test with Low Cost Antenna: Experiment Set-up

Another artifact of the inaccurate ambiguity estimates are the periods in which no candidates sets are provided by the LAMBDA method. These periods exist during 0 to 200 seconds and 225 to 425 seconds in figure 3.10.

3.4 DRTK: Poor Performance

For this section, we continue using the patch antenna but switch the Piksi Evaluation board with a low-cost Ublox EVK-M8T receiver. This receiver uses a TCXO internal oscillator which causes high levels of noise to be present in its computed measurements [29]. This can make it almost impossible to resolve the integer ambiguities for on-the-fly AR. Researchers have utilized stochastic methods for improving the AR in these conditions but require large amounts of data and does not ensure correct integer fixing. Using the traditional DRTK algorithm, the filter is unable to correctly fix integers. It is still able to provide the float and pseudorange solution but again, fixed integer precision is desired. The time series of the measurements are seen in figure 4.4:

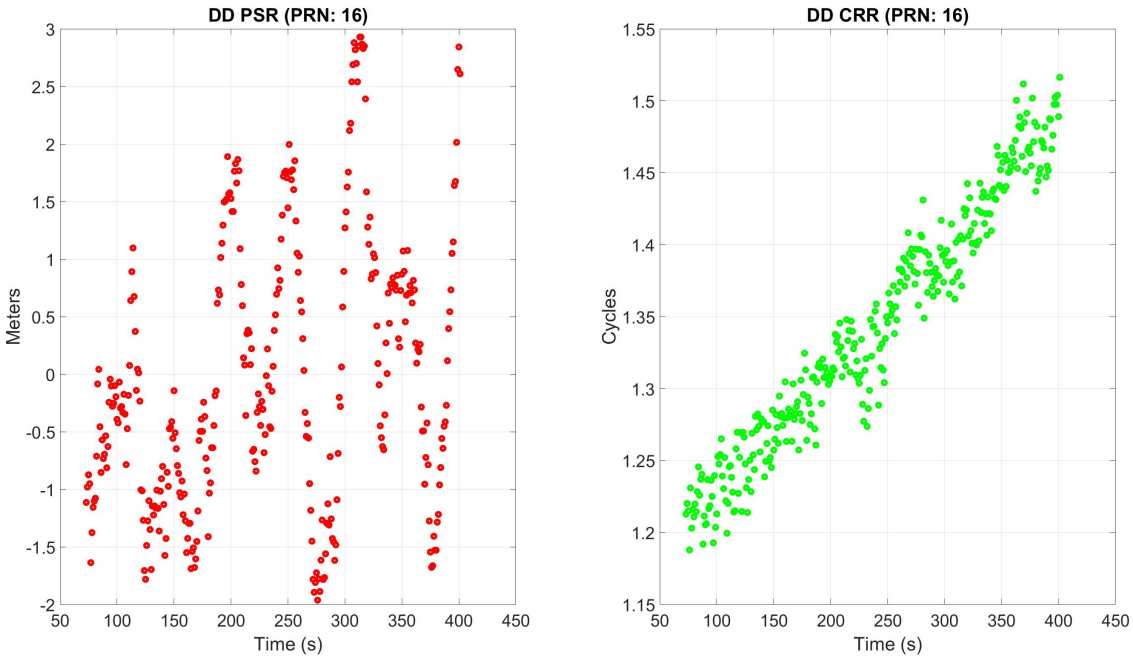

Figure 3.11: DD Observables from a Low-Cost Receiver

The affects of the clock error are easily observed in the DD carrierphase time series. This drift, in addition to the high level of uncertainty present in the pseudorange observables, prevent the DRTK algorithm from providing high precision capabilities.

This chapter of the thesis discusses the DRTK algorithm and demonstrates its capabilities in unique scenarios. It is important to understand how algorithms respond in ideal and non-ideal circumstances involving expected measurements and used equipment. While the algorithm works well when using survey-to-mid grade equipment, it loses its ability to provide HP-RPV solution when using low-cost equipment. This needs to be investigated to determine whether precise relative positioning is achievable under these low-cost sensor suite constraints.

The need for precise relative positioning is greater now more then ever. With that in mind, it is important to understand how the algorithm behaves under non-ideal circumstances (i.e. when survey-grade equipment is not available). The next chapter discusses advancements to the DRTK algorithm that allows for improved performance under multiple considered sensor suites.

Chapter 4

Advancements in DRTK

This chapter begins exploring how improvements can be made to the DRTK algorithm allowing it to provide HP-RPV estimates in several use cases where it has been previously shown incapable to do so. The investigation begins by augmenting the nominal DRTK architecture to include single frequency information from GPS, Galileo, and BeiDou constellations. Next, adaptive estimation of measurement uncertainty is integrated to the DRTK algorithm to improve the AR when using low-cost antennas. Lastly, a tightly-coupled DGPS/UWB algorithm is demonstrated to provide HP-RPV estimates when using low-cost receivers and antennas. Each method is studied by comparing filter performance and integer validation metrics.

4.1 Multi-GNSS DRTK

GPS, while accurate in open-sky environments, is prone to intermittent dropouts and degraded accuracy due to satellite availability. Multi-GNSS aims to solve this consistency issue by incorporating multiple constellations into a single architecture. This increases the number of observables available and thus, the availability of GNSS positioning.

4.1.1 Filter Design

To demonstrate the augmentation of the Galileo and BeiDou constellations into the DRTK algorithm, a single frequency example is considered. The states for the multi-GNSS DRTK filter are given in Equation 4.1.

$$\vec{x} = \begin{bmatrix} \Delta X \\ \Delta Y \\ \Delta Z \\ cb^{j}_{ab,GPS} \\ cb^{j}_{ab,GAL} \\ cb^{j}_{ab,BDS} \\ \Delta N^{1}_{ab,GPS} \\ \vdots \\ \Delta N^{j}_{ab,GPS} \\ \Delta N^{1}_{ab,GAL} \\ \vdots \\ \Delta N^{j}_{ab,GAL} \\ \Delta N^{1}_{ab,BDS} \\ \vdots \\ \Delta N^{j}_{ab,BDS} \end{bmatrix} \tag{4.1}$$

These states are mapped to the measurement domain with the following observation matrix:

$$H = \begin{bmatrix} H^{GPS}_{x,y,z} & 1 & 0 & 0 & 0_{nxm} & 0_{nxm} & 0_{nxm} \\ H^{GAL}_{x,y,z} & 0 & 1 & 0 & 0_{nxm} & 0_{nxm} & 0_{nxm} \\ H^{BDS}_{x,y,z} & 0 & 0 & 1 & 0_{nxm} & 0_{nxm} & 0_{nxm} \\ H^{GPS}_{x,y,z} & 1 & 0 & 0 & \lambda_{L1} I_{nxm} & 0_{nxm} & 0_{nxm} \\ H^{GAL}_{x,y,z} & 0 & 1 & 0 & 0 & \lambda_{E1} I_{nxm} & 0_{nxm} \\ H^{BDS}_{x,y,z} & 0 & 0 & 1 & 0 & 0_{nxm} & \lambda_{B1} I_{nxm} \end{bmatrix} \tag{4.2}$$

It should be noted that dual and even triple frequency implementations can be considered by designing the filter with a similar formulation as [1]. This is generalized in Equation 4.3.

$$H = \begin{bmatrix} H_{x,y,z,cb}^{GPS,L1} & 0_{nxm} & 0_{nxm} & 0_{nxm} & 0_{nxm} & 0_{nxm} & 0_{nxm} \\ H_{x,y,z,cb}^{GAL,E1} & 0_{nxm} & 0_{nxm} & 0_{nxm} & 0_{nxm} & 0_{nxm} & 0_{nxm} \\ H_{x,y,z,cb}^{BDS,B1} & 0_{nxm} & 0_{nxm} & 0_{nxm} & 0_{nxm} & 0_{nxm} & 0_{nxm} \\ H_{x,y,z,cb}^{GPS,L2} & 0_{nxm} & 0_{nxm} & 0_{nxm} & 0_{nxm} & 0_{nxm} & 0_{nxm} \\ H_{x,y,z,cb}^{GAL,E2} & 0_{nxm} & 0_{nxm} & 0_{nxm} & 0_{nxm} & 0_{nxm} & 0_{nxm} \\ H_{x,y,z,cb}^{BDS,B2} & 0_{nxm} & 0_{nxm} & 0_{nxm} & 0_{nxm} & 0_{nxm} & 0_{nxm} \\ H_{x,y,z,cb}^{GPS,L1} & \lambda_{L1} I_{nxm} & 0_{nxm} & 0_{nxm} & 0_{nxm} & 0_{nxm} & 0_{nxm} \\ H_{x,y,z,cb}^{GAL,E1} & 0_{nxm} & \lambda_{E1} I_{nxm} & 0_{nxm} & 0_{nxm} & 0_{nxm} & 0_{nxm} \\ H_{x,y,z,cb}^{GPS,B1} & 0_{nxm} & 0_{nxm} & \lambda_{B1} I_{nxm} & 0_{nxm} & 0_{nxm} & 0_{nxm} \\ H_{x,y,z,cb}^{GPS,L2} & 0_{nxm} & 0_{nxm} & 0_{nxm} & \lambda_{L2} I_{nxm} & 0_{nxm} & 0_{nxm} \\ H_{x,y,z,cb}^{GAL,E2} & 0_{nxm} & 0_{nxm} & 0_{nxm} & 0_{nxm} & \lambda_{E2} I_{nxm} & 0_{nxm} \\ H_{x,y,z,cb}^{GPS,B2} & 0_{nxm} & 0_{nxm} & 0_{nxm} & 0_{nxm} & 0_{nxm} & \lambda_{B2} I_{nxm} \end{bmatrix} \tag{4.3}$$

Lastly, the inputs provided to the filter from each constellation and are organized below:

$$\vec{x} = \begin{bmatrix} \vec{y}_\rho \\ \vec{y}_\phi \end{bmatrix} \tag{4.4}$$

$$\vec{y}_\rho = \begin{bmatrix} \Delta\rho_k^1, GPS \\ \vdots \\ \Delta\rho_k^i, GPS \\ \Delta\rho_k^1, GAL \\ \vdots \\ \Delta\rho_k^i, GAL \\ \Delta\rho_k^1, BDS \\ \vdots \\ \Delta\rho_k^i, BDS \end{bmatrix} \tag{4.5a}$$

$$\vec{y}_\phi = \begin{bmatrix} \Delta\phi_k^1, GPS \\ \vdots \\ \Delta\phi_k^i, GPS \\ \Delta\phi_k^1, GAL \\ \vdots \\ \Delta\phi_k^i, GAL \\ \Delta\phi_k^1, BDS \\ \vdots \\ \Delta\phi_k^i, BDS \end{bmatrix} \tag{4.5b}$$

Similar to Equation 3.9, the left null space of Equation 4.2 can be used to extract the non-essential information from matrices and vectors of interest. The operation from the nominal DRTK algorithm is thus used here to consider only the SD ambiguity estimates.

4.1.2 Experimental Results

As shown previously, the quality of the signal perceived by the receiver affects the ability to estimate the high-precision RPVs. This quality is not only affected by equipment grade but by platform dynamics. Thus, we assess the improvement to performance for both static and dynamic baselines when utilizing the multi-GNSS DRTK algorithm and compare it to stand alone GPS only equivalent implementations.

4.1.2.1 Static Baseline

The static test show-cases the ability of the filter to extract ambiguity information when the geometric range between antennas is non-zero and static. Some features that provide insight to signal quality and observability of the ambiguities include the Carrier-to-Noise Desnity Ratio (CNO) value and ambiguity resolution index (ARI). The CNO ratio is defined as the ratio of the received modulated carrier signal power to the received noise power [8]. The ARI value is a

diagnostic tool for assessing the observability of the integer ambiguities embedded in the carrierphase observables. It is the difference between consecutive measurements across observation periods and is described in Equation 4.6.

$$ARI_k^j = (\rho_k^j - \rho_{k-1}^j) - \lambda(\psi_k^j - \psi_{k-1}^j) \tag{4.6}$$

Where ρ_k^j and ψ_k^j are the pseudorange and carrierphase observable for the current sampling epoch in cycles.

To compare GPS only to multi-GNSS DRTK, a short static baseline is examined. The experiment setup is shown in Figure 4.1

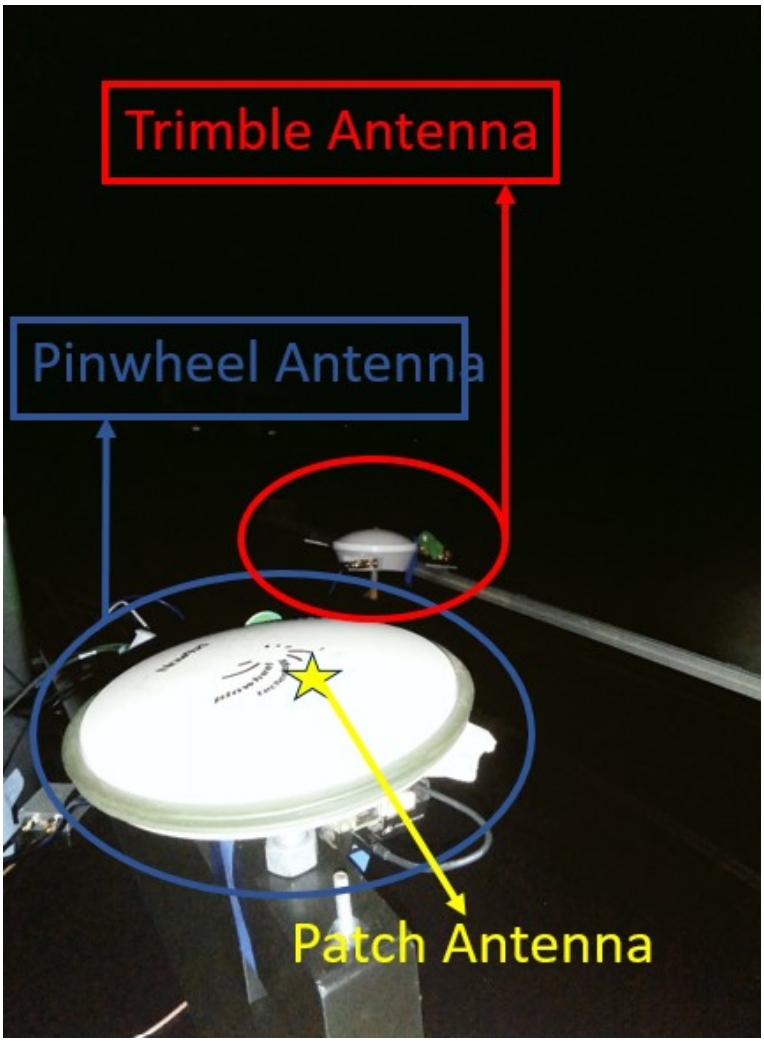

Figure 4.1: Static-Baseline Test with Survey-Grade Antenna: Experiment Set-Up

The 'base' module is a Novatel PWRPAK7 with a Trimble survey-grade antenna. The rover consisted of a Piksi Evaluation Board with a survey-grade Novatel Pinwheel antenna. The CNO ratios are depicted below for all visible satellites:

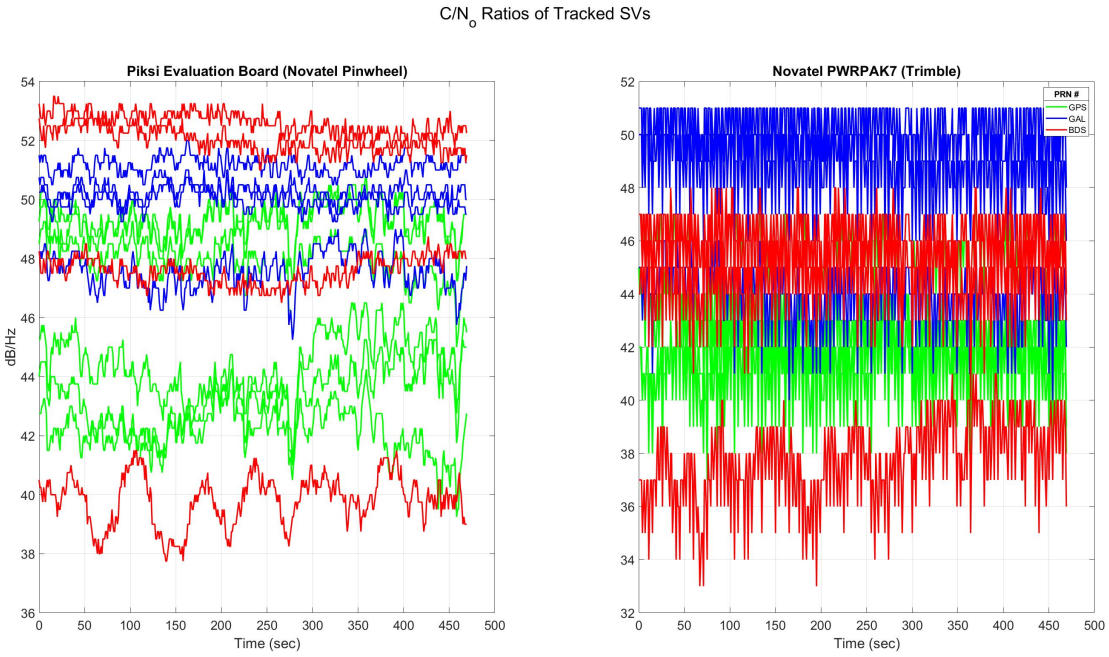

Figure 4.2: Static Baseline Test with Survey-Grade Antennas: CNO Ratios

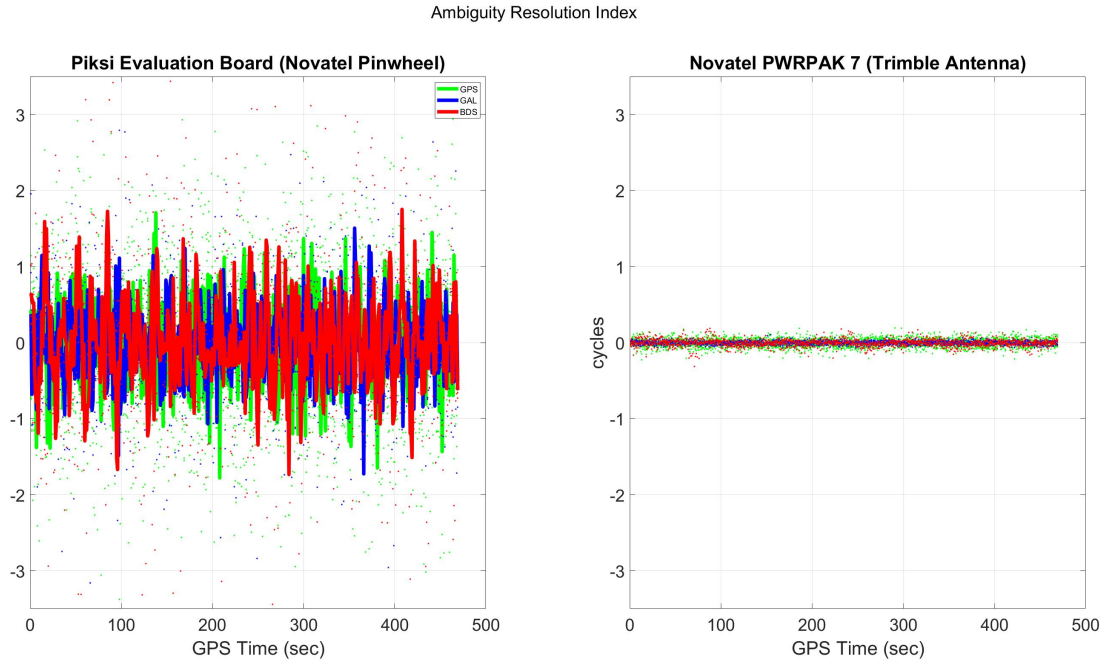

Figure 4.3: Static Baseline Test with Survey-Grade Antennas: ARI Values

The difference in GNSS system quality between platforms is clearly seen from the diagnostic figures above. Note the difference in magnitude of each platform's ARI value. This can be attributed to the receiver and antenna quality on each platform. During this test, no cycle slips were reported by the receiver or observed in the measured ARI values of any channel. Another key element to note is the ARI precision across constellations. It shows that the bottle neck for many RTK or DRTK applications is the equipment. Research has shown that a benefit from multi-GNSS solution comes from the improvement in dilution of precision (DOP) from incorporating different constellations [8]. This can be assessed by comparing the various DOP parameters for the GPS only and multi-GNSS implementations with a 0 degree mask angle. This comparison is shown below:

Configuration @ 0°	HDOP	PDOP	VDOP
GPS only	1.5781	1.8555	0.9760
Multi GNSS	1.1457	1.4095	0.8209

Table 4.1: Multi-GNSS DOP Comparison

A 0 degree elevation mask angle was used since two of the BeiDou satellites were low on the horizon and triple constellation was desired. This improved geometry provides a slight benefit to the SD ambiguity estimation since the positional information can be more easily distinguished from the floating point ambiguity estimates. To demonstrate this, the residual error from the Kalman filter can be observed. The residual error can be thought of as the error between a set of measurements and our state estimates mapped to the measurement domain, and is given in Equation 4.7.

$$\xi_k = z - Cx^k_{apriori} \tag{4.7}$$

Where z is the set of observables used in the measurement update, C is the observation matrix detailed in Equation 4.2, and $x^k_{apriori}$ is the set of current best state estimates before the measurement update. The SD residual error for the GPS only implementation and the multi-GNSS implementation can be seen in the Figures below:

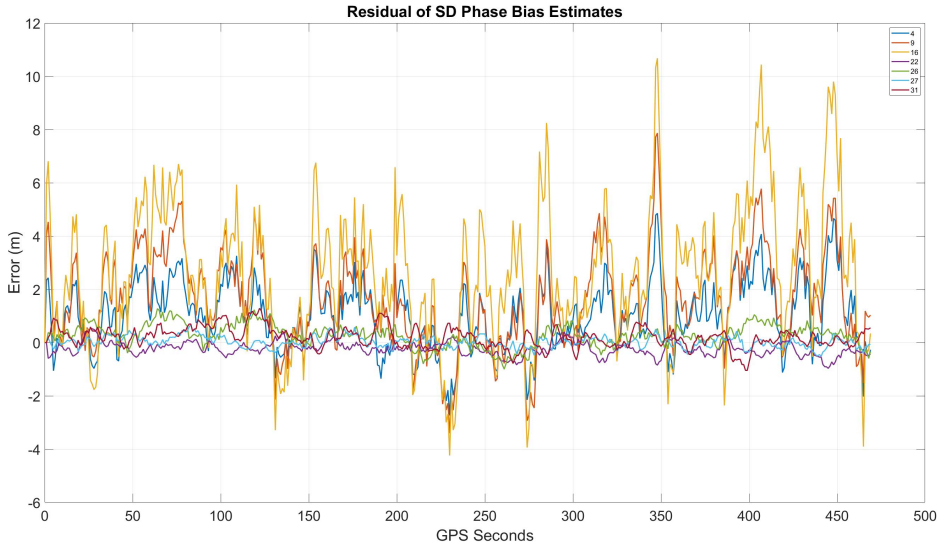

Figure 4.4: Static Baseline Test with Survey-Grade Antennas: GPS only Residuals (cycles)

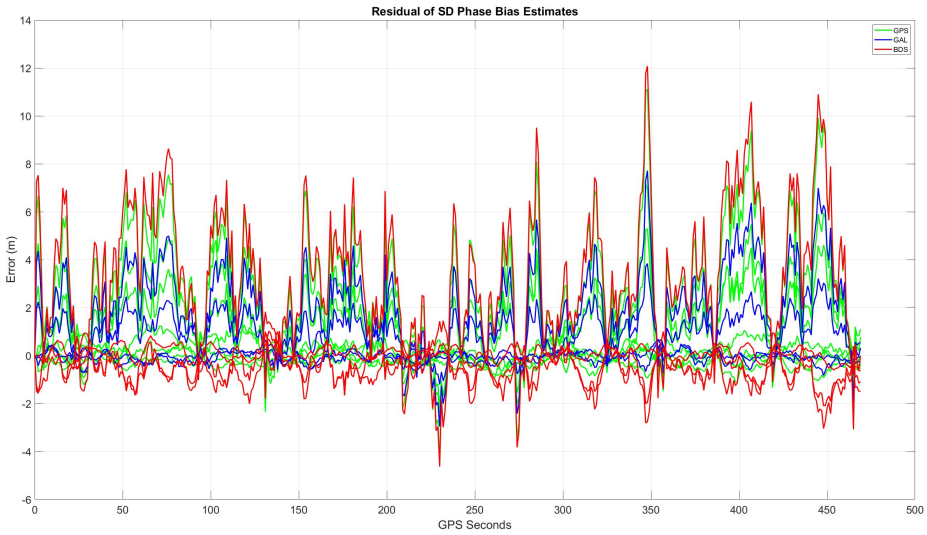

Figure 4.5: Static Baseline Test with Survey-Grade Antennas: Multi-GNSS Residuals (cycles)

Note that the additional constellations do not improve the magnitude of the residual error across all channels in the filter, and that spikes seen in the GPS only implementation can be observed across constellations. This suggests that the dynamics seen in these time series are attributed to a common error source such multi-path. This would explain the preference of residual error to a single slide of the error axis. However, the strength of multi-GNSS RTK comes from the additional DD estimates and covariances provided to the LAMBDA method. As stated in section 3.1.6, the LAMBDA method decorrelates the ambiguity estimates and respective covariances to reduce and more efficiently explore the search space for viable integer sets. The effects of correct information decorrelation can be seen below:

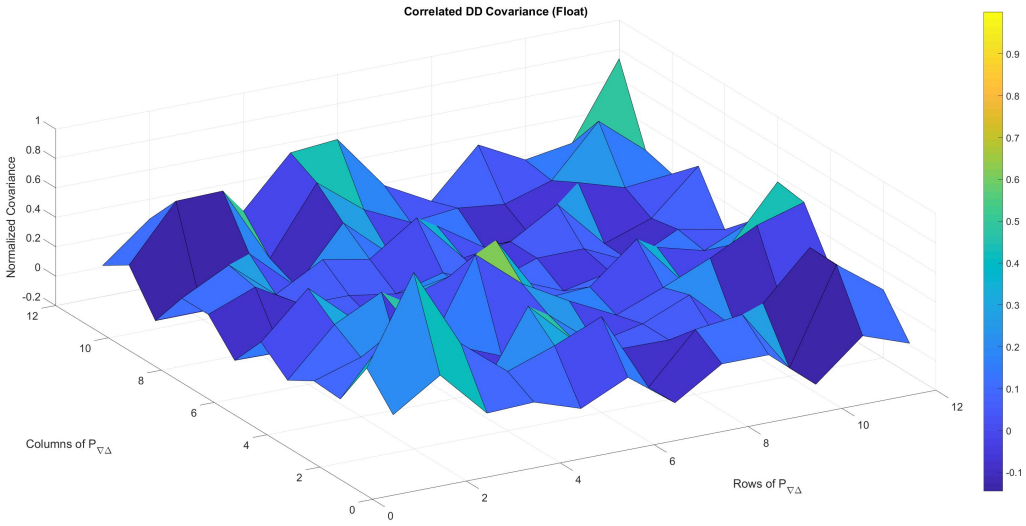

Figure 4.6: Correlated DD Covariance Values

Note the non-uniqueness of the covariance uncertainty for the DD ambiguity estimates. The disjointed characteristics can be attributed to how the Kalman couples information across measurements to better observe states of interest. The same covariance knowledge is shown below after correct decorrelation:

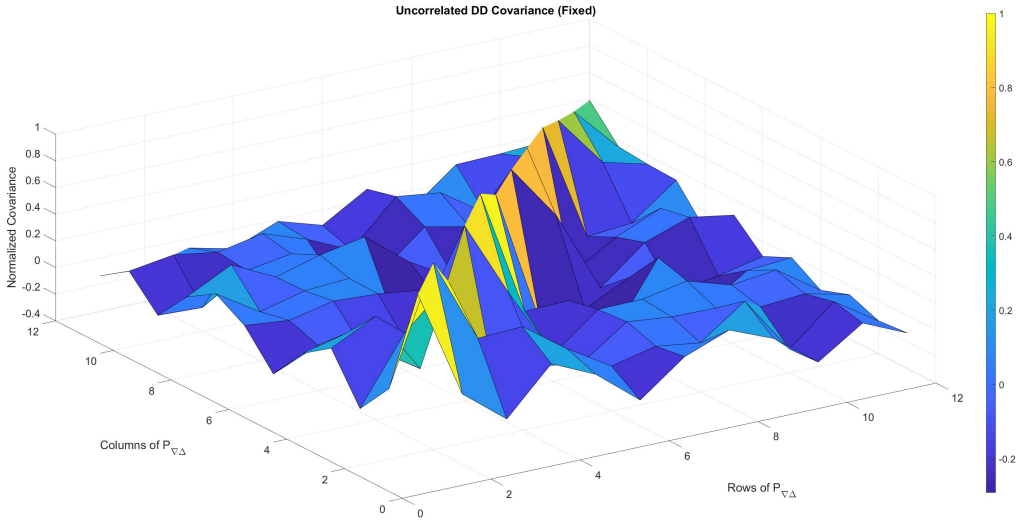

Figure 4.7: Decorrelated DD Covariance Values

Note that a majority of the information is stored along the diagonal, suggesting that state estimates are independent and have little-to-no impact on other states. This step is crucial due to

the strong correlation built during the recursive estimation and double differencing operations across states.

To investigate the proficiency of the LAMBDA method, the results of the ratio test are studied for both the GPS only and multi-GNSS architectures and can be seen in Figure 4.8.

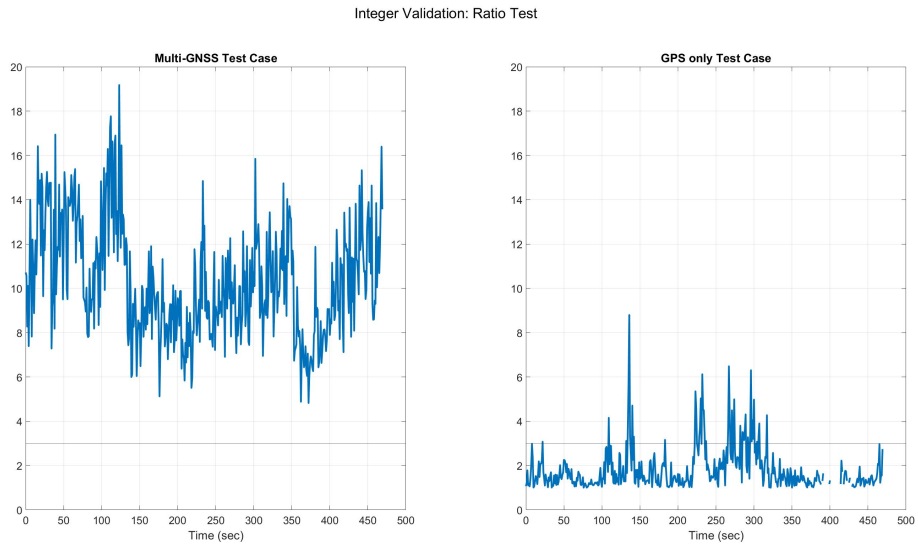

Figure 4.8: Static Baseline Test with Survey-Grade Antennas: Ratio Test Comparison

The difference in magnitude between the left and right plots demonstrates the improvement in the estimated integer confidence. The multi-GNSS filter is able to confidently estimate the correct integer set from the first epoch as seen by its high ratio value. The GPS only filter however, momentarily passes the threshold test momentarily near the 125s and 150s into the data set but doesn't pass the consecutive counter threshold until nearly 250s into the data set.

The estimated RPVs are shown one at a time below. First, the HP-RPV is shown once the consecutive threshold passes a valid integer set:

Figure 4.9: Static Baseline Test with Survey-Grade Antennas: GPS only Fixed RPV

The RPV is rotated to a local ENU frame centered about the base antenna to better interpret the RPV elements. One weakness that is well discussed in literature is the challenge of SF RTK/DRTK algorithms in kinematic platforms [1]. Here, the GPS only architecture is disadvantageous due to its long TTFF of about 250s. In scenarios where receiver LOS is depreciated, such as urban environments, a navigation filter must be able to converge to the correct set of integer estimates rapidly even in the presence of limited perceivable satellites. To conclude the study of SF GPS-only DRTK, the norm of each estimated RPVs is shown in Figure 4.10.

Figure 4.10: Static Baseline Test with Survey-Grade Antennas: GPS only Estimated RPV Norm

The HP-RPV provides the most stable navigation solution between antennas and is easily observed after the finding the norm of the estimated vectors. Note the noisiness of the PSR based solution. While this is the easiest solution to obtain, the accuracy of its results should be considered when using it in autonomous applications.

The HP-RPV solution for the multi-GNSS implementation is shown in 4.11.

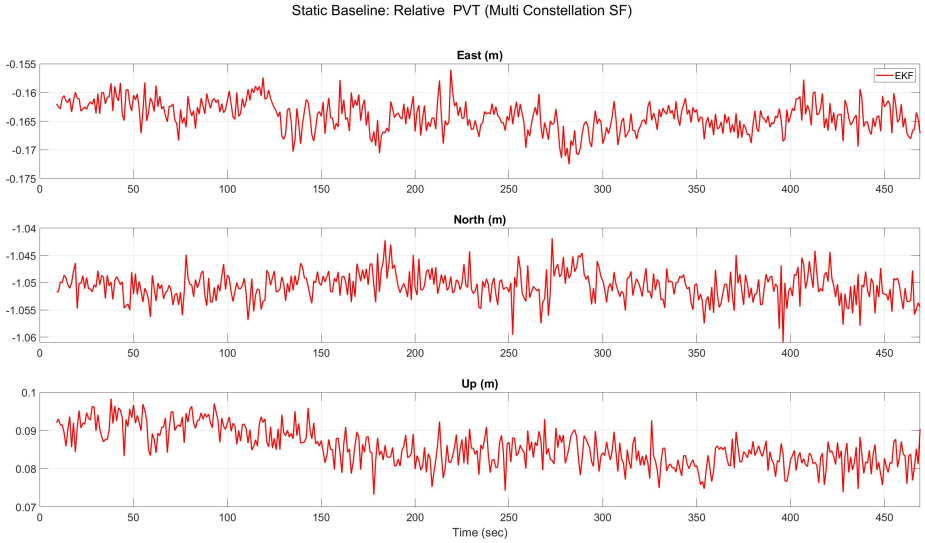

Figure 4.11: Static Baseline Test with Survey-Grade Antennas: Multi-GNSS Fixed RPV

The multi-GNSS implementation is able to find the correct integer set from the first epoch but the since the consecutive counter threshold must be passed, the HP-RPV solution is first provided 10s into the data set. Lastly, the norm of the estimated vectors are computed and can be seen below:

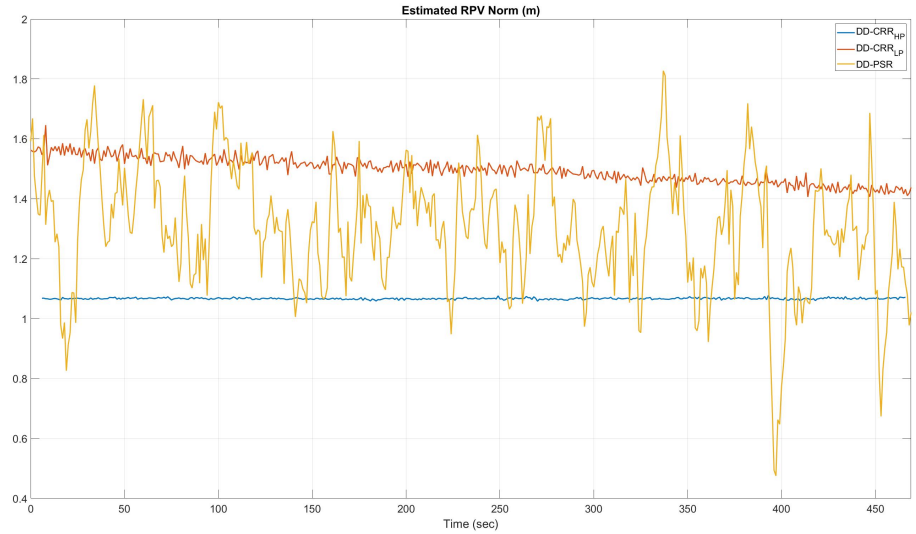

Figure 4.12: Static Baseline Test with Survey-Grade Antennas: Multi-GNSS Estimated RPV Norm

4.1.2.2 Dynamic Baseline

This test demonstrates how the algorithm is able to effectively estimate the ambiguity biases while the geometric relative range changes between platforms. For this work, the base was a Lincoln MKZ equipped with a Piksi Multi Evaluation Board and a Novatel Propak V3 for truth. The receivers were fed RF signal from a Trimble Survey-Grade Antenna. The rover vehicle was equipped with a Novatel ProPak OEM7 and a Novatel Propak V3 for truth. The receivers were provided RF signal by a Novatel Pinwheel Antenna. The experiment setup can be seen in Figure 4.13.

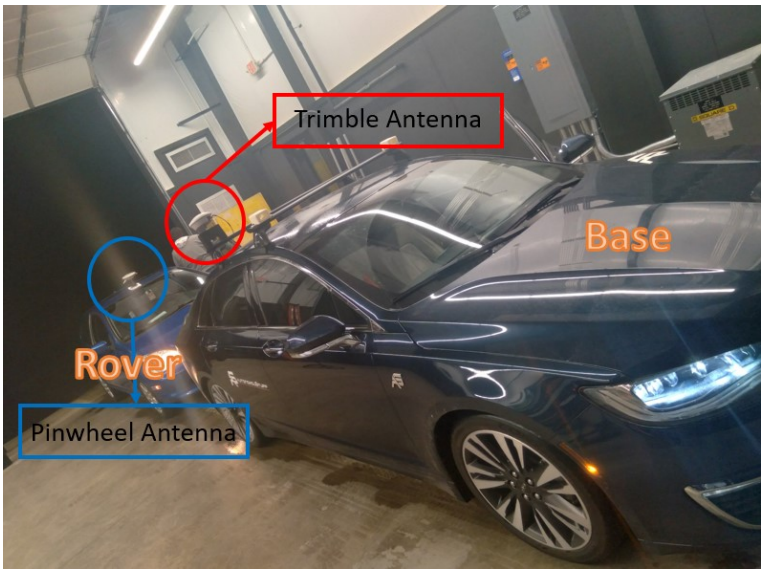

Figure 4.13: Dynamic Baseline Test with Survey-Grade Antennas: Experiment Setup

The test consisted of an initial static period, followed by a dynamic sequence from both vehicles driving circles around the NCAT skidpad in Auburn, Alabama.

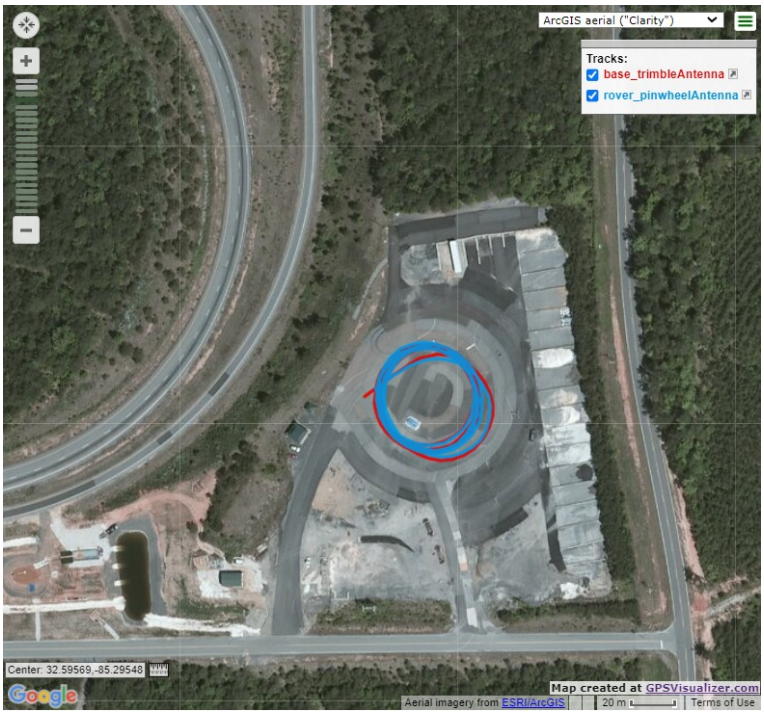

Figure 4.14: Dynamic Baseline RTK Trajectories

The vehicles were driven at a maximum of 10 MPH. There trajectories on the skidpad can also be visualized in Figure 4.14. The CNO ratios and ARI values can be plotted and used to assess the quality and observability of the GNSS observables.

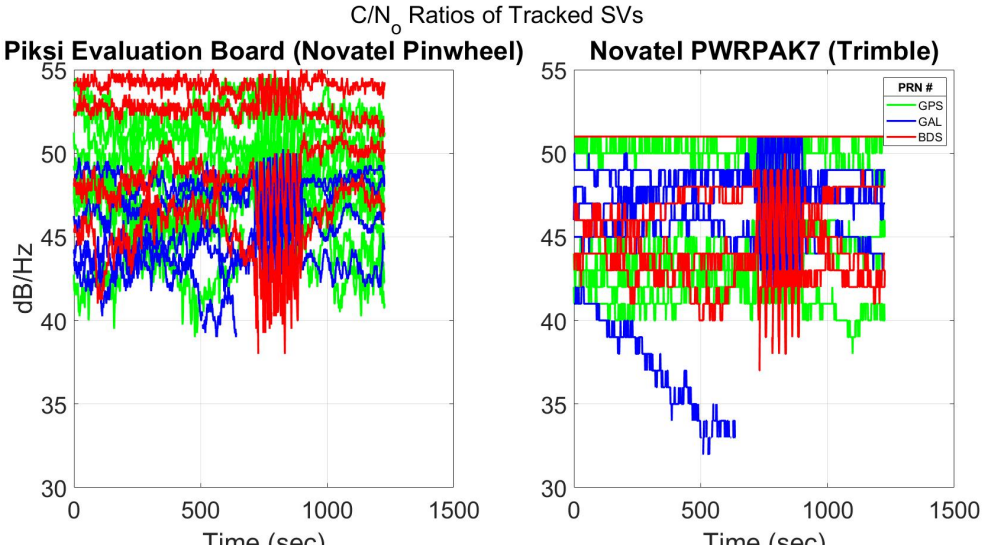

Figure 4.15: Dynamic Baseline Test with Survey-Grade Antennas: CNO Values

Similar behavior can be seen during the static portions of this test when assessing the diagnostic information. An obvious distinction can be made in the CNO values when both platforms begin moving near 700 seconds. It should be noted that the ARI values are more consistent for both static and dynamic periods of the test.

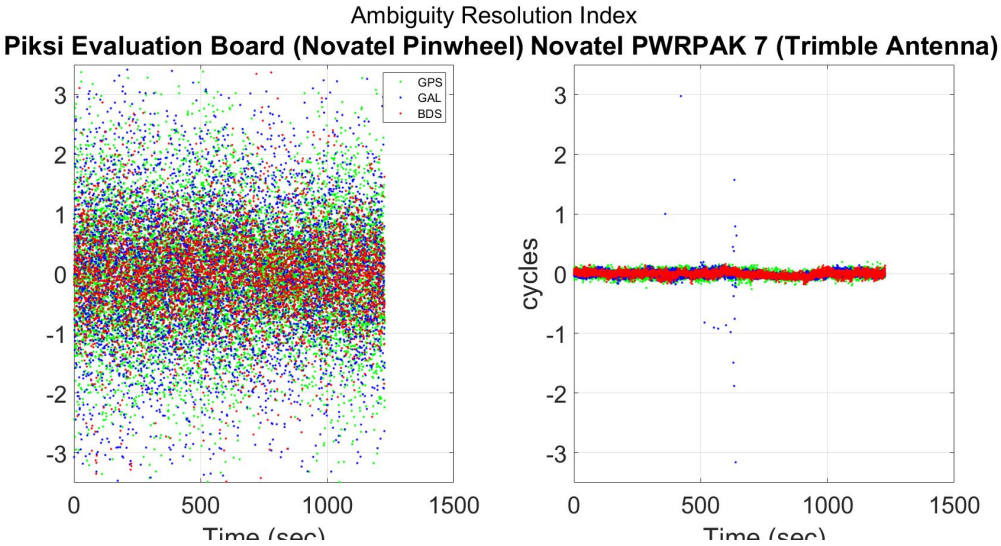

Figure 4.16: Dynamic Baseline Test with Survey-Grade Antennas: ARI Values

The residual error for the GPS only consideration is shown below for the complete data set. Similar magnitudes of residual error are seen during the static portions as seen in Figure 4.4

and Figure 4.5. However, a notable decrease in magnitude is seen during the dynamic portion of the run from 700 to 900 seconds.

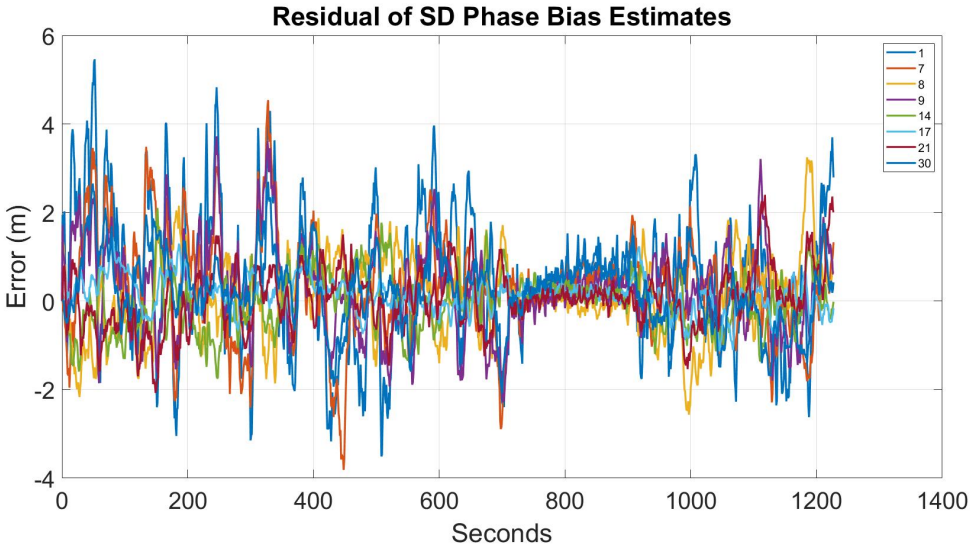

Figure 4.17: Dynamic Baseline Test with Survey-Grade Antennas: GPS only SD Residual Error

Again, the accuracy of the floating point ambiguity estimates are not improved with the addition of multiple constellations. This can be observed in 4.18 where channels belonging to the Galileo and BeiDou constellations share dynamics and similar levels of error.

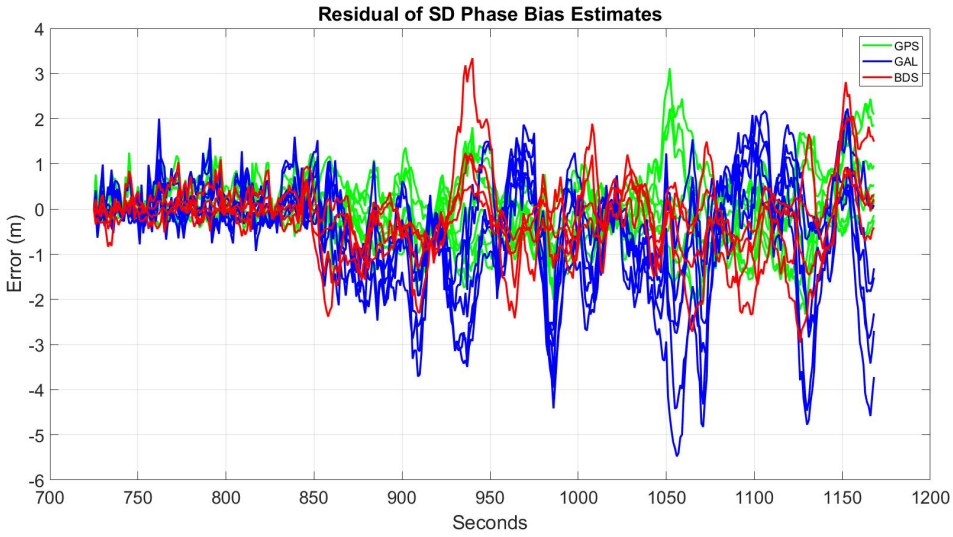

Figure 4.18: Dynamic Baseline Test with Survey-Grade Antennas: Multi-GNSS SD Residual Error

It should be noted that to ensure the affects of platforms dynamics were evaluated, the filter is initialized at the start of platform dynamics. Similar levels of integer validation metrics were observed between the static and dynamic baseline tests. The ratio test computed at every observation period is provided for both the GPS only and Multi-GNSS implementations.

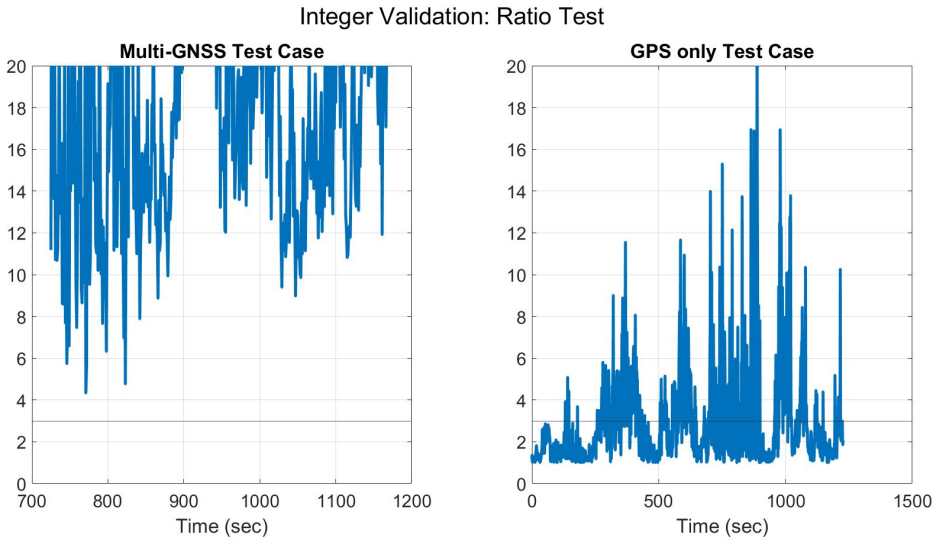

Figure 4.19: Dynamic Baseline Test with Survey-Grade Antennas: Ratio Tests

The ratio values are unaffected by the platform dynamics. Again, the values from the multi-GNSS and GPS only implementations have magnitudes consistent with the static baseline test and so high levels of estimated integer confidence is seen from the multi-GNSS architecture. The GPS only architecture initially experiences low confidence with its estimated integer sets but, eventually finds a valid integer set near 880 seconds. The ADOP, discussed in [8], are consistent with 100% confident integer sets for both architectures as seen in Figure 4.20. The empty space seen in the multi-GNSS ADOP values from 420 to 560 seconds was due to a BDS satellite dropout which caused the BDS relative clock bias to be unobservable. The time series for the complete data set is shown in

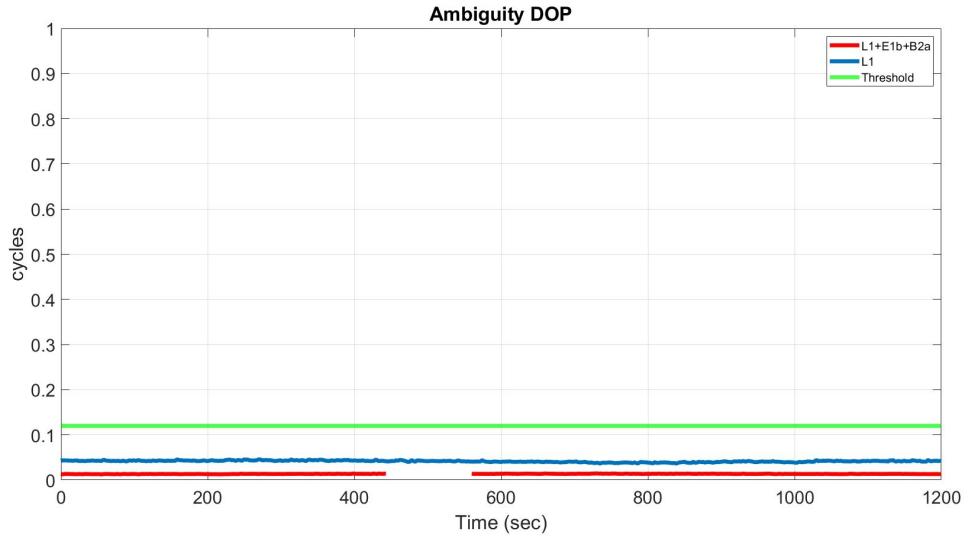

Figure 4.20: Dynamic Baseline Test with Survey-Grade Antennas: Ambiguity DOP

These validation metrics coupled with valid integer sets passing the consecutive threshold were found and used to compute the HP RPV estimate. To assess the accuracy of the DRTK solution, RTK positions of each platform were computed using a commercial software known as GraftNav and differenced to form the relative position truth.

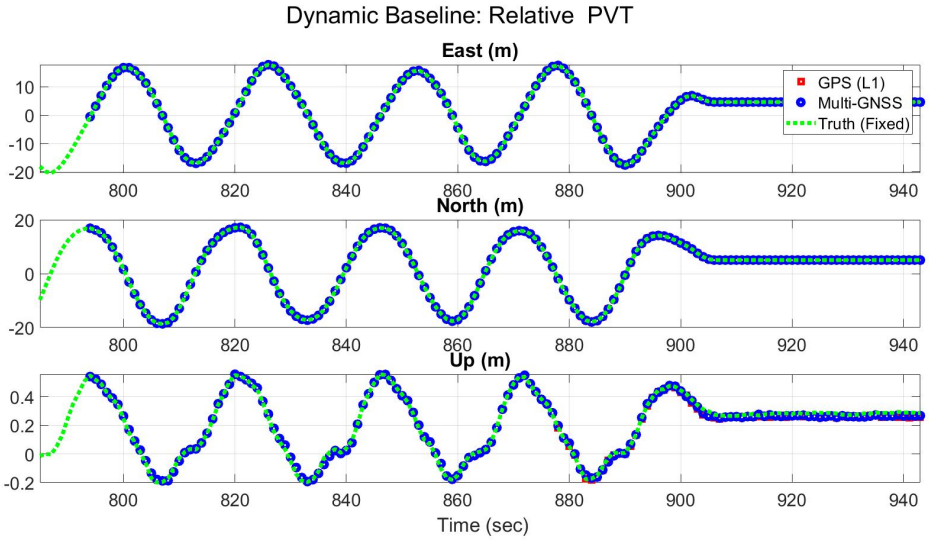

Figure 4.21: Dynamic Baseline Test with Survey-Grade Antennas: Estimated RPV comparison

The multi-GNSS architecture finds the correct integer set 10 seconds into the experiment. The GPS only architecture finds the correct integer set 74 seconds into the experiment. A 64 second improvement to the TTFF is observed by the new multi-GNSS architecture. Since both

architectures observe the relative range between phase centers, the HP-RPV of both are seen to track the truth accurately. To assess to accuracy of the DRTK HP-RPV solution, the DRTK RPV solution is differenced from the true RPV to compute RTK level metrics. These metrics can be seen for every acis in Figure 4.22.

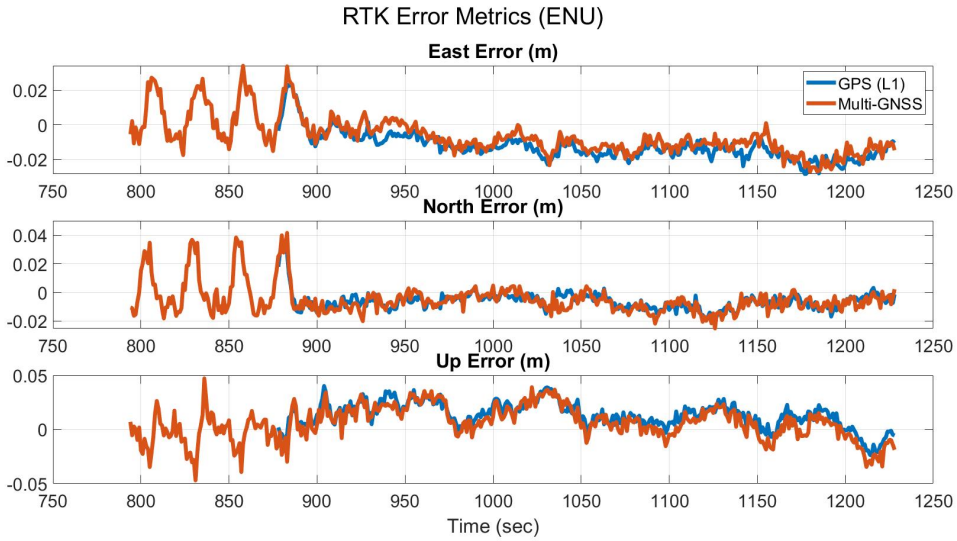

Figure 4.22: Dynamic Baseline Test with Survey-Grade Antennas: RTK Error Metrics

Centimeter level accuracy can be discerned by investigating the RTK metrics in Figure 4.22. There is a slight loss in accuracy during the dynamic portion of the data as seen by the orange time series. These are attributed to higher levels of phase center variations due to the platform dynamics.

4.2 Adaptive Extended Kalman Filter

In surveying applications, the antennas and receivers are of high quality. This allows accurate measurements to be made internally while mitigating the effects of errors such as multi-path through appropriate gain patterns. The use of a low-cost antenna pair with a survey-grade antenna can reduce performance aspects of the nominal algorithm described in the previous section. This impairment is due to biases present in specific channels which are poorly perceived by the antenna. These biases are unique to the single patch antenna and thus not removed through differential techniques. These biases, since not modeled, add obscurity to the ambiguities and prevent fast TTFF. One method for improving the TTFF for these scenarios

is to attempt to adaptively estimate the sensor and process noises acting on the system. These estimates improve the weighting applied to the measurements to more accurately depict their uncertainty due to hardware biases or multi-path.

For the adaptive DRTK algorithm, all steps are identical the the previously discussed DRTK algorithm with the exception of the float point ambiguity resolution step discussed in section 3.1.3. Here, an adaptive filter is used which identifies values of R_k or Q_k.

4.2.1 Process Noise

Process noise describes the uncertainty in the modeled state dynamics. For this approach, the noise is assumed to be Gaussian with characteristics such that $w_k \sim \eta(0,Q_k)$. The implementation used here was derived in [17]. It uses a Method of Maximum Likelihood (MMLE) within the framework of a Kalman Filter. The MMLE uses the residual between the a priori and a posteriori state estimates to update the estimate of Q_k. The update equation is shown below:

$$Q* = \Delta x_k \Delta x_k^T + P_k^- - P_k^+ - \hat{Q}_k^- \tag{4.8}$$

where

$$\Delta x_k = \hat{x}_k^+ - \hat{x}_k^- \tag{4.9}$$

and $Q*$ is the process noise covariance update, Δx_k is the state estimate residual, $\hat{x}_k^+$ is the a posteriori state estimate, $\hat{x}_k^-$ is the priori state estimate, P_k^+ is the a posteriori covariance estimate, P_k^- is the a priori state covariance estimate, and $\hat{Q}_k^-$ is the current expected process noise covariance. The term Δx_k is the measured state residual, and represents the difference between the state estimate before and after the measurement update. If this residual is large, this is an indication that the filter is not predicting the future state very well. This is because there is a large jump in the expected state when the measurements are applied. As the filter converges, this residual should decrease as its ability to predict the next state is expected to improve.

The second half of the equation $P_k^- - P_k^+ - \hat{Q}_k^-$ is a measure of the predicted state residual, and represents the expected change in the state covariance. The process noise update, Q*, is then combined with the current value of $\hat{Q}_k$ in a running-average filter:

$$\hat{Q}_k^+ = \hat{Q}_k^- + \frac{1}{L_Q}(Q * - \hat{Q}_k^-) \tag{4.10}$$

In the equation 4.33, L_Q is the window size.

4.2.2 Measurement Noise

Measurement noise describes the accuracy of the observables used in the measurement update. This noise is typically described as $v_k \sim \eta(0, R_k)$. In the geometric model, the non-deterministic term in the equation is assumed to be uncorrelated Gaussian white noise. However it should be noted that there are some assumptions made from the original measurement model shown in Equation 3.1 and the considered SD measurement model seen in Equation 3.1. These assumptions suggest that the hardware biases and multipath effects are considered negligible and assumed to be lumped in the noise term [63]. This assumption holds in most cases, but there exists scenarios where equipment, platform dynamics, or environment can make this less accurate [64,52,41].

The sensor noise present is observed by the residual between the expected and actual measurements. The sensor noise update equation is shown below:

$$R* = \Delta y_k \Delta y_k^T - H_k P_k^+ H_k^T \tag{4.11}$$

Where

$$\Delta y_k = y_k - \hat{y}_k^+ \tag{4.12}$$

and where H_k and y_k are the observation matrix and measurements at time k. This routine is run after the measurement update, thus, $\hat{y}_k^+$ is defined as:

$$\hat{y}_k^+ = H\hat{x}_k^+ \tag{4.13}$$

The second term $H_k P_k^+ H_k^T$ cancels expected measurement error due to the state uncertainty. Similar to the process noise estimation, the update is applied to the $\hat{R}_k^k$ through a similar low-pass filter:

$$\hat{R}_k^+ = \hat{R}_k^- + \frac{1}{L_R}(R * -\hat{R}_k^-) \tag{4.14}$$

The capabilities of this algorithm has been shown in simulations where both platforms are dynamic and signal quality is poor due to the environment of interest [52]. This works aims to experimentally validate the capabilities of this algorithm when signal quality is poor due to antenna grade and platform dynamics.

4.2.3 Experimental Results

4.2.3.1 Static Baseline

For ambiguity estimation, uncertainty in the time update can be held constant since the integer ambiguity remains constant. This allows us to estimate measurement uncertainty without relying on receiver provided values which can be over optimistic in many situations. To demonstrate the improvement to the AR a static baseline experiment was conducted using a Novatel PWRPAK7 receiver with Trimble Antenna for the base unit. The rover unit consisted of the Piksi Evaluation Board and a Ublox Patch Antenna. The Ublox patch antenna is a single frequency antenna and has poor gain patterns low on the horizon. This is demonstrated and discussed in [43].

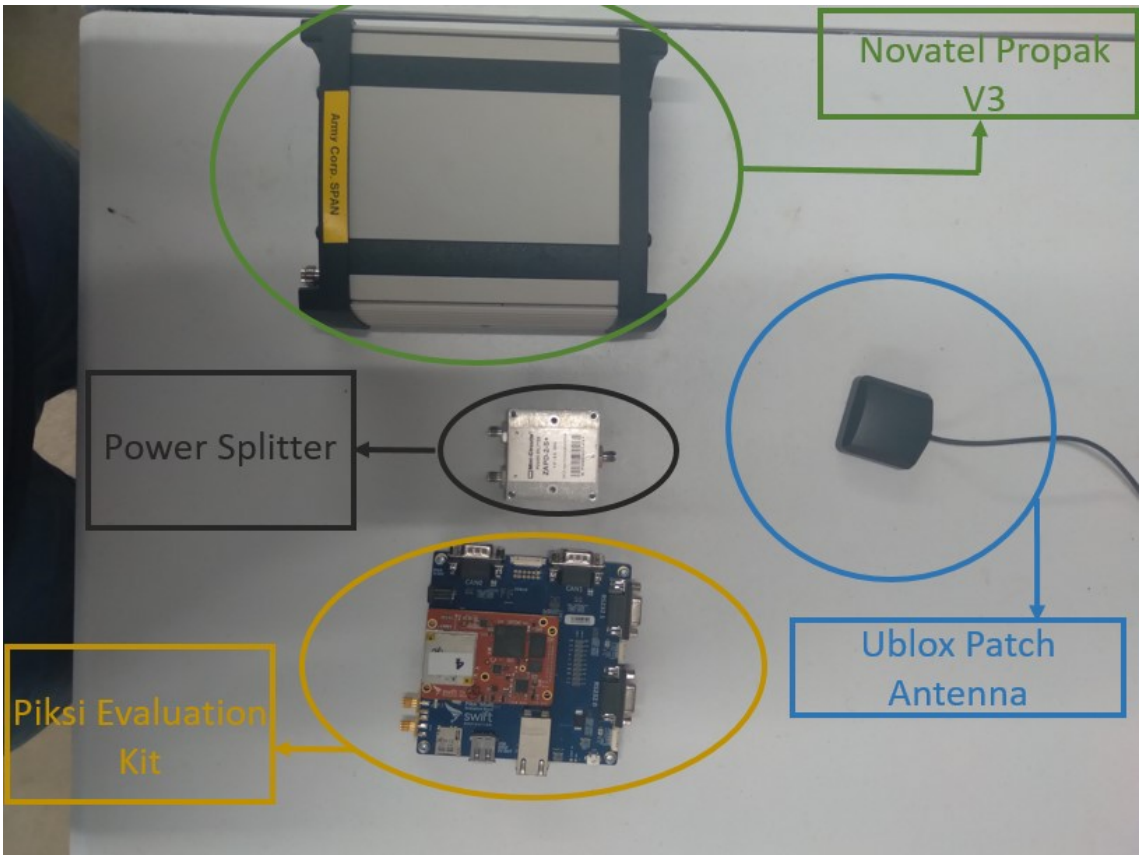

Figure 4.23: Static Baseline Test with Low-Cost Antennas: Experiment Setup

The same equipment was used for the base so similar diagnostic measures were observed as seen in the multi-GNSS sections. However, the Novatel Pinwheel used by the Piksi Evaluation board was switch with a low-cost Ublox patch antenna. The rover's sensor suite is seen in Figure 4.23.

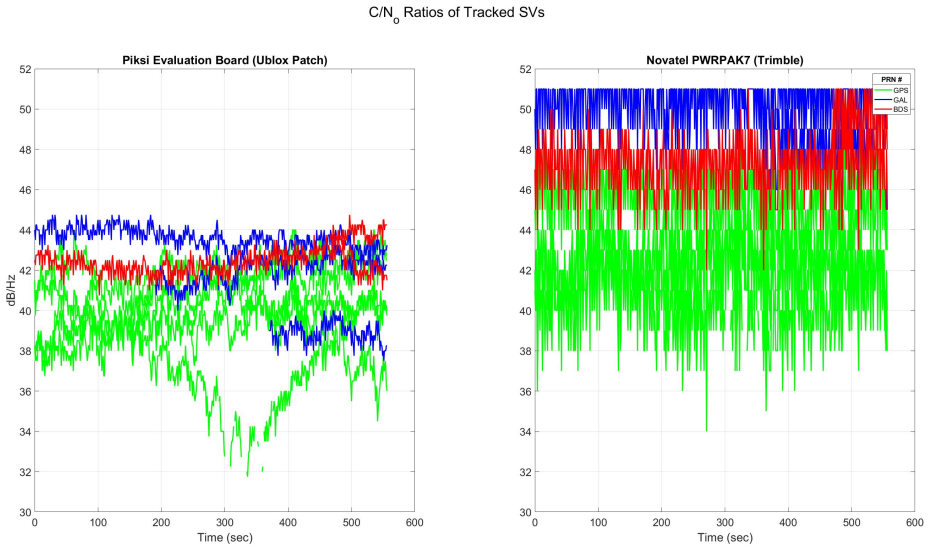

(a)

Figure 4.24: Static Baseline Test with Low-Cost Antennas: CNO Ratios

Figure 4.24 compares the CNO ratios between the base and rover. A notable difference can be seen in CNO magnitude can be seen due to the patch antenna. This degradation in signal quality can also be observed by an increase in ambiguity obscurity as shown by the ARI values in Figure 4.25.

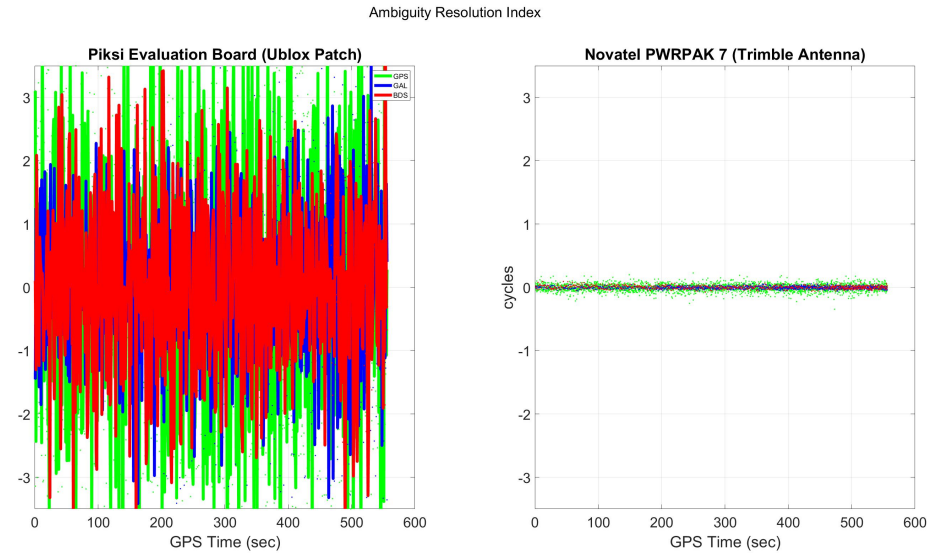

(a)

Figure 4.25: Static Baseline Test with Low-Cost Antennas: ARI Values

An obvious increase in ARI magnitude can be seen across all channels. This suggests increased obscurity when attempting to estimate the ambiguities. Furthermore, an additional layer of degradation is seen to occur when using the patch antenna. This is due to less than 4 SVs being visible for the Galileo and BeiDou constellations. In addition, the observed GPS satellites are limited and are seen to periodically dropout mid-run. All satellites seen by the Piksi during this ten minute data run can be seen below:

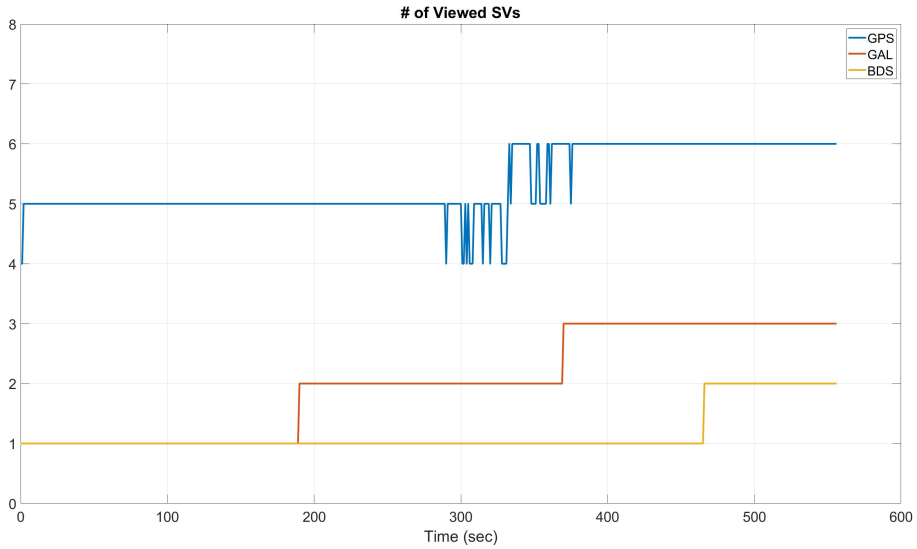

Figure 4.26: Satellites Viewed with Low-Cost Antenna

Multi-GNSS based approaches are not applicable in this experiment since less than four satellites are in view for the Galileo and BeiDou constellations. Instead, a single frequency GPS only implementation must be utilized. As demonstrated in section 3.3, this approach has poor performance characteristics. For this work, up to 6 GPS satellites are seen for the total data set. PRN 8 and 16 are low on the horizon and exhibit poor SD residual error. Using the nominal algorithm, fixed integer precision is not achievable due to the geometry and limited observables. While the time series of the SD residual error is similar for both the nominal and adaptive algorithms, the state uncertainty for the SD ambiguity estimates differ. First, we consider the estimated measurement noise trajectories for the used channels. This weighting matrix is initialized with the receiver's reported measurement uncertainty. This is done to accurately assess the uncertainty of the used observables after extracting positional and clock bias information from the carrierphase. Below are the time series for the estimated uncertainties:

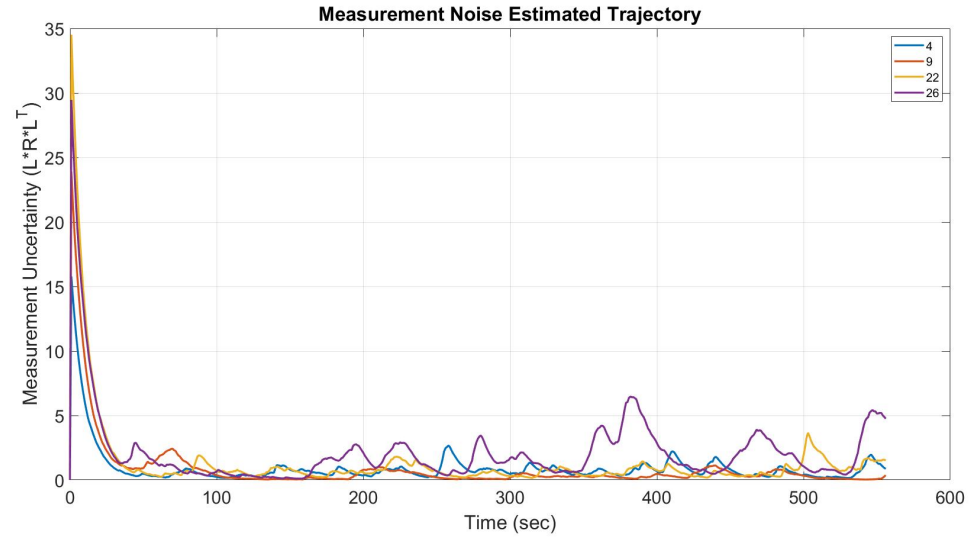

Figure 4.27: Static Baseline test with Low-Cost Antenna: Estimated Measurement Trajectories

For this study, the process noise was kept constant at 100e-06. The state covariance, a recursive value tracking state uncertainty, can be affected by both the measurement and process noise. The state covariances of the estimated SD ambiguities are shown in Figure 4.28 and seen not to converge to a steady state value.

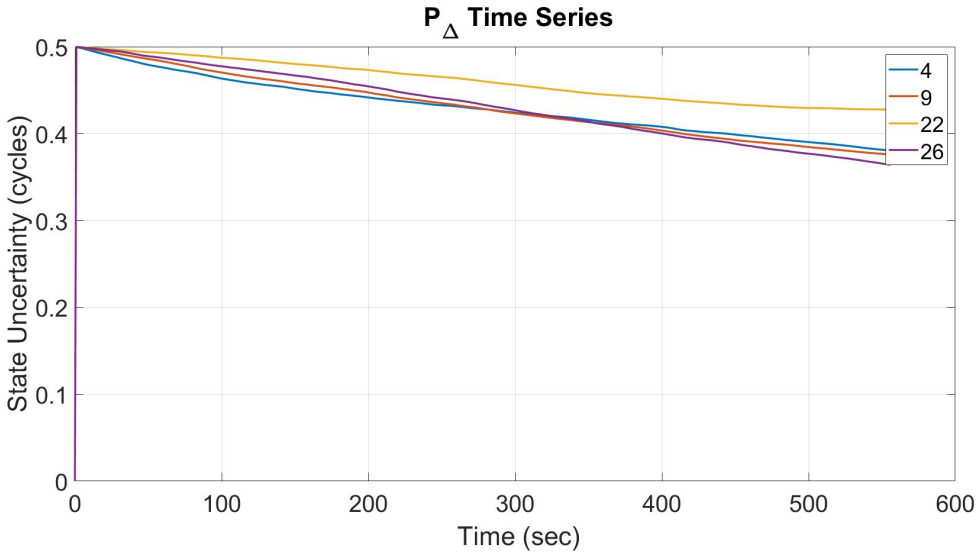

Figure 4.28: Static Baseline test with Low-Cost Antenna: Nominal SD Ambiguity Covariance

Due to the very low process noise, a slow convergence to steady state covariance values is seen in Figure 4.29. The over-optimistic measurement noise creates a hesitancy in the filter to

correct it states estimates. The resulting state covariances from the adaptive EKF is shown in 4.29.

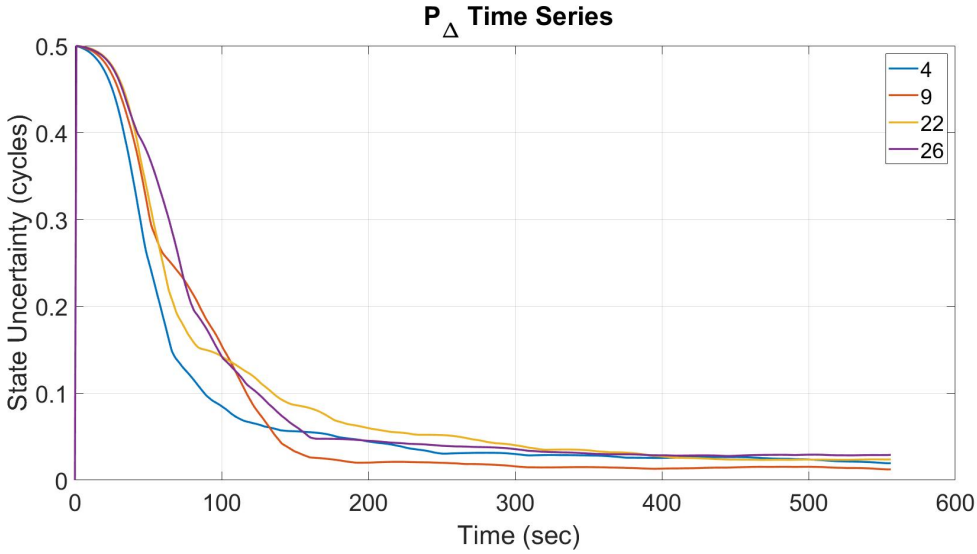

Figure 4.29: Static Baseline test with Low-Cost Antenna: Adaptive SD Ambiguity Covariance

Steady-state dynamics suggest a local or absolute extrema has been found by the filter indicating improved ambiguity resolution and the potential of finding a valid integer set. The resulting ratio values from the adaptive EKF and LAMBDA method is shown in Figure 4.30.

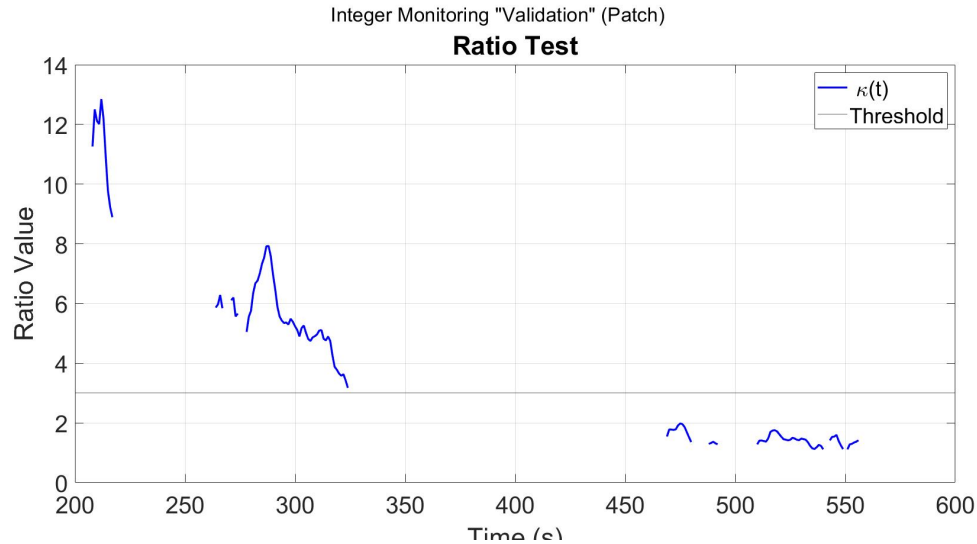

Figure 4.30: Static Baseline test with Low-Cost Antenna: Adaptive Ratio Test

The LAMBDA method has trouble finding valid integer sets throughout the data set as seen during 225 to 260 seconds and 335 to 475 seconds. These periods of invalidity cause the

empty spaces of ratio values seen in 4.30. With a consecutive threshold of 10, the first valid set of integer values were found near 200s. The resulting HP-RPVs are shown below:

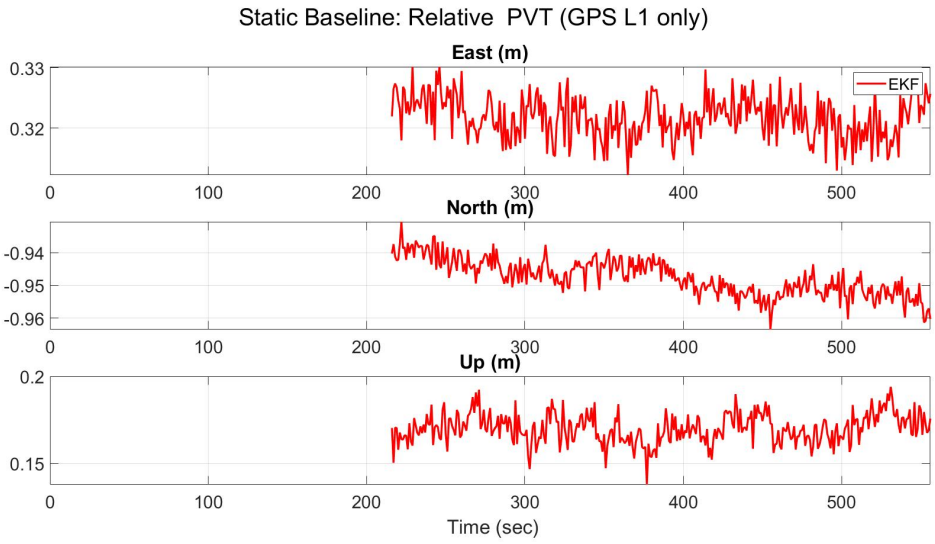

Figure 4.31: Static Baseline test with Low-Cost Antenna: Fixed RPV

Centimeter level precision is observed in the estimated HP-RPV. To compare the stability of the HP-RPV to the other solutions availble in the DRTK algorithm the magintude of each of the RPVs are plotted in Figure 4.32.

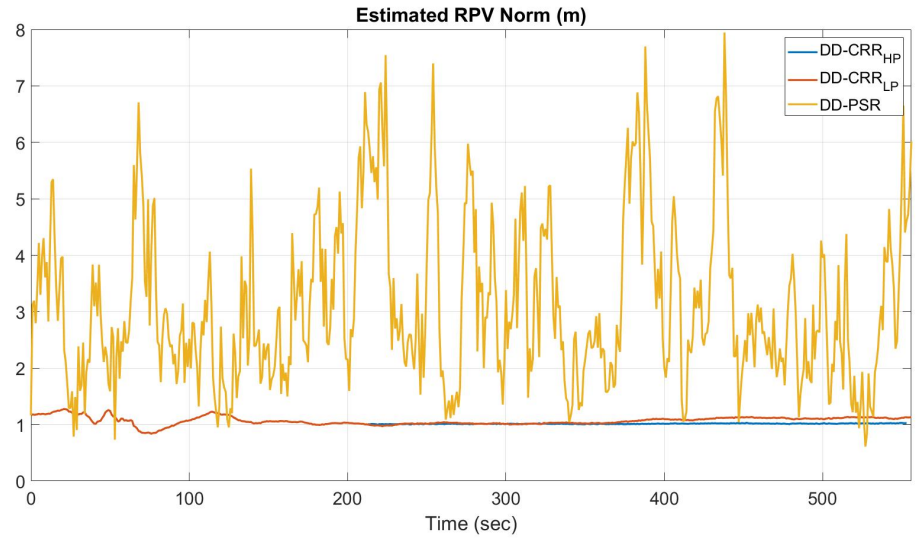

Figure 4.32: Static Baseline test with Low-Cost Antenna: Estimated RPV Norm

High levels of noise are seen in the DD-PSR solution making it undesirable for navigation. The LP-RPV is more stable but experiences some dynamics due to error in the float ambiguity estimates. Lastly, we see the expected long term stability of the HP-RPV.

4.2.3.2 Dynamic Baseline

The dynamic baseline experiment aims to experimentally validate the adaptive EKF formulation as a viable method for precise relative positioning. Again, the base used a Novatel PowerPAK7 and a Novatel Propak V3 for truth. The receivers were fed RF signal from a Trimble Survey-Grade antenna. The rover vehicle was equipped with a Piksi Evaluation Board and a Novatel Propak V3 for truth. The receivers were provided RF signal by a Ublox patch antenna.

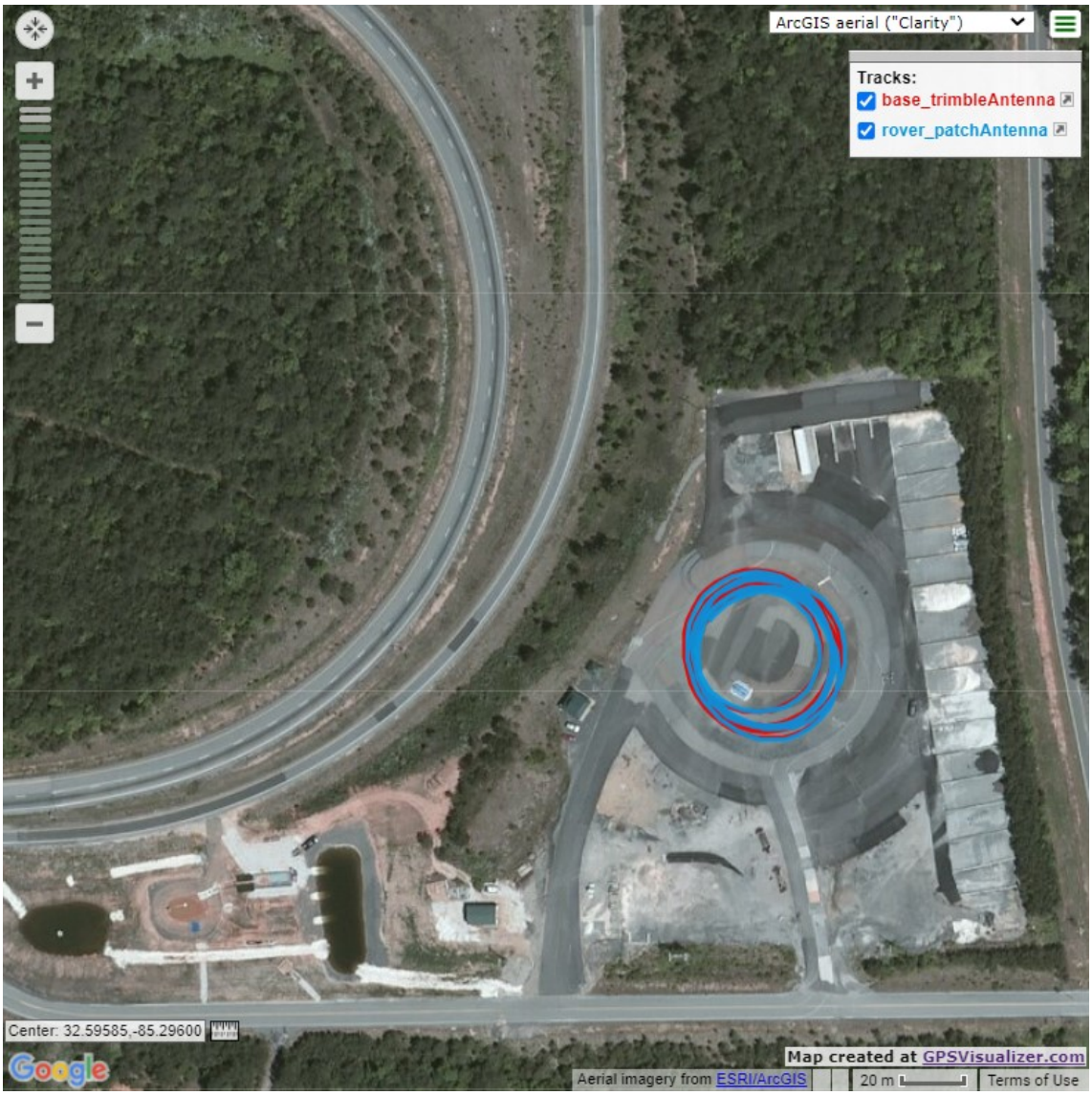

Figure 4.33: Dynamic Baseline Test with Low-Cost Antennas: CNO Values

Similarly, the test consisted of an initial static period, followed by a dynamic sequence from both vehicles driving circles around the NCAT skidpad.

The vehicles were driven at a maximum of 10 MPH. Again the CNO ratios and ARI values can be plotted and used to assess the quality and observability of the GNSS observables.

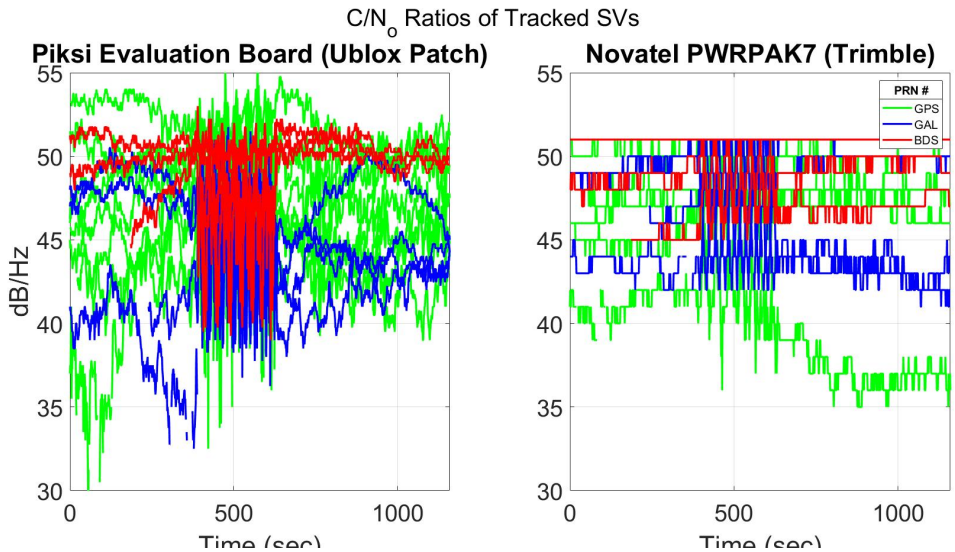

Figure 4.34: Dynamic Baseline Test with Low-Cost Antennas: CNO Values

Similar behavior can be seen during the static portions of this test when assessing the diagnostic information. An obvious distinction can be made in the CNO values when both platforms begin moving as seen in Figure 4.34. Again, we see higher levels of ambiguity obscurity as observed by the ARI values in Figure 4.35.

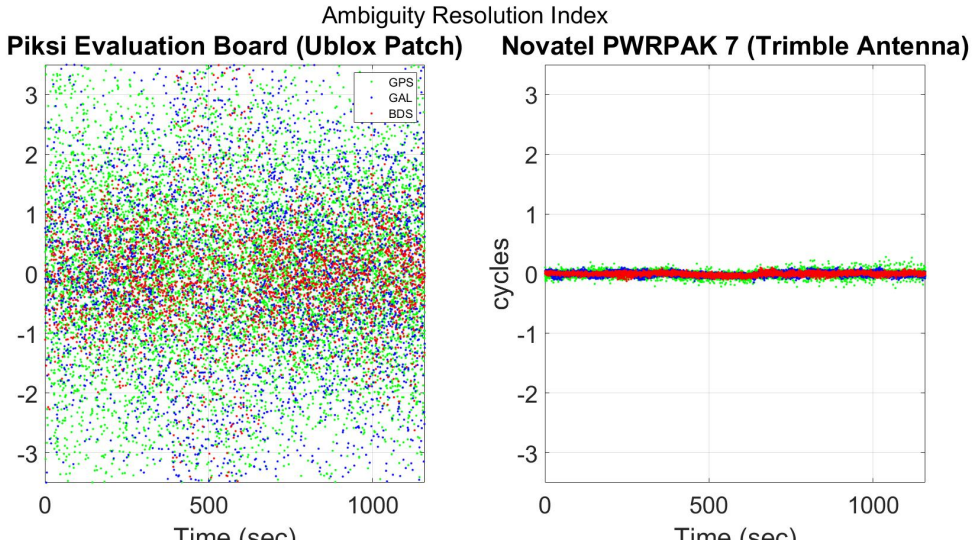

Figure 4.35: Dynamic Baseline Test with Low-Cost Antennas: ARI Values

Lastly, we can observe the common fifteen channels tracked by both receivers. These are visualized by constellation in Figure 4.36.

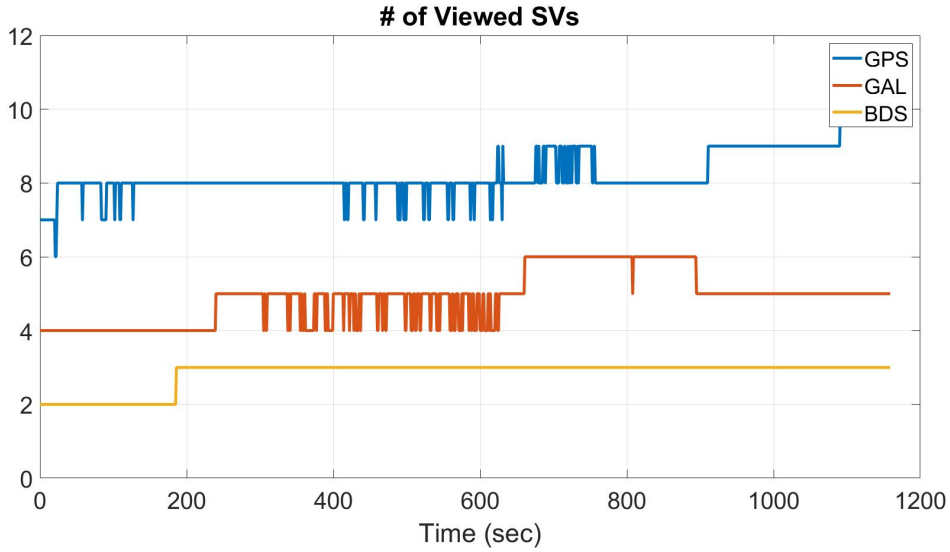

Figure 4.36: Dynamic Baseline Test with Low-Cost Antennas: Viewed Satellites

The patch antenna has trouble perceiving BDS satellites but sufficient Galileo satellites are in view to be integrated into the filter. However, due to the quality of measurements, Galileo was not included in the study. It should be noted that at times upwards of nine GPS SVs are viewed by the antenna. This allows for higher chances of correct ambiguity fixing. To better demonstrate the affects of total SVs used in the filter on ambiguity resolution the ADOP value is plotted in Figure 4.37 while varying this number.

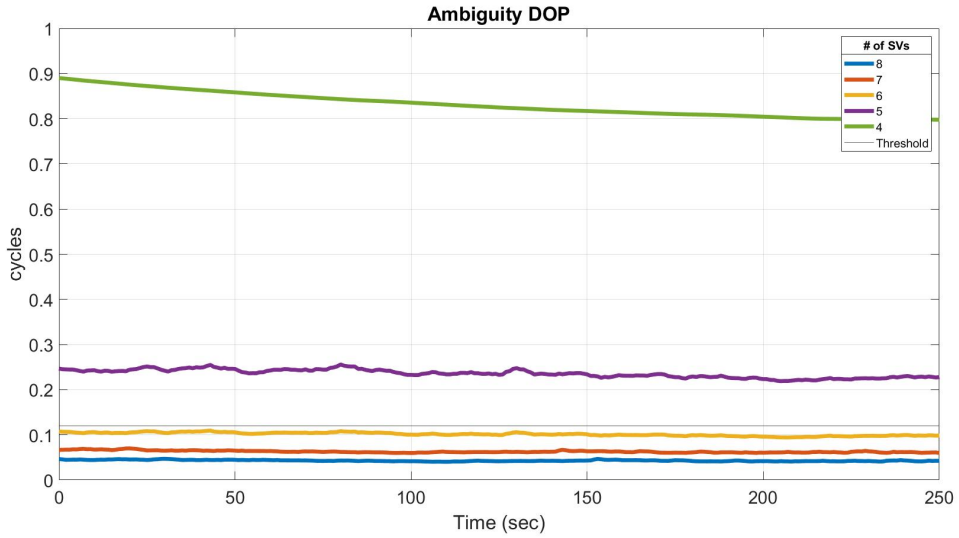

Figure 4.37: Dynamic Baseline Test with Low-Cost Antennas: ADOP Values

Note that after less than six satellites are used in the filter the chance for correctly fixing integers is very low. While the ADOP values were used as an additional validation metric during analysis, they were not integrated as a form of validating a candidate integer set.

The residual error for the GPS-only architecture is shown in Figure 4.38 for the complete data set. Similar magnitudes of residual error are seen during the static portions as seen in 4.4 and 4.5. The high levels of error observed during the static portions are attributed to multi-path cause by foliage near the starting and ending locations of the vehicles. This is verified by the more consistent residual error experienced during the dynamic portion of the data set.

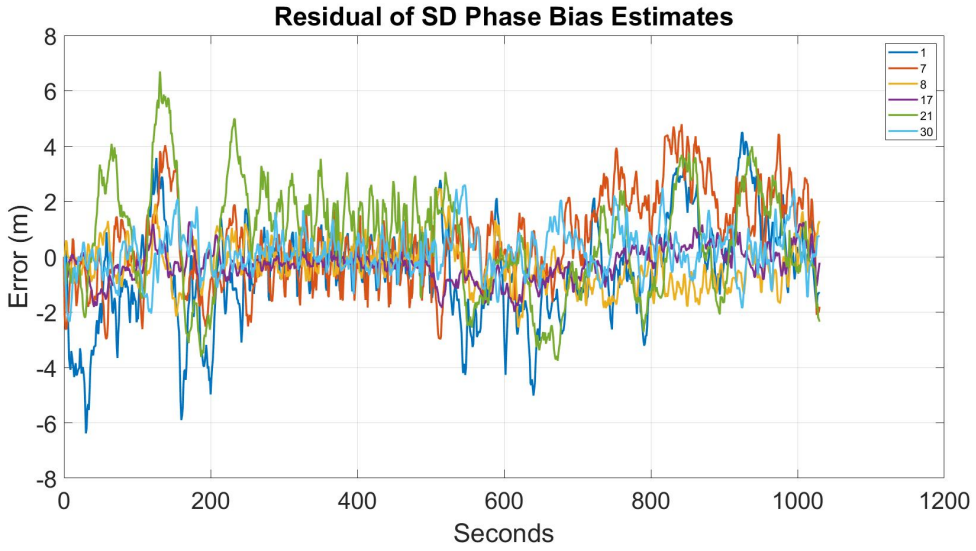

Figure 4.38: Dynamic Baseline Test with Low-Cost Antennas: GPS-only SD Residual Error

Again, the adaptive EKF is initialized during the dynamic portion to evaluate the effects of changing geometric range while attempting to estimate measurement uncertainty. Similar error dynamics can be seen across Figures 4.37 and 4.39 suggesting no significant improvement to floating point ambiguity resolution can be expected when using the adaptive EKF. The benefits of the adaptive EKF however can be seen as the integer validation section of the algorithm is assessed.

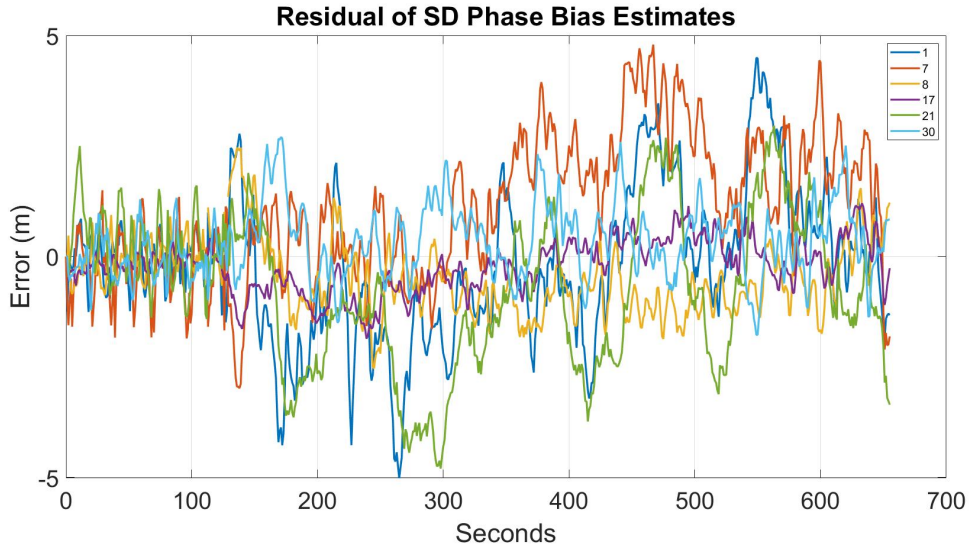

Figure 4.39: Dynamic Baseline Test with Survey-Grade Antennas: Adaptive SD Residual Error

Similar levels of integer validation metrics were observed but the adaptive filter is able to consistently achieve ratio values above the desired threshold. From Equation 3.32, the best candidate integer set is in the denominator of the fraction. Thus, as the float ambiguity set converges to the true ambiguity values, the difference between the float and optimal sets is small thus increasing the ratio value. This suggests that the float DD ambiguity estimates are able to be fixed more accurately through the adaptive EKF. The ratio test computed at every observation period is provided for both the GPS only and adaptive implementations in Figure 4.40.

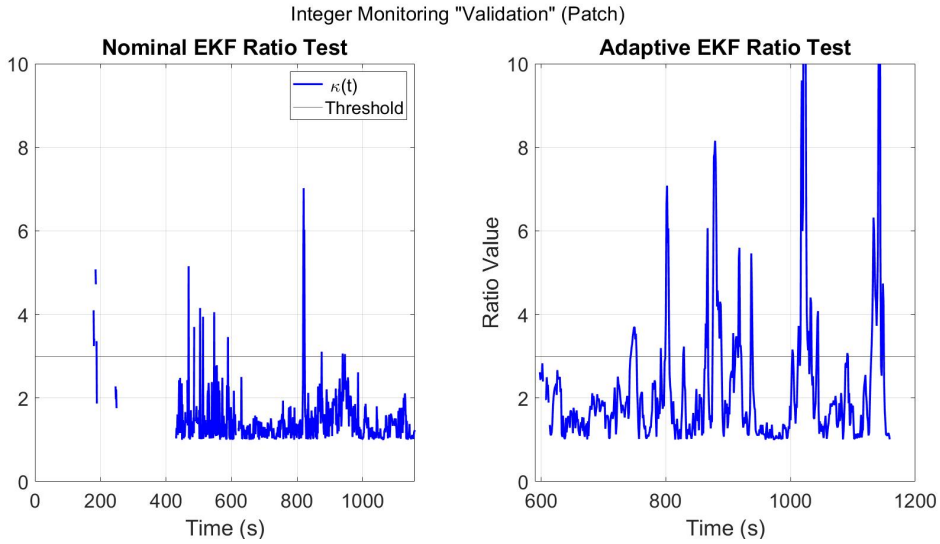

Figure 4.40: Dynamic Baseline Test with Survey-Grade Antennas: Multi-GNSS SD Residual Error

The ratio values are unaffected by the platform dynamics. Again, the values from the adaptive and nominal implementations have magnitudes consistent with the static baseline test. The ratio test resulting from the adaptive EKF however, is able to sustain high level of confidence in its candidate integer sets allowing it to pass the consecutive ambiguity counter threshold. The ADOP can also be used here to demonstrate the improvement to the AR of the problem.

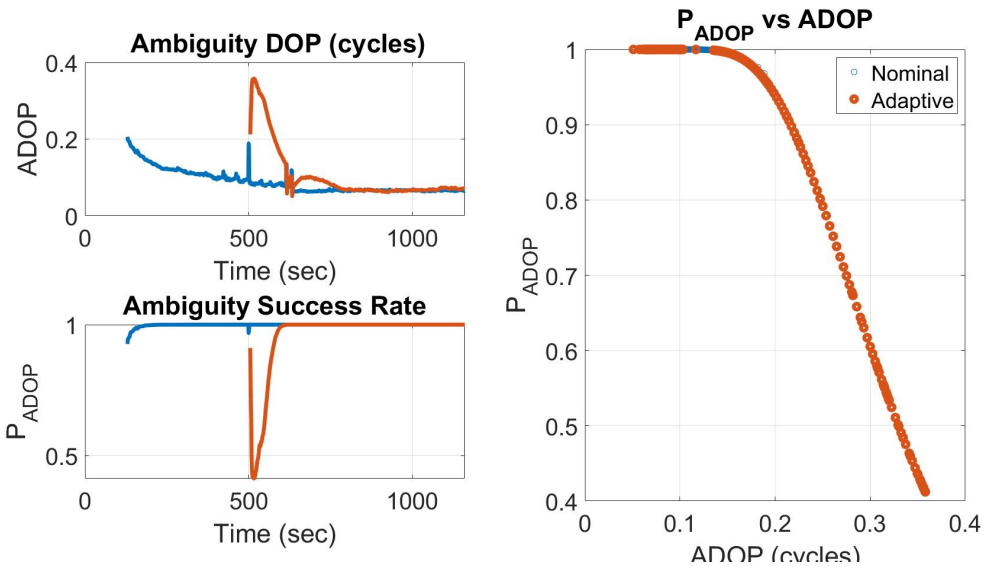

Figure 4.41: Dynamic Baseline Test with Survey-Grade Antennas: Ambiguity DOP

Both the nominal and adaptive EKF formulations obtain to 100% integer fixing rate due to the number of Svs used in the filter. However, the resulting candidate sets from the nominal

EKF formulation can be seen to cause instability in the estimated HP-RPV proving that they are incorrect. These validation metrics, coupled with valid integer sets passing the consecutive threshold, were found and used to compute the HP RPV. To assess the accuracy of the DRTK solution, RTK positions of each platform were computed and differenced across platforms to form the relative position truth. This was compared against the nominal and adaptive implementations.

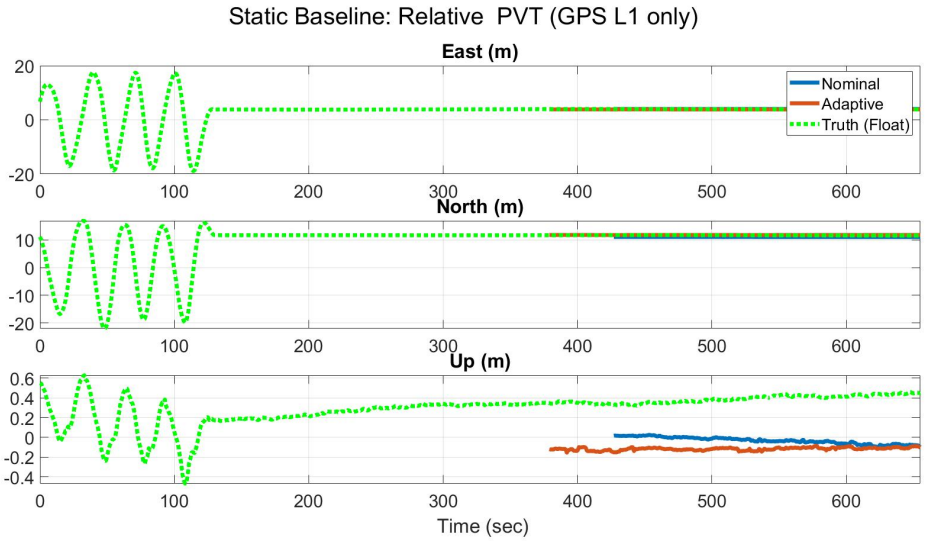

Figure 4.42: Dynamic Baseline Test with Survey-Grade Antennas: Relative Positions

An item of interest is the quality of the truth solution provided by GraftNAV. When using the patch antenna the software is only able to provide a float level solution, which as stated earlier, can be biased and drift from the true solution. This can be easily observed in the Up direction in 4.42 as truth is seen to drift several centimeters after the vehicles have stopped moving. This level solution depreciates the value of comparing the truth to DRTK solution since we lose the certainty of centimeter level accuracy. The solutions of both architectures are still compared to truth as reference for solution precision. Both the nominal and adaptive EKF formulations can achieve the HP-RPV estimates but only after the vehicles have stopped moving. While both can provide the HP-RPV, the difference in quality of the solution can be observed by comparing the Up-direction between formulations. The solution provided by the nominal EKF formulation is seen to drift by close to 10 centimeters in the Up direction. Centimeter level precision is expected from the HP-RPV estimate suggesting that the chosen candidate set was

incorrect. The adaptive formulation is observed to be more stable than its nominal counterpart as its Up-direction does not drift. Again, due to the float solution provided by GraftNAV, the accuracy between both formulations cannot reliably be assessed but for completion the RTK metrics are shown in Figure 4.43.

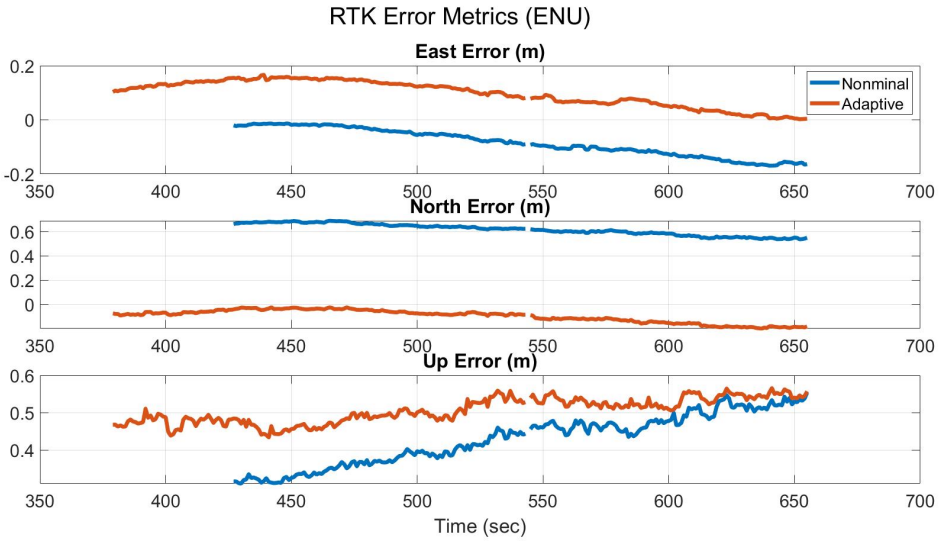

Figure 4.43: Dynamic Baseline Test with Survey-Grade Antennas: Position Errors

The effects of the drift can be observed in all directions by both formulations. A noticeable bias can be seen in the North error of the nominal solution where the adaptive solution is seen to more closely follow the truth.

4.3 Tightly-Coupled DGPS/UWB Filter

For specific applications, constraints on power consumption, cost, and weight can cause the navigation system to be comprised of a low-cost sensor suite. In this section, a low-cost antenna and low-cost receiver is used by the rover further degrading the AR of the relative positioning problem. Low-cost receivers, besides being less accurate, are typically single frequency and are known to require longer periods before fixing integers [25,68]. In addition, they are typically equipped with a TXCO internal oscillator which can suffer from aggressive clock bias drift in short periods. This can make maintaining fixed integer accuracy difficult to sustain. As discussed in [8] several techniques exist that statistically account for this drift and added uncertainty to the observables.

Another demonstrated technique for improving the AR for this scenario was demonstrated in [12,68]. In this thesis, the SD ambiguities are constrained by UWB ranging measurements which allows for improved TTFF and improved integer monitoring metrics for sustained accuracy.

4.3.1 UWB Measurement Model

The tightly-coupled algorithm uses the same SD GNSS measurement models as used in Section 3.1.2. The UWB measurement model has been studied before and information regarding its background can be found in [24]. In this work, the UWB measurements are treated as a precise SD pseudorange observable. The motivation for this is to improve the resolution of the ambiguity search space by the UWB precision. This is important due to the high levels of noise found in the pseudorange measurements created by low-cost equipment. Thus, we consider the following measurement model:

$$r_{cd}^{i} = |\rho_{cd}^{i}| + \eta_{cd}^{i} \tag{4.15}$$

Where ρ_{cd}^{i} is the geometric range between the two UWB modules and η_{cd}^{i} is the Gaussian noise modeled into the measurement. As discussed in [10], the uncertainty of apriori baseline knowledge plays a critical role in the ambiguity resolution problem. Excessive trust in this measurement will devalue the SD GNSS observables, and prevent the SD ambiguity estimates from converging to their correct value. Too little trust in the UWB measurement will cause the filter to behave like the nominal DRTK algorithm, and thus, not take advantage of the precise ranging information provided by the UWB [11].

The architecture of the considered navigation filter is complex, a holistic block diagram is demonstrated in Figure 4.44 depicting all stages of the filter.

GNSS measurements are first synced across platforms. UWB measurements are stored in a vector with their respective UNIX time stamps. The UWB measurement closest in time to the current synced GNSS measured are used as measurements to a discrete EKF. SD ambiguities estimates are recursively corrected and the DD operation is applied to the necessary matrices

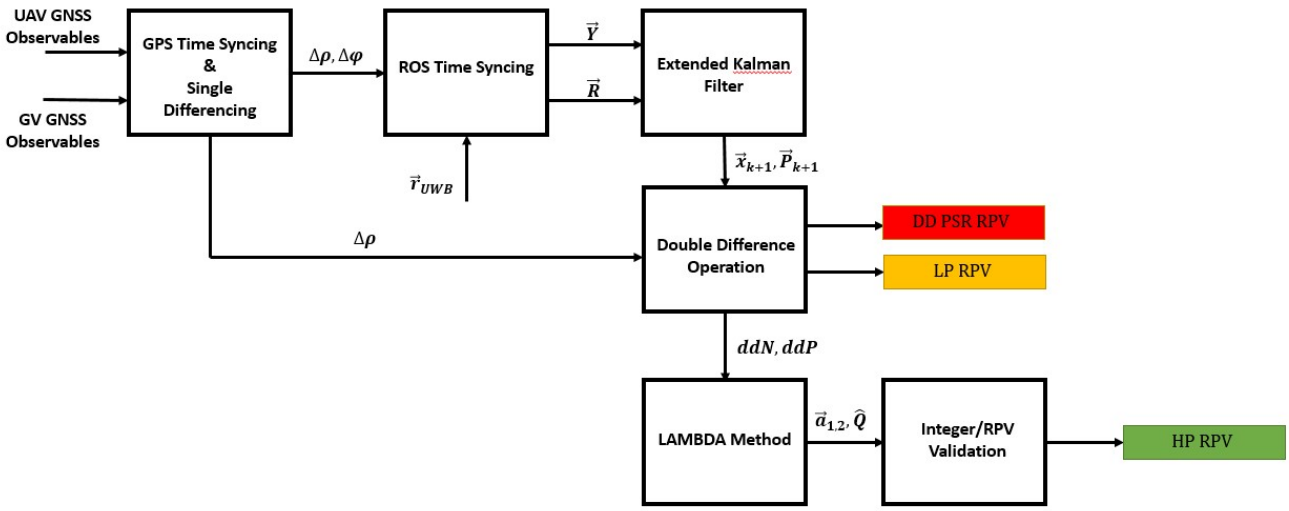

Figure 4.44: DGPS/UWB Navigation Filter Architecture

and vectors. For this algorithm, the left null space is not used since the geometry matrix is no longer symmetric with the inclusion of the UWB measurement. Similar integer monitoring metrics are used and the HP-RPV estimate is computed when a valid integer set is found. The following section discusses the formulation of the discrete EKF used for this thesis.

4.3.2 Discrete Extended Kalman Filter

Both sets of measurements have the ability to provide high-accuracy range measurements, but the difference in respective baselines should be considered. For this work, the UWB radios are assumed to be co-axial with the GPS antennas. This allows for the same relative position states to apply to both DGPS and UWB measurements. The state vector used in this filter is shown in Equation 4.16.

$$\vec{x} = \begin{bmatrix} \Delta X \\ \Delta Y \\ \Delta Z \\ cb_{ab}^{j} \\ \dot{cb}_{ab}^{j} \\ \Delta N_{ab}^{1} \\ \vdots \\ \Delta N_{ab}^{j} \end{bmatrix} \tag{4.16}$$

Where ΔX, ΔY, ΔZ are the relative positions states in the Earth centered Earth Fixed reference frame, cb_{ab}^{j} and $\dot{cb}_{ab}^{j}$ are the relative clock bias and relative clock bias drift respectively and ΔN_{ab}^{j} are the SD ambiguities for each tracked channel used in the filter. The considered measurements for the system are shown in Equation 4.17.

$$\vec{y}_k = \begin{bmatrix} \Delta\rho_k^1, GPS \\ \vdots \\ \Delta\rho_k^i, GPS \\ \Delta\phi_k^1, GPS \\ \vdots \\ \Delta\phi_k^i, GPS \\ r_k^{UWB} \end{bmatrix} \tag{4.17}$$

4.3.2.1 Process Model

The process model for the position states is simply the identity matrix. This is because the goal of the filter is not to track position states but to estimate the SD integer ambiguities found in the carrierphase measurements. Due to the disparity between each platform's internal oscillator, a second order process model was used to properly estimate the clock process dynamics. The power spectral density coefficients found in [1] were used to compute the receiver clock process model shown below:

$$Q_{cb} = \begin{bmatrix} S_f \Delta t + S_g \frac{\Delta t^3}{3} & S_g \frac{\Delta t^2}{2} \\ S_g \frac{\Delta t^2}{2} & S_g \Delta t \end{bmatrix} \tag{4.18}$$

In addition, the process gains for the ambiguity states were given low values since they are constant and will not change unless a cycle slip occurs. The overall process model can be seen below:

$$Q = \begin{bmatrix} Q_{x,y,z} I_{3x3} & 0_{3x2} & 0_{3xm} \\ 0_{2x3} & 2Q_{cb} & 0_{2xm} \\ 0_{mx3} & 0_{mx2} & Q_N I_{mxm} \end{bmatrix} \tag{4.19}$$

4.3.2.2 Observation Matrix

The observation matrix can be created by computing the Jacobian of the aforementioned measurement models and state vector. Note that this mapping from state to measurement domain assumes that the measurements contain the same baseline information, i.e. they are co-axial. Thus, the lever-arm between sensors should be minimized for actual implementation. This is further discussed in the experiment set-up section. The observation matrix is shown below:

$$C = \begin{bmatrix} H_{x,y,z} & 1 & 0 & 0_{nxm} \\ H_{x,y,z} & 1 & 0 & I_{nxn} \\ H_{x,y,z}^{UWB} & 0 & 0 & 0_{1xn} \end{bmatrix} \tag{4.20}$$

The geometry matrix corresponding to the UWB measurement is unique and is created using relative position information computed from a DGPS W.L.S. The formulation of these unit vectors is expressed in Equation 4.21.

$$H_{x,y,z}^{UWB} = \begin{bmatrix} \frac{\Delta X}{r_k^{UWB}}, \frac{\Delta Y}{r_k^{UWB}}, \frac{\Delta Z}{r_k^{UWB}} \end{bmatrix} \tag{4.21}$$

4.3.2.3 Measurement Weighting

As discussed earlier, the statistical variance of the individual measurements were quantified using a thermal noise model [1]. These were summed between receivers to account for the single difference operation, and summed again for the double difference operation standard in RTK/D-RTK algorithms. These values populated the first 2nx2n diagonal of the R matrix. The UWB stochastic term was tuned until attractive integer fixing results were obtained. Considerations were taken to ensure the uncertainty for the measurements masked the bimodal separation seen in the observables.

4.3.3 Experiment Setup

For this section, each platform is identified and followed by a specifications overview for the sensor suite under consideration. The static baseline test used a Trimble survey-grade antenna, a Novatel Pinwheel antenna, a Ublox EVK-M8T receiver/antenna kit, and two Novatel Propaks V3s. Novatel's GraftNav software was unable to maintain a fixed level solution when using the patch antenna and thus, the Novatel Pinwheel antenna was used to create the RTK truth solution. For the dynamic tests, a 2008 Subaru Outback XT was used as the ground vehicle (GV) while a Tarot meter class octacopter served as the aerial platform. The GV was equipped with a Novatel Propak V3, a Trimble Survey-Grade Antenna, and a single UWB module. The multirotor UAV was outfitted with a Ublox EVK-M8T receiver/antenna kit, a Novatel OEMstar board receiver, a MiniCircuits power splitter, and a single UWB module. A portion of the sensor suite specifications can be seen in Table 1. The full specifications for each product can be found in [19],[20],[21]. The data sets discussed in this work was taken on 09-10-2021 and 06-15-2021 at the Auburn NCAT Testing Facility on the skidpad respectively. This area has open-sky conditions and thus ideal for testing GNSS based navigation filters. A pulse integration index (PII) of 9 was used to allow for longer perceived baselines for dynamic testing. The Robotic Operating System (ROS) interpretation of Unix time was used to sync observables from both sensors in post process.

GNSS Receiver	Osscilator	Code Acc.	Phase Acc.	$H_{acc}(RMS)$
Novatel OEMstar	VCTCXO	5cm	0.6mm	1.5m
Ublox EVK-M8T	TCXO	N/A	N/A	2.5m
Novatel Propak V3	VCTCXO	4cm	0.5mm	1.2m

Table 4.2: GNSS Receiver Specifications

As can be seen in the images below, the baseline between phase centers of each sensor is non negligible. The baseline error on the UAV platform was 2.5 inches for both tests while the baseline error on the GV was 3.75 and 4.2 inches respectively. This totals to 15.9cm and 16.2cm in baseline error which is much greater than the 5cm maximum suggested by Broshears for consistent integer fixing. While this baseline requirement holds true for high grade receivers capable of sub-meter code-based ranging, this may be more flexible for the considered low cost receiver which experienced greater than 3m measurement variance for its code ranges. This allows the UWB range measurement to provide highly accurate ranging information, which constrains the SD ambiguity estimates. This baseline error was seen to cause erroneous ambiguity fixes as predicted by [4]. This is further discussed in a later section. To better assess the benefits of the tight-coupling, the static baseline test was used to establish a baseline of performance for the algorithm. For comparative analysis, the tightly-coupled algorithm is compared to its unaided counterpart. Results from both algorithms are compared to truth computed using Novatel's GraftNav software.

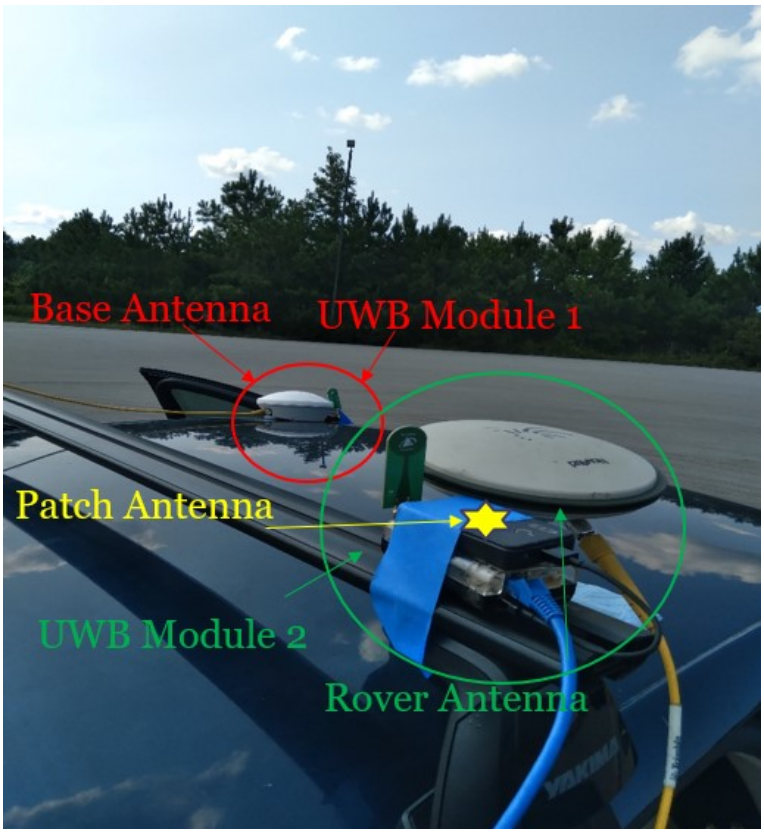

Figure 4.45: Static Baseline Setup

The second test assessed the effects of high dynamics on the ambiguity resolution and evaluated the aid provided by the UWB measurements. The same metrics of evaluation used for the static test are used here. Due to a connection issue with the Novatel OEMstar board, it was unable to log observables needed for truth. Thus, the dynamic data set will only be assessed relative to the stand-alone RTK algorithm. Images of all platforms and sensor suite can be seen in Figures 4.45, 4.46, 4.47 and 4.48. While not shown, the location of the patch antenna for the static baseline test is noted.

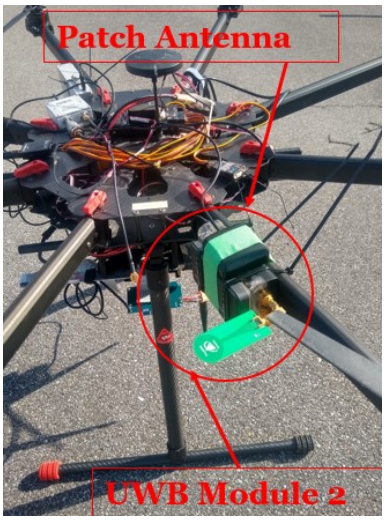

(a) UAV GNSS Equipment

(b) GV GNSS Antenna

Figure 4.46: Outfitted Sensor Packages

Figure 4.47: GV GNSS Receiver

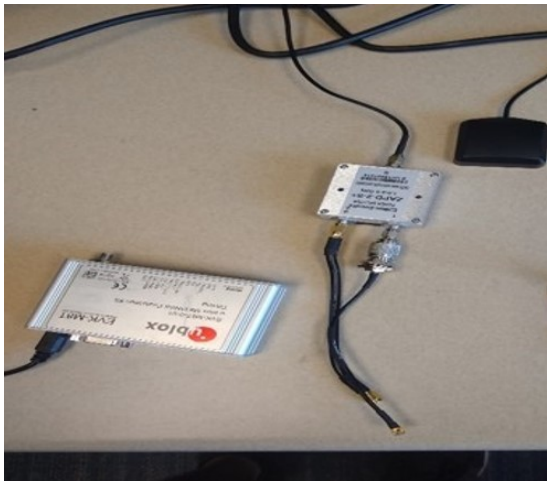

Figure 4.48: UAV GNSS Receiver

4.3.4 Experimental Validation

The results are organized as follows: first, diagnostic information for the data sets are discussed, more specifically, the CNO value and ambiguity resolution index (ARI) are used to assess the quality of GNSS observables perceived by each platform. Secondly, estimator performance is quantified by observing the residual error of the SD ambiguity estimates. Next, our DD ambiguity estimates are evaluated for correctness using the ratio test, a common metric used to determine if the set of integer ambiguity estimates are correct. A ratio threshold of 3 was used

for this work. Lastly, the computed RPV estimates are assessed and compared to GraftNav truth when available in a local ENU reference frame.

4.3.4.1 Static Baseline Test

The patch antenna was placed on the blue tape above the rover UWB sensor module in Figure 4.45. Thus, while a small offset would exist in the RPV solution and truth, the errors would be constant if the correct set of integer estimates were chosen. Figures 4.49 and 4.50 depict the diagnostic information regarding the data set.

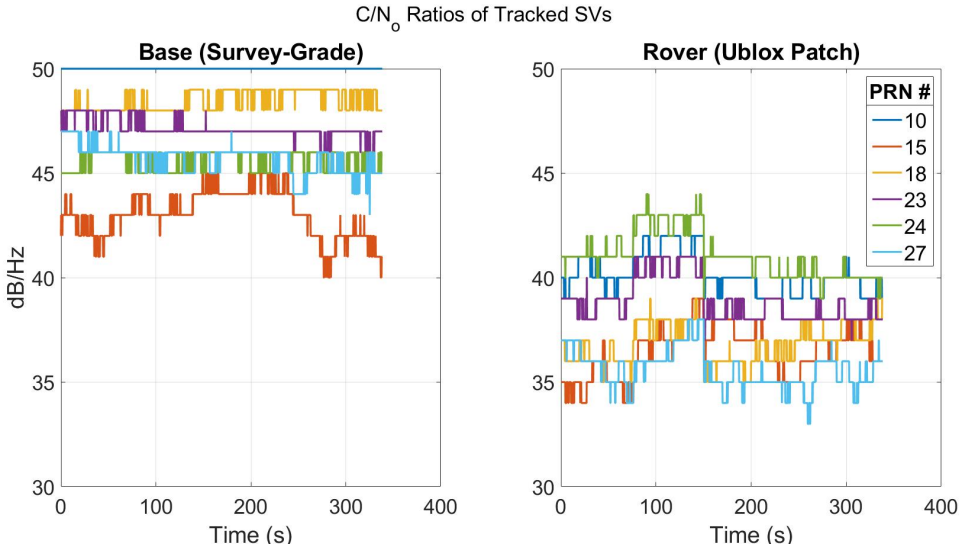

Figure 4.49: C/N_O ratios tracked channels

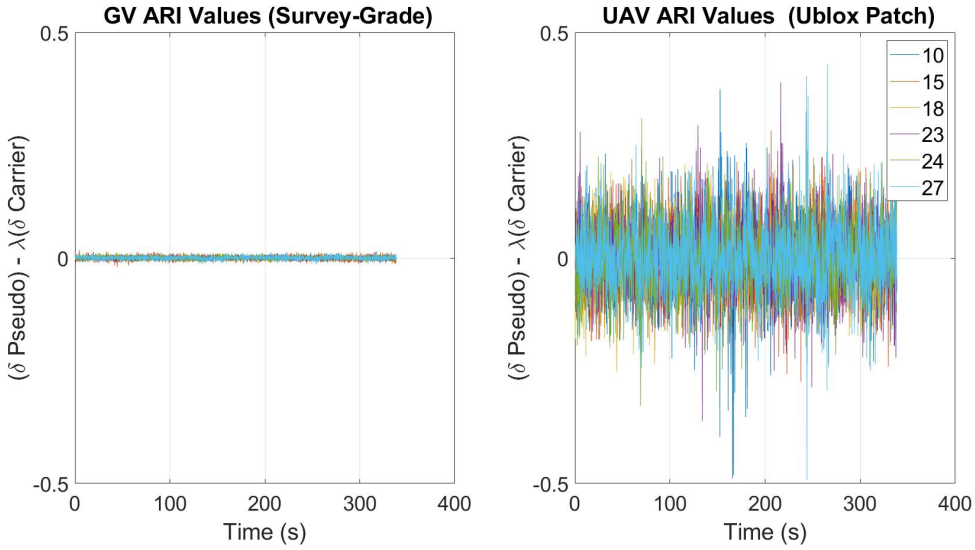

Figure 4.50: Ambiguity Resolution Index (m)

The difference in GNSS system quality between platforms is clearly seen from the diagnostic figures above. A difference of 5-10db/Hz is seen across all channel. This is attributed to the used equipment for the experiment. Note the difference in magnitude of each platform's ARI value. This can be attributed to the receiver and antenna quality on each platform. During this test, no cycle slips were reported by the receiver or observed in the measured ARI values of any channel. The residual error from the SD ambiguity estimates can be seen below:

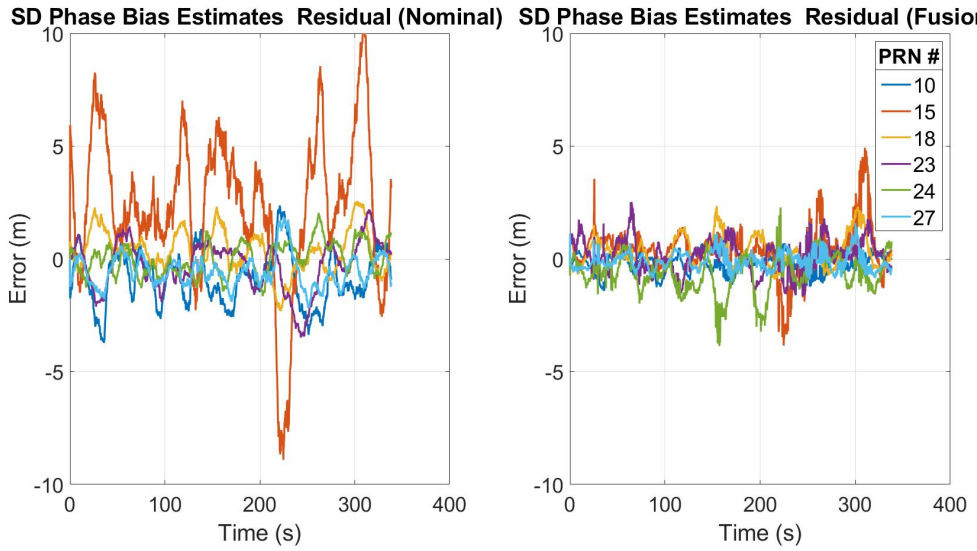

Figure 4.51: Ambiguity Resolution Index (m)

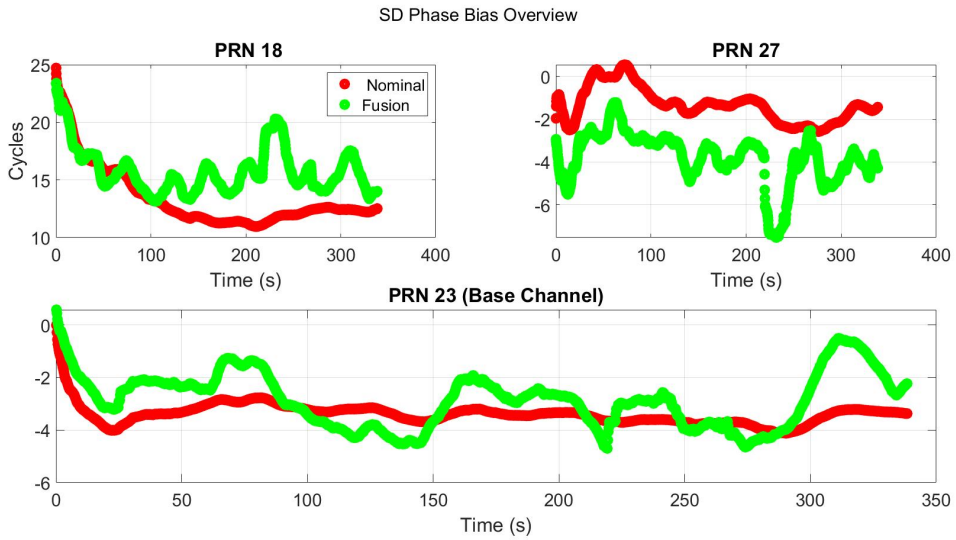

Figure 4.52: SD Ambiguity Estimates (cycles)

The usefulness of the UWB measurement constraint to the ambiguity search space is clearly seen in Figure 4.51. Channel 15 experiences the highest magnitudes of residual error as it is the lowest satellite along the horizon. Thus, we can expect high levels of error in its observables, particularly in the pseudoranges which are more susceptible to errors. This approach to ambiguity estimation uses a combination of SD pseudorange and SD carrier phase measurements. Thus, an increase in uncertainty in the pseudoranges can result in obscurity of the ambiguities within the carrier phase. The standard deviation for channel 15 was 3.29m for the nominal and 1.06m for the aided algorithm. A reduction in standard deviation was seen across all channels for the aided algorithm. To show the difference in floating point SD ambiguity estimates, Figure 4.52 illustrates the estimates of both the nominal and fusion architectures for a few channels. A double difference operation is applied to the SD ambiguity estimates and state covariances. These are provided to the LAMBDA method for integer fixing and validation. The DD ambiguity estimates for two channels are demonstrated below along with the computed ratio test value for both implementations:

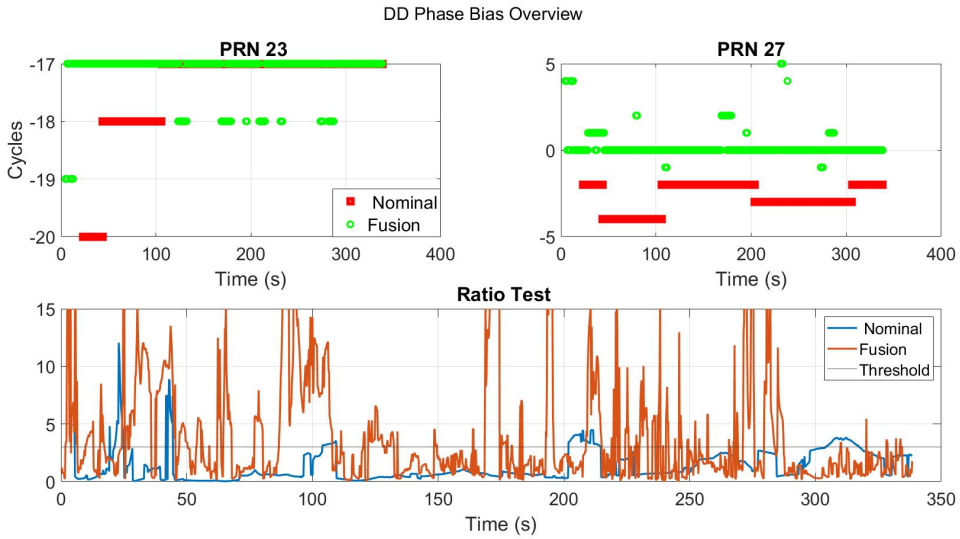

Figure 4.53: DD Ambiguity Time Series with Ratio Test

The aided implementation found a valid set of integers 4.6s into the data set. The unaided implementation found a valid set 23.2s into the data set. To avoid erroneous integer sets, an integer set was required to be observed for 10 consecutive epochs in addition to passing the ratio test. Even with this integer validation strategy, convergence to a constant was not seen

in either implementation. This can be seen in Figure 4.53 where both formulations are seen to jump between valid integer sets. This sporadic jumping is attributed to the noisy pseudorange measurements used by the filter.

Utilizing the passing integer sets, the time series for the resulting RPV in the ENU frame is shown below:

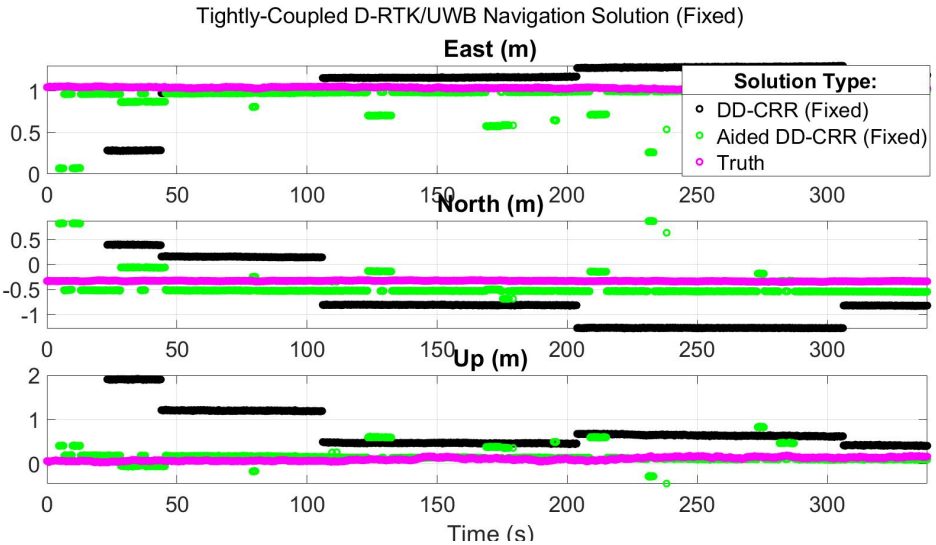

Figure 4.54: Estimated RPV in local ENU Frame

The computed HP-RPV estimates were differenced by the truth RPV provided by Graft-Nav. These metrics can be seen below:

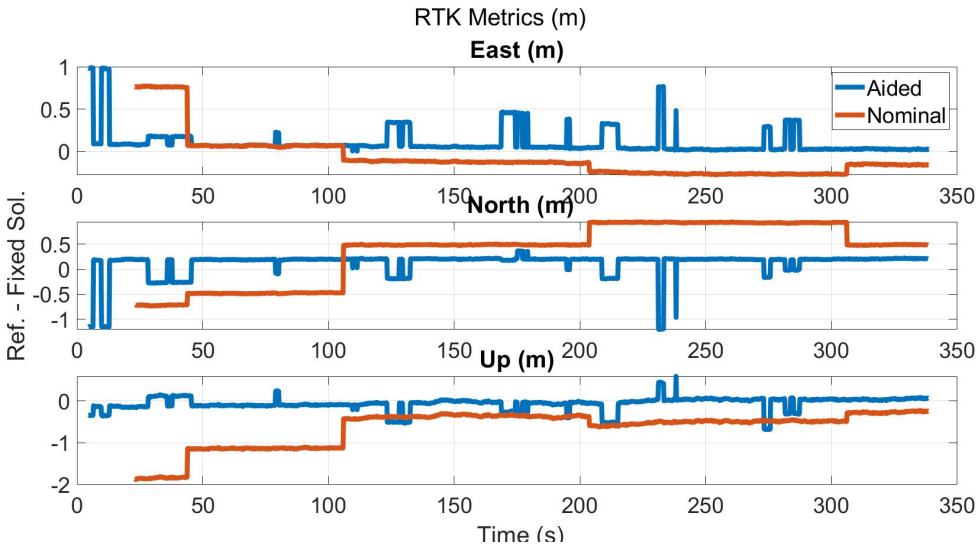

Figure 4.55: Ambiguity Resolution Index (m)

The aided implementation is seen to more consistently depict the RPV estimate. To better assess the accuracy of each method, the mean error of each direction is shown in Table 4.3.

Direction	Nominal	Aided
East	-7.60cm	10.3cm
North	36.1cm	12.3cm
Up	-65.0cm	-6.0cm

Table 4.3: Static Baseline RTK Metrics

4.3.4.2 Dynamic Baseline Test

The dynamic baseline test was split in three parts, a static portion lasting about 90 seconds, a dynamic portion where the UAV moved routinely around the skidpad, and lastly a static ending period. To observe the affects of high dynamics on the ambiguity resolution of the problem, only the dynamic portion is discussed. Using MAVROS, way-points were created around the skidpad at a 30 meter altitude ceiling. MAVROS is a interface between platforms and various autopilot programs within the ROS environment. This knowledge is later used to assess both algorithms. Figure 4.56 depicts the C/NO values and computed ARI values seen in the tracked channels during this data set:

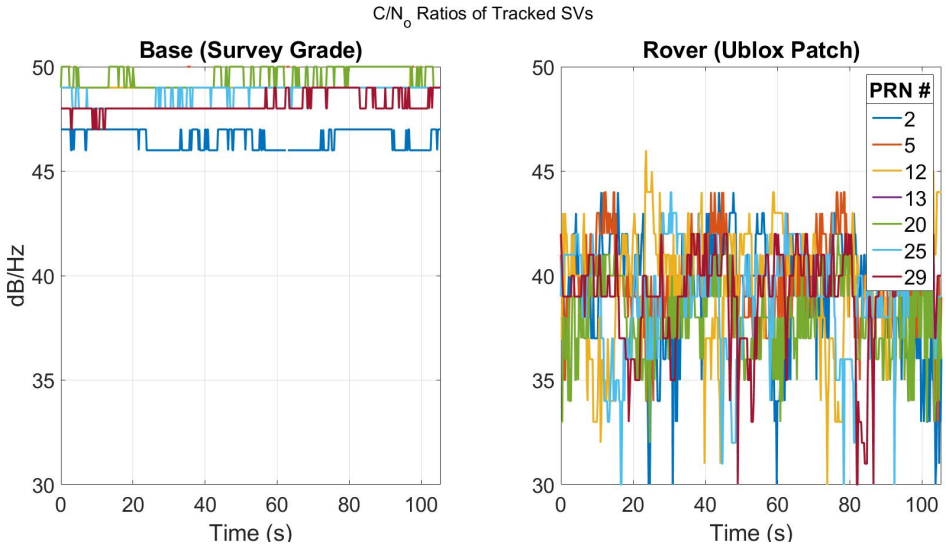

Figure 4.56: C/N_O ratios tracked channels

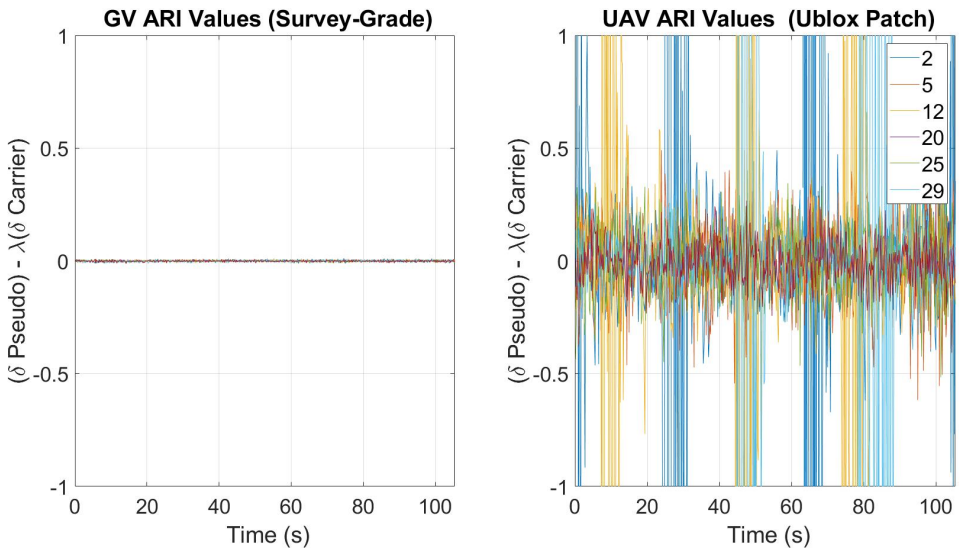

Figure 4.57: Ambiguity Resolution Index (m)

The effects of UAV dynamics can be seen in both figures. These periods of degraded GNSS quality can make it difficult to accurately estimate the SD ambiguity values. Furthermore, these periods heighten the probability of channels experiencing cycle-slips which are typically predicted when the ARI values exceeds a threshold of 1. Because of the Ublox's attempts of ambiguity removal [20], a threshold of 1 was too stringent of a filter for the channels. A threshold of 6 was used for this work while also relying on the receiver's locktime information to avoid using channels which had undergone a cycle-slip. The residual error from our SD ambiguity estimates can be seen below. The precise baseline constraint provided by the UWB is seen to reduce error in the ambiguity estimates during the static portions and also during the dynamic portions where the ambiguities are obscured due to increased measurement uncertainty.

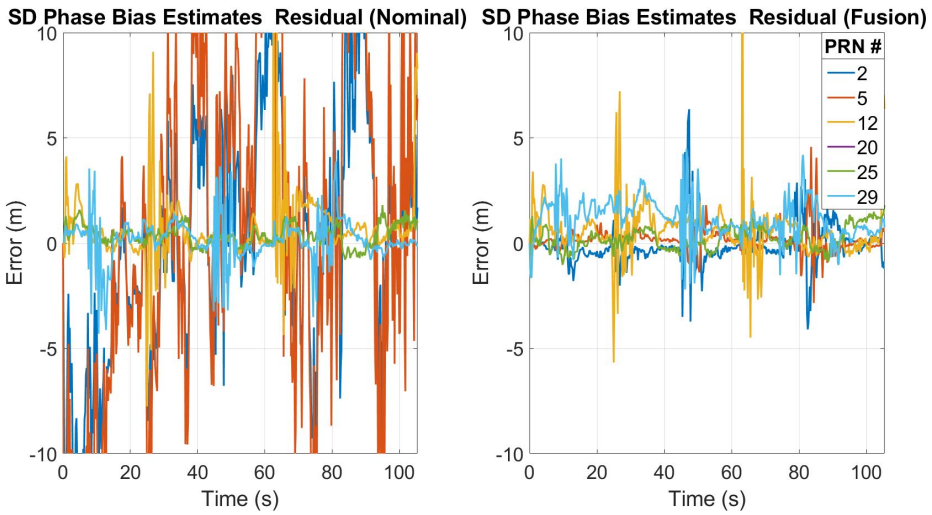

Figure 4.58: SD Residual Error (m)

A double difference operation is performed to remove the remaining modes of error in the GNSS observables. These DD ambiguity estimates, and their respective covariances from the EKF, are used in the LAMBDA method to attempt to fix the integer ambiguities. The time series of two resulting ambiguities are demonstrated below in addition to the ratio test at every measurement update:

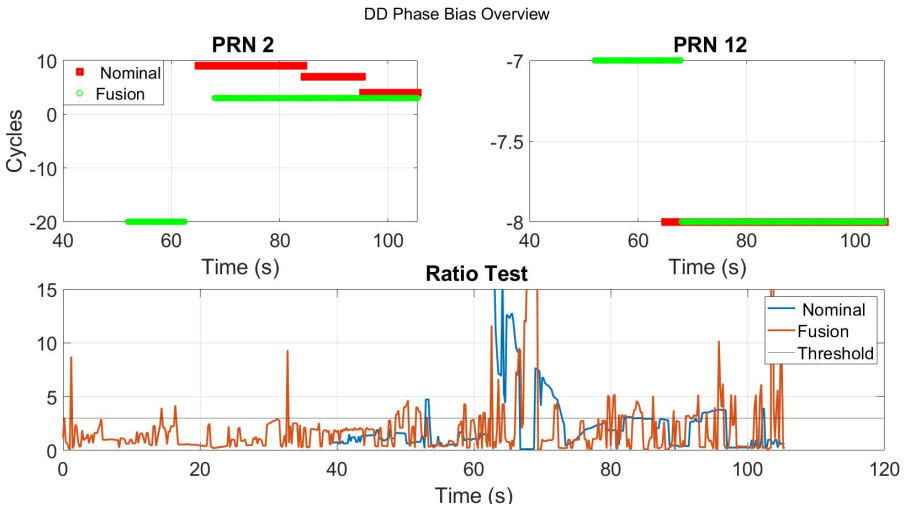

Figure 4.59: DD Ambiguity Time Series with Ratio Test

The aided algorithm finds a valid integer set 52 seconds into the dynamic data. Its unaided counterpart finds its first fix 65 seconds into the data. Unlike the static baseline case, the integer estimates for the aided algorithm do not experience the sporadic jumps between valid sets. The rover receiver lost lock of channel 2 61 seconds into the data. The resulting integer set found

by the aided solution is converged to for the remainder of the data. Since truth was unable to be computed, the resulting HP-RPV estimates are compared to the DD-PSR RPV. The resulting RPV in the ENU frame is depicted below:

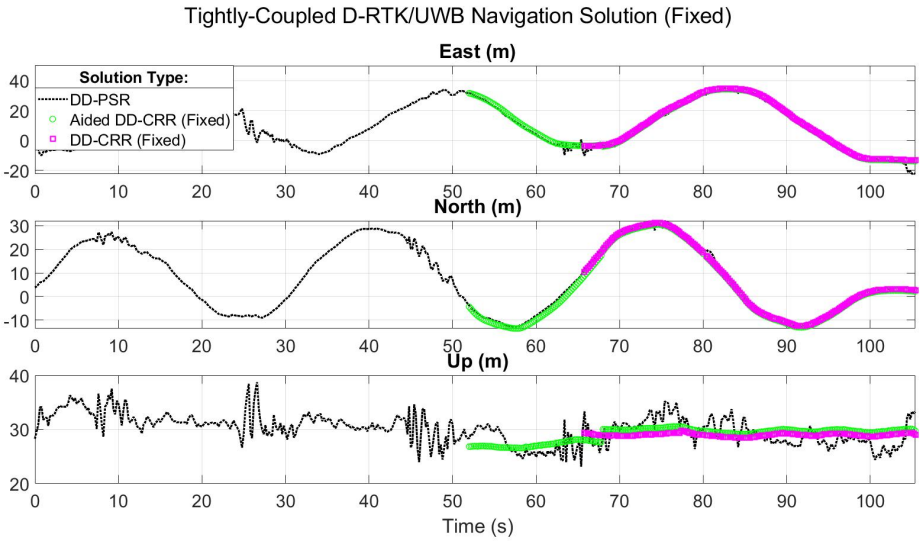

Figure 4.60: Estimated RPV in local ENU Frame

To further validate the HP-RPV solution, the norm of the baseline is compared to the UWB ranging measurements. This comparison is shown below:

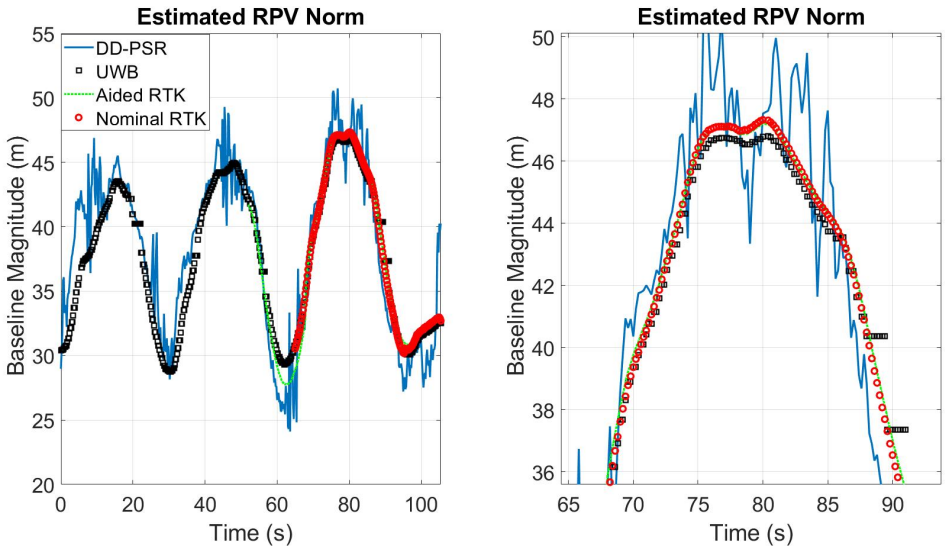

Figure 4.61: Estimated RPV Norm

The UWB modules were seen to experience dropouts during the dynamic portion of the test. An example of this can be seen near 20 seconds into the data set. This would cause issues

in the tightly-coupled formulation since the UWB range measurement would not accurately describe the current baseline between GPS antennas. While not an accurate reference to the trajectory taken by the UAV, the HP-RPV estimates are compared to the DD-PSR RPV to better assess their accuracy. Knowledge of the 30m ceiling is used to evaluate the accuracy of the estimated RPV in the Up direction. Sub-decimeter level accuracy is seen after the second set of valid integers is found for the aided implementation. These metrics can be seen in Figure 4.62

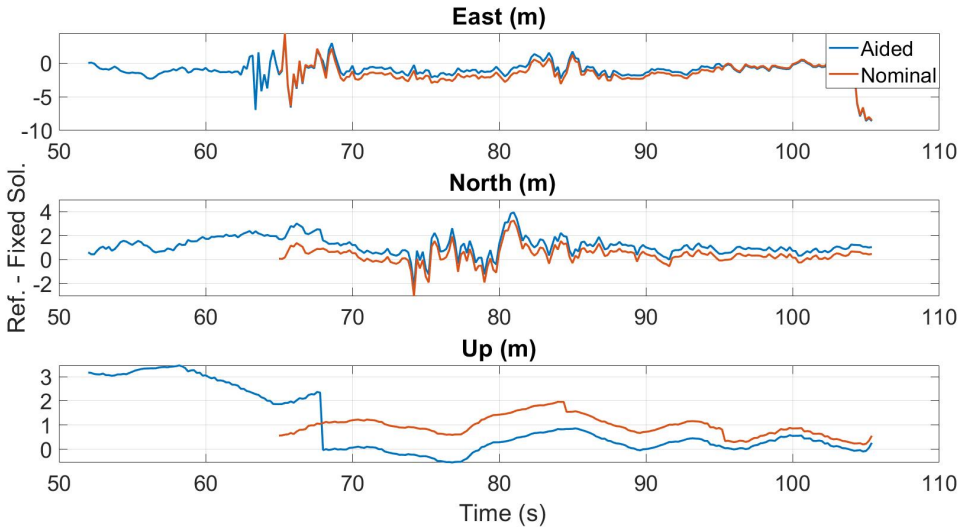

Figure 4.62: RTK Error Metrics

An improvement to the TTFF was seen in both the static and dynamic baseline experiments for the aided algorithm when compared to its nominal counterpart. An increase in HP-RPV availability was seen when using the tightly-coupled formulation. With the lack of high precision truth for the dynamic tests, the aided algorithm still out-performed the nominal formulation when assessing the Up-direction. The aided solution is seen to find the correct integer set near 78 seconds where a reduction in Up error is seen to occur.

Chapter 5

Conclusion

This thesis presented three DGPS techniques capable of providing a RTK level accurate relative navigation solution. It is shown that these algorithms work with varying equipment grade where the nominal DRTK algorithm fails. Chapter 2 describes the GNSS constellations considered in this work. Chapter 3 distinguishes the subtleties between RTK and DRTK positioning algorithms and discusses the nominal DRTK algorithm. It also demonstrates the baseline performance metrics of the standard DRTK algorithm given three unique circumstances. Chapter 4 provides the architecture of the navigation filters that are capable of remedying the problems highlighted in Chapter 3.

The Multi-GNSS DRTK algorithm was shown to effectively improve the AR of static and dynamic baselines when using a survey-grade antenna. The equipment provided good signal reception and accurate observables. Considering GPS, Galileo, and BeiDou constellations allowed for a significant improvement to time-to-first-fix when limited to a single frequency. Through this test, it was shown that robust integer fixing is possible when ARI values are greater than 3 cycles. Centimeter level accuracy was maintained for both the static and dynamic baseline test.

The adaptive DRTK algorithm was shown to allow for a high-precision navigation solution to be computed when using a low-cost patch antenna. This trend is seen for both static and dynamic baselines. The nominal DRTK algorithm and Novatel GraftNAV software was incapable of providing the same level solution as the proposed algorithm. The differences between the used equipment is seen through diagnostic information. It is shown that by more accurately weighing the inputs to the filter, the LAMBDA method is able to more effectively

decorrelate the recursive covariance knowledge leading to fixed integer precision. Centimeter level accuracy was seen for both the static and dynamic baselines.

The advantages of coupling UWB range measurements with low cost SD GPS observables was demonstrated through the tightly-coupled EKF formulation. The UWB range measurement acts as precise baseline constraint when estimating the SD float ambiguity values. This constraint improves the resolution of the DD ambiguity estimates and allows for rapid fixing to a valid integer set. An improvement to time-to-fix was seen in both tests for the aided algorithm when compared to its nominal counterpart. In addition, the aided algorithm was found to more accurately depict the RPV for the static baseline. The resulting RTK metrics demonstrated a 24cm improvement in the North direction and 59cm improvement in the Up direction. The aided algorithm was also found to converge to a set of valid integer sets 68 seconds into the dynamic test. Its nominal counterpart failed to converge to a valid integer set for the entire period of interest.

5.1 Future Work

This work can be extended for future work in several ways. A few possibilities are listed below.

1. The multi GNSS implementation only considers the single frequency scenario. While it had promising results, the filter should be extended to consider dual-frequency observables from available constellations. This will increase the robustness of the integer fixing piece of the algorithm. The computational load from dual-frequency multi constellation should be considered before real-time use on autonomous systems. A real-time implementation of the algorithm should be made to allow for precise relative navigation in GNSS limited environments.

2. The adaptive implementation was shown to work when initialized with static or dynamic baselines. However, valid integer fixing still needs to be explored for fully dynamic scenarios since the time-to-first-fix did not occur until after the dynamic period ended. In addition, longer of intervals data should be considered to further inspect the estimated

measurement trajectories to the receiver reported trajectories. A real-time implementation of the algorithm should be made allowing for precise relative navigation of smaller platforms such as UAVs.

3. The tightly-coupled implementation was demonstrated to perform well for static and dynamic baselines. The addition of multiple constellations into the filter needs to be explored. Further testing is needed to validate the HP-RPV estimates found during high dynamic maneuvering. In addition, a method for filtering the sporadic jumps in valid integer sets is still needed for static cases. A moving average filter could alleviate some of this variance while adding minimal complexity to the algorithm. The erroneous sets could also be alleviated by minimizing the phase center baseline error between sensors. Lastly, while the effects of rover dynamics on the ambiguity resolution were evaluated, the combination of base/rover dynamics must be assessed. A real-time implementation of the algorithm should be made allowing for precise relative navigation of a cost-limited UAV-UGV team.

References

[1] William T. E. ”Path Duplication Using GPS Carrier Based Relative Position for Automated Ground Vehicle Convoys”. PhD Dissertation. Auburn University (2010). https://etd.auburn.edu/handle/10415/2109

[2] Teunissen, P. J. G., “The Least-Squares Ambiguity Decorrelation Adjustment: A Method for Fast GPS Integer Ambiguity Estimation,” Journal of Geodesy, Vol. 70, Nos. 1–2, Nov. 1995, pp. 65–82.

[3] de Jonge, P., and Tiberius, C., “The LAMBDA Method for Integer Ambiguity Estimation: Implementation Aspects,” Delft Geodetic Computing Centre, LGR series, No. 12, available online at http:// enterprise.lr.tudelft.nl/mgp/modules.php?op=modloadname=Lambdafile= indexfunc=displaypapers, Aug. 1996, pp. 1–41 [retrieved 21 Dec. 2005].

[4] TeunissenPJG(1997a)AcanonicaltheoryforshortGPSbaselines.Part I: the baseline precision. J Geod 71(6):320–336

[5] TeunissenPJG(1997b)AcanonicaltheoryforshortGPSbaselines.Part II:theambiguityprecisionandcorrelation.JGeod71(7):389–401

[6] TeunissenPJG(1997c)AcanonicaltheoryforshortGPSbaselines.Part III:thegeometryoftheambiguitysearchspace.JGeod71(8):486– 501

[7] Teunissen PJG (1997d) A canonical theory for short GPS baselines. Part IV: precision versus reliability. J Geod 71(9):513–525

[8] Odolinski, R., Teunissen, P.J.G. Single-frequency, dual-GNSS versus dual-frequency, single-GNSS: a low-cost and high-grade receivers GPS-BDS RTK analysis. J Geod 90, 1255–1278 (2016). https://doi.org/10.1007/s00190-016-0921-x

[9] Scott M. ” Closely Coupled GPS.INS Relative Positioning for Automated Vehicle Convoys”. Master’s Thesis (2011). Auburn University. https://etd.auburn.edu/handle/10415/2533

[10] Troupe T. T. ” Multi-Antenna GPS for Improved Carrier Phase Positioning in Autonomous Convoys”, Master’s Thesis (2019). Auburn University.https://etd.auburn.edu/xmlui/handle/10415/6900

[11] Broshears E. ”Ultra-Wideband Radio Aided Carrier Phase Ambiguity Resolution in Real-Time Kinematic GPS Relative Positioning”. Master’s Thesis (2013). Auburn University. https://etd.auburn.edu/xmlui/handle/10415/3704

[12] Glenn M., Kyle K., Richard K. ” Tightly-coupled GPS/UWB Integration”. *The Journal of Navigation* (2010). Vol.63 No.1.

[13] Gross J., Dewberry, B. ” Tightly-Coupled GPS/UWB-Ranging for Relative Navigation During Formation Flight”. *Proceedings of the 27th International Technical Meeting of the Satellite Division of The Institute of Navigation* (2014) pp. 1698 - 1708.

[14] Correal N. S., Kyperountas S., Shi Q., Welborn M., ”An UWB relative location system,” *IEEE Conference on Ultra Wideband Systems and Technologies* 2003, Reston, VA, USA, 2003, pp. 394-397, doi: 10.1109/UWBST.2003.1267871.

[15] Jung S., Ariyur K. B., ”Compensating UAV GPS data accuracy through use of relative positioning and GPS data of UGV”. *Journal of Mechanical Science and Technology* Volume 31, 4471–4480 (2017). https://doi.org/10.1007/s12206-017-0847-0.

[16] Sivaneri V. O., Gross J. ”Flight-testing of a cooperative UGV-to-UAV strategy for improved positioning in challenging GNSS environments”. *Aerospace*

Science and Technology, Volumes 82-83, 2018, Pages 575-582, ISSN 1270-9638,https://doi.org/10.1016/j.ast.2018.09.035.

[17] Brandao A. S. , Sarcinelli-Filho M. , R. Carelli, "Leader-following control of a UAV-UGV formation," *2013 16th International Conference on Advanced Robotics (ICAR)*, Montevideo, Uruguay, 2013, pp. 1-6, doi: 10.1109/ICAR.2013.6766592.

[18] Xu J., Ma M., Law C. L., "Position Estimation Using UWB TDOA Measurements,". *2006 IEEE International Conference on Ultra-Wideband*. Waltham, MA, USA, 2006, pp. 605-610, doi: 10.1109/ICU.2006.281617.

[19] Perakis H., Gikas V., "Evaluation of Range Error Calibration Models for Indoor UWB Positioning Applications,". *2018 International Conference on Indoor Positioning and Indoor Navigation (IPIN*), Nantes, 2018, pp. 206-212, doi: 10.1109/IPIN.2018.8533755.

[20] Delamare, M., Boutteau, R., Savatier, X., Iriart, N. "Static and Dynamic Evaluation of an UWB Localization System for Industrial Applications". Sci 2020, 2, 23.

[21] Gebre-Egziabher D., Hayward R. C., Powell J. D., "A low-cost GPS/inertial attitude heading reference system (AHRS) for general aviation applications," IEEE 1998 Position Location and Navigation Symposium (Cat. No.98CH36153), Palm Springs, CA, USA, 1998, pp. 518-525, doi: 10.1109/PLANS.1998.670207.

[22] Lazzari F., Buffi A., Nepa P., Lazzari S., "Numerical Investigation of an UWB Localization Technique for Unmanned Aerial Vehicles in Outdoor Scenarios,". *IEEE Sensors Journal*, vol. 17, no. 9, pp. 2896-2903, May 1, 2017, doi: 10.1109/JSEN.2017.2684817.

[23] H. Qin et al., "Autonomous Exploration and Mapping System Using Heterogeneous UAVs and UGVs in GPS-Denied Environments," in IEEE Transactions on Vehicular Technology, vol. 68, no. 2, pp. 1339-1350, Feb. 2019, doi: 10.1109/TVT.2018.2890416.

[24] Sahinoglu Z., Gezici S., Guvenc I., "Ultra-Wideband Positioning Systems: Theoretical Limits, Ranging Algorithms, and Protocols"

[25] Pesyna, Kenneth M., Jr.,, Heath, Robert W., Jr.,, Humphreys, Todd E., "Centimeter Positioning with a Smartphone-Quality GNSS Antenna," Proceedings of the 27th International Technical Meeting of the Satellite Division of The Institute of Navigation (ION GNSS+ 2014), Tampa, Florida, September 2014, pp. 1568-1577.

[26] K. M. Pesyna, T. E. Humphreys, R. W. Heath, T. D. Novlan and J. C. Zhang, "Exploiting Antenna Motion for Faster Initialization of Centimeter-Accurate GNSS Positioning With Low-Cost Antennas," in IEEE Transactions on Aerospace and Electronic Systems, vol. 53, no. 4, pp. 1597-1613, Aug. 2017, doi: 10.1109/TAES.2017.2665221.

[27] https:// hexagondownloads.blob.core.windows.net/public/Novatel/assets/Documents/Manuals/om-20000126/ om-20000126.pdf

[28] https:// hexagondownloads.blob.core.windows.net/public/Novatel/assets/Documents/Papers/ ProPakV3/ ProPakV3.pdf

[29] *https://www.u-blox.com/sites/default/files/products/documents/u-blox8-M8*$_{R}eceiverDescrProtSpec_{U}BX - 13003221.pdf$

[30] "TEX https://gssc.esa.int/navipedia/index.php/GPS$_{S}pace_{S}egment"T_{E}X$.

[31] https://gssc.esa.int/navipedia/index.php/Galileo$_{F}uture_{a}nd_{E}volutions"T_{E}X$.

[32] https://gssc.esa.int/navipedia/index.php/BeiDou$_{G}eneral_{I}ntroduction"T_{E}X$.

[33] https://eur-lex.europa.eu/LexUriServ/LexUriServ.do?uri=OJ:L:2008:196:0001:0011:en:PDF.

[34] https://en.wikipedia.org/wiki/BeiDou.

[35] Verhagen, Sandra Li, Bofeng. (2012). LAMBDA software package: Matlab implementation, Version 3.0.

[36] Petovello, Mark G., et al. "Demonstration of inter-vehicle UWB ranging to augment DGPS for improved relative positioning." Proceedings of the 23rd International Technical Meeting of the Satellite Division of The Institute of Navigation (ION GNSS 2010). 2010.

[37] GPS ICD

[38] Galileo ICD

[39] BeiDou ICD

[40] Rinex 3.04

[41] Woo, Rinara, Eun-Ju Yang, and Dae-Wha Seo. ”A fuzzy-innovation-based adaptive Kalman filter for enhanced vehicle positioning in dense urban environments.” Sensors 19.5 (2019): 1142.

[42] Wang, Jinling. ”Stochastic Modeling for Real-Time Kinematic GPS/GLONASS Positioning.” Navigation 46.4 (1999): 297-305.

[43] Odolinski, Robert, and Peter JG Teunissen. ”An assessment of smartphone and low-cost multi-GNSS single-frequency RTK positioning for low, medium and high ionospheric disturbance periods.” Journal of Geodesy 93.5 (2019): 701-722.

[44] Stempfhuber, W., and M. Buchholz. ”A precise, low-cost RTK GNSS system for UAV applications.” Proc. of Unmanned Aerial Vehicle in Geomatics, ISPRS (2011).

[45] Matias, Bruno, et al. ”High-accuracy low-cost RTK-GPS for an unmannned surface vehicle.” OCEANS 2015-Genova. IEEE, 2015.

[46] Skoglund, Martin, et al. ”Static and dynamic performance evaluation of low-cost RTK GPS receivers.” 2016 IEEE Intelligent Vehicles Symposium (IV). IEEE, 2016.

[47] Takasu, Tomoji, and Akio Yasuda. ”Development of the low-cost RTK-GPS receiver with an open source program package RTKLIB.” International symposium on GPS/GNSS. Vol. 1. International Convention Center Jeju Korea, 2009.

[48] Odolinski, Robert, and Peter JG Teunissen. ”Best integer equivariant estimation: performance analysis using real data collected by low-cost, single-and dual-frequency, multi-GNSS receivers for short-to long-baseline RTK positioning.” Journal of Geodesy 94.9 (2020): 1-17.

[49] Kim, Euiho. ”GNSS Precise Relative Positioning Using A Priori Relative Position in a GNSS Harsh Environment.” Sensors 21.4 (2021): 1355.

[50] Psiaki, Mark L., and Shan Mohiuddin. ”Global positioning system integer ambiguity resolution using factorized least-squares techniques.” Journal of Guidance, Control, and Dynamics 30.2 (2007): 346-356.

[51] Busse, Franz D., Jonathan P. How, and James Simpson. ”Demonstration of adaptive extended Kalman filter for low-earth-orbit formation estimation using CDGPS.” NAVIGATION, Journal of the Institute of Navigation 50.2 (2003): 79-94.

[52] Psiaki, Mark L. ”Kalman filtering and smoothing to estimate real-valued states and integer constants.” Journal of guidance, control, and dynamics 33.5 (2010): 1404-1417.

[53] Olynik, Michael. ”Temporal characteristics of GPS error sources and their impact on relative positioning.” University of Calgary: Calgary, Canada (2002).

[54] Li, Bofeng, Sandra Verhagen, and Peter JG Teunissen. ”Robustness of GNSS integer ambiguity resolution in the presence of atmospheric biases.” GPS solutions 18.2 (2014): 283-296.

[55] Teunissen, P. J. G. ”GPS ambiguity resolution: impact of time correlation, cross-correlation and satellite elevation dependence.” Studia Geophysica et Geodaetica 41.2 (1997): 181-195.

[56] Petovello, Mark G., et al. ”Consideration of time-correlated errors in a Kalman filter applicable to GNSS.” Journal of Geodesy 83.1 (2009): 51-56.

[57] Miller, Charles, Kyle O’Keefe, and Yang Gao. ”Operational performance of RTK positioning when accounting for the time correlated nature of GNSS phase errors.” Proceedings of the 23rd International Technical Meeting of the Satellite Division of The Institute of Navigation (ION GNSS 2010). 2010.

[58] Verhaegen, Michel, and Paul Van Dooren. ”Numerical aspects of different Kalman filter implementations.” IEEE Transactions on Automatic Control 31.10 (1986): 907-917.

[59] Mohiuddin, Shan, and Mark L. Psiaki. ”High-altitude satellite relative navigation using carrier-phase differential global positioning system techniques.” Journal of Guidance, Control, and Dynamics 30.5 (2007): 1427-1436.

[60] Dong, D., et al. ”Mitigation of multipath effect in GNSS short baseline positioning by the multipath hemispherical map.” Journal of Geodesy 90.3 (2016): 255-262.

[61] Teunissen, P. J. G. ”Closed form expressions for the volume of the GPS ambiguity search spaces.” Artificial Satellites- Planetary Geodesy 32.1 (1997): 5-20.

[62] Psiaki, Mark L., and Shan Mohiuddin. ”Modeling, analysis, and simulation of GPS carrier phase for spacecraft relative navigation.” Journal of Guidance, Control, and Dynamics 30.6 (2007): 1628-1639.

[63] Humphreys, Todd E., et al. ”On the feasibility of cm-accurate positioning via a smartphone’s antenna and GNSS chip.” 2016 IEEE/ION position, location and navigation symposium (PLANS). IEEE, 2016.

[64] Subirana, Sanz Jaume, et al. GNSS Data Processing. Vol. 1, ESA Communications, 2013.

[65] Kaplan, Elliott D. Understanding GPS: Principles and Applications. Artech House, 1996.

[66] Chhabra, A.; Venepally, J.R.; Kim, D. Measurement Noise Covariance-Adapting Kalman Filters for Varying Sensor Noise Situations. Sensors 2021, 21, 8304. https://doi.org/10.3390/s21248304

[67] Campos-Vega, Christian J., Kamarath, Dan, Sprunger, John David, Martin, Scott, Bevly, David, ”Precise Relative Positioning in GPS-Degraded Environments using a DGPS/UWB Navigation Filter,” Proceedings of the 34th International Technical Meeting of the Satellite Division of The Institute of Navigation (ION GNSS+ 2021), St. Louis, Missouri, September 2021, pp. 2526-2543.

Appendix A

Consecutive Ambiguity Counter Analysis

The results discussed in Chapters 3 and 4 used a CAC threshold of 10. This value was chosen based on results where the CAC threshold was varied and the accuracy of the resulting HP-RPV solution was compared to truth. This section explains the formulations used to evaluate the success rate and results of these tests.

A key metric used to assess integer correctness is the integer success rate. Its formulation can be seen in Equation A.1.

$$P^i_{int} = \frac{intCounter}{(totalSamples - TTFF/T_s)} \tag{A.1}$$

Where $intCounter$ is the number of observation periods where the resulting normalized HP-RPV was within 10 centimeters of the normalized truth.The $totalSamples$ variable is the total number of observation periods considered for any given run. $TTFF$ is the time-to-first-fix for a given run and T_s is the sample time for a given data set. The success rate and time-to-first-fix are compared for the static baseline tests for each experiment setup.

The high-grade equipment setup is studied first. Tables A.1 and A.2 shows the performance metrics for the GPS only and multi-GNSS algorithms respectively.

CAC	1	3	5	7	10	20	50
TTFF (sec)	285	376	379	381	384	450	N/A
$P^i_{INT}(\%)$	88.2	91.6	100	100	100	100	N/A

Table A.1: Static Baseline Test: High-Grade Antenna (GPS Only)

CAC	1	3	5	7	10	20	50
TTFF (sec)	5	6	8	10	14	25	59
$P^i_{INT}(\%)$	99.3	99.3	99.4	99.4	100	100	100

Table A.2: Static Baseline Test: High-Grade Antenna (Multi-GNSS)

The robustness of the integer fixing strategy is observed to improve with an increasing CAC threshold. This is true for both algorithms but is clearly observed in the GPS only case who experiences less then 90% success rate when using a CAC threshold of 1. A 100% success rate is achieved by both algorithms with a CAC threshold of 10. It should be noted that at a CAC

threshold of 50, only the multi-GNSS algorithm achieves 100% success rate. This stems from the length of the data set used for the study. The GPS only algorithm can achieve a HP-RPV solution but is incapable of satisfying the CAC threshold and thus the HP-RPV solution is never computed by the algorithm. Thus, while the CAC threshold is observed to improve robustness of the integer monitoring portion of the algorithm, the strictness of the threshold should be considered to prevent the HP-RPV solution from being avoided. Important parameters used by each of the algorithms are listed in Table A.3.

	GPS only	Multi GNSS
$T_s(sec)$	1	1
$P_o(cycles)$	0.5	0.5
$Q_o(cycles)$	100e-06	100e-06

Table A.3: Variables of Interest

The high-grade receivers with low-grade antenna experiment set-up is studied next. The CAC threshold was varied for both the nominal and adaptive EKF algorithms. The same performance metrics were assessed and are demonstrated in Tables A.4 and A.5.

CAC	1	3	5	7	10	20	50
TTFF (sec)	N/A	N/A	N/A	N/A	N/A	N/A	N/A
$P^i_{INT}(\%)$	N/A	N/A	N/A	N/A	N/A	N/A	N/A

Table A.4: Static Baseline Test: Low-Grade Antenna (Patch)

CAC	1	3	5	7	10	20	50
TTFF (sec)	447	448	451	453	456	470	N/A
$P^i_{INT}(\%)$	88.2	91.2	100	100	100	100	N/A

Table A.5: Static Baseline Test: Low-Grade Antenna (Adaptive Patch)

The nominal EKF algorithm is unable to achieve a HP-RPV solution regardless of the CAC threshold. The adaptive EKF however, experiences an improvement to integer fixing robustness with increasing CAC threshold. A similar cut-off point for HP-RPV availability is observed with a CAC threshold of 50. Important variables used by the filters can observed in Table A.6.

	GPS only	Multi GNSS
$T_s(sec)$	1	1
$P_o(cycles)$	0.5	0.5
$Q_o(cycles)$	100e-06	1000e-06
L_R	N/A	10

Table A.6: Variables of Interest

Lastly, the low-grade equipment with low-cost antenna is studied. Again, the same performance metrics were used to assess the effects of varying the CAC threshold. The results can be seen in Tables A.7 and A.8 for the nominal and aided algorithms respectively.

CAC	1	10	25	50	100	150	200
TTFF (sec)	5.2	23.4	109.2	212.0	N/A	N/A	N/A
$P^i_{INT}(\%)$	0	0	0	0	N/A	N/A	N/A

Table A.7: Static Baseline Test: Low-Grade Antenna (Ublox/Patch)

CAC	1	10	25	50	100	150	200
TTFF (sec)	4.2	5.8	12.2	79.0	95.6	109.0	N/A
$P^i_{INT}(\%)$	30.0	39.4	39.6	86.9	90.2	100	N/A

Table A.8: Static Baseline Test: Low-Grade Antenna (Aided Ublox/Patch)

The nominal EKF is able to achieve a HP-RPV solution and these occurrences are acknowledged with their corresponding CAC value. The resulting HP-RPV however, is not within the 15 centimeter threshold and so the success rate is marked as zero. On the contrary, the aided algorithm observes a steady increase in integer fixing robustness with increasing CAC value. At a CAC value of 50, a nearly 87% success rate is observed. 100% success rate is observed at a CAC value of 150! Again, we see a cut-off for the HP-RPV availability at a CAC value of 200. Variables of interest for these tests are shown in Table A.9.

	Nominal	Aided
$T_s(sec)$	0.2	0.2
$P_o(cycles)$	10	10
Q (cycles)	1e-05	1e-05
$R_{UWB}(m)$	N/A	0.05

Table A.9: Variables of Interest

In conclusion, the CAC threshold has measurable impact on the robustness of the provided HP-RPV solution. It filters erroneous integer sets for high-grade equipment when GNSS availability is limited ensuring consistent HP-RPV solutions. Little to no impact is observed when varying the CAC threshold with multi-GNSS availability. This is because the algorithm can confidently fix integer sets as observed by the high ratio values. When using low-cost antennas, the CAC threshold can improve the probability that only the correct integer set is chosen. Most interestingly however, is the impact the CAC threshold has on the integer selection scheme when using a low-cost antenna and receiver. The CAC threshold is observed to remedy the indecisiveness of the aided algorithm by filtering erroneous integer sets that are temporarily calculated by the filter allowing for centimeter level precision for the low-cost sensor suite.